

Creation and Manipulation of Quantum States of
Light and Cold Atoms using Rydberg States

Thomas Henry Laycock, MPhys.

Thesis submitted to the University of Nottingham
for the degree of Doctor of Philosophy

December 2013

Abstract

Rydberg atoms are often proposed as the basis of quantum computing and quantum information protocols. One of the central reasons for this is that they provide a strong and long-ranged interaction that can be coherently switched on and off. This thesis details two techniques which use the exaggerated properties of Rydberg atoms to manipulate both the quantum state of the atom itself and that of the external light field.

The first proposal initially focuses on the creation of many-body quantum states from two-level atoms trapped in a two-dimensional lattice. This approach uses the van der Waals interaction present between alkali metal atoms in highly excited Rydberg s -states. The approximate solution of the corresponding Hamiltonian is detailed in the regime where the laser driving is the largest energy scale of the system. The states which are most likely achieved using an oscillating laser detuning are then determined. These states are then taken as the basis for the creation of deterministic single-photons, whose properties are shown to rely on the interplay between interatomic spacing and the geometry of the lattice.

The second technique described uses the coupling between a Rydberg atom and a moving electron to manipulate the atomic state.

In this system, the atom is initially excited to a Rydberg s -state and trapped at a finite distance from an electron waveguide. Two analytical methods are used to show that the final state of the atom depends strongly on the direction and modulus of the electron momentum. A complementary numerical simulation shows that the atoms may be left in a polarised state, suggesting the possibility of using this setup to ‘switch on’ *permanent* electric dipoles in the atoms. This investigation leads naturally to a system where multiple interacting atoms are trapped close to the waveguide, allowing various many-body states to be accessed.

Acknowledgements

First of all, I must thank those members of the research group with whom I have had the pleasure of working with for the past four years. First of all my supervisor, Dr. Igor Lesanovsky, who himself was only just settling into Nottingham when I applied for my postgraduate studies. His exemplary knowledge of cold atoms and Rydberg physics coupled with his drive to branch out into different less familiar areas meant that my studies have been both very challenging and very rewarding. Thank you very much, it has been a privilege to be part of your group. I reserve special thanks for Dr. Beatriz Olmos, who always made time to explain to me how to get around and/or solve many of the numerous problems I encountered or even sometimes created unnecessarily during the course of my studies. Also, I have to thank Dr. Weibin Li for his numerically generated Rydberg atom wavefunctions, which have been used extensively for much of my work, and for being present for many of my discussions with both Igor and Bea about which directions it was feasible to take my work. I think it is fair to say that I would not have got this far without the continual support of these three people. Further thanks go to Prof. Mark Fromhold who, along with responding to my first enquiries about applying to Nottingham, helped enhanced to my understanding of how condensed matter systems may be used in conjunction with my more familiar cold atom ones. It is quite unbelievable that the huge group in which I complete my studies has stemmed from the tiny one in which I started, which I feel is an indication of the

talent of the people I have been lucky enough to work with.

I can't really write this section without acknowledging the contribution of fellow PhD student Tom Montgomery, whose enthusiasm for discussions about all areas of physics proved often to be very fruitful to both of us, even if he did have a tendency to get very animated. Along with other fellow students Anton Piccardo-Selg, Sonali Warriar and Gal Aviv, I have had many enjoyable times both at conferences and just at general nights in Nottingham, which served as very useful breaks from my studying. Speaking of my down time, I have to further thank Igor for those few odd days where I left the office to compete in various pool competitions. This time allowed me to both satisfy my competitive side and form numerous friendships not connected to my work.

I move now to thanking those people who have had a huge influence on my life outside of studying. First of all there is my girlfriend, Ellie, who has been a saint with me when I worked late at the office or returned home late from a trip to the pub after the office. Not to mention too her faith in me at those unavoidable times when work doesn't seem to be going as smoothly as it probably should be. Finally, my thanks go to my family, without whose love and support I probably wouldn't have found myself in a position to start studying for a PhD, let alone be at the point where I am submitting my thesis.

Contents

Abstract	i
Acknowledgements	iii
List of Figures	viii
List of Tables	xii
1 Introduction	1
1.1 An Overview of Cold Atom Physics	1
1.2 Interactions between Light and Atomic Ensembles	5
1.3 Rydberg Atoms	9
1.3.1 Rydberg Atom Interactions	13
1.3.2 Summary of Proposals and Experiments	18
1.4 Structure of this Thesis	20
2 Photon Emission from a Rydberg Atom Lattice	22
2.1 Introduction and Background	22
2.2 System and Hamiltonian	25
2.3 Solution of the Hamiltonian	29
2.3.1 The Holstein-Primakoff Transformation	30
2.3.2 Constrained Dynamics	33
2.4 Excitation of the Many-Particle States	37

2.4.1	Addressing the Many-Body States	39
2.4.2	Excitation Properties	43
2.4.3	Selection Rules for Accessing the Many-Body States	54
2.4.4	Transition Intensities to Imperfect Lattices	57
2.5	Exact Diagonalisation of the Holstein Primakoff Hamiltonian	59
2.5.1	Exact Diagonalisation Algorithm	63
2.5.2	Removal of the Linear Terms	66
2.5.3	Validity of the Strong Driving Solutions	69
2.6	Single Photon Sources	71
2.6.1	Mapping to a Stable State	72
2.6.2	The Atom-Light Hamiltonian	73
2.6.3	The Atom-Photon Mapping	78
2.6.4	The Angular Density Matrix of the Single Photon State	85
2.7	The Emitted Photons	89
2.7.1	Square Lattice Emission	89
2.7.2	Triangular Lattice Emission	91
2.7.3	Hexagonal Lattice Emission	93
2.7.4	Uncertainty in Atomic Position	95
2.8	Summary and Outlook	96
3	Rydberg State Control using Electrons	99
3.1	Introduction and Background	99
3.2	System and Hamiltonian	101
3.3	Preliminary Investigation	104
3.3.1	The Born Oppenheimer Approximation	107
3.3.2	Beyond Perturbation Theory	111
3.4	Analytic Analysis	119
3.4.1	Time-Dependent Schrödinger Equation	119

3.4.2	Scattering Solution	125
3.4.3	Interpretation of the Transition Amplitude Result	133
3.5	Numerical Analysis	136
3.5.1	Rubidium	137
3.5.2	Lithium	142
3.5.3	Species Comparison	146
3.5.4	Comparison with Previous Work	150
3.5.5	Lifetime Considerations	151
3.6	Extension to a Chain of Atoms	152
3.6.1	Interatomic Interaction Dominated and Electron-Atom In- interaction Dominated Regimes	161
3.7	Summary and Outlook	162
Appendices		165
A Atomic Units		165
B Interaction of a Two-Level Atom with a Classical Field		166
C Transformation to a Rotating Frame		169
D Adiabatic Elimination of the Auxiliary State		172
E Atomic Transition Dipole Elements		174
F Lippmann-Schwinger Scattering Beyond the Born Approxima- tion		175
Bibliography		177

List of Figures

1.1	An illustration of an atomic level scheme and the resulting Rabi oscillations	6
1.2	A schematic representation of a quantum repeater.	8
1.3	A diagram of the basis for the atomic ensemble quantum repeater	9
1.4	Diagram showing the labels used in characterising the dipole-dipole interaction.	13
1.5	Simplified level scheme to characterise the Rydberg-Rydberg interaction.	14
1.6	A schematic showing the Rydberg blockade.	16
2.1	The square lattice and atomic level scheme and an illustration of the intended photon production from the lattice.	26
2.2	The energy manifolds and couplings given by the bosonic Hamiltonian.	34
2.3	Atomic level scheme required for experimental generation of the bosonic ground state	38
2.4	Transition intensities from the ground state to the singly excited states for an $L_{\text{sq}} = 10$ square lattice.	46
2.5	Transition intensities from the highest energy single excitation state to the double excitation manifold for an $L_{\text{sq}} = 10$ square lattice.	47

2.6	Diagram of the equilateral triangular lattice.	48
2.7	Transition intensities from the ground state to the singly excited states for an $L_{\text{tri}} = 10$ triangular lattice.	49
2.8	Transition intensities from the highest energy single excitation state to the double excitation manifold for an $L_{\text{tri}} = 10$ triangular lattice.	50
2.9	Diagram of the hexagonal lattice confined in the external geometry of a rhombus.	50
2.10	Transition intensities from the ground state to the singly excited states for an $L_{\text{hex}} = 11$ hexagonal lattice.	52
2.11	Transition intensities from the highest energy single excitation state to the double excitation manifold for an $L_{\text{hex}} = 11$ hexagonal lattice.	53
2.12	The three system geometries and their symmetries.	55
2.13	Average intensity profile for an $L_{\text{sq}} = 10$ square lattice when atomic position uncertainty is introduced.	57
2.14	A comparison of the single excited manifold spectra generated using the strong laser driving regime and the exact diagonalisation procedure	70
2.15	Atomic level scheme for the mapping from a collective excitation state to a photonic state.	73
2.16	Initial atomic state and photon emission patterns for a range of lattice spacings for an $L_{\text{sq}} = 7$ square lattice.	90
2.17	Initial atomic state and photon emission patterns for a range of lattice spacings for an $L_{\text{tri}} = 7$ triangular lattice.	92
2.18	Initial atomic state and photon emission patterns for a range of lattice spacings for an $L_{\text{hex}} = 11$ hexagonal lattice.	94

2.19	Change of the photon emission distribution of the square lattice when uncertainty in atomic position is introduced.	96
3.1	A schematic of the single Rydberg atom and single electron system.	102
3.2	Radial transition dipole elements and energy spectrum for rubidium.	108
3.3	The bound states of the interacting electron and Rydberg atom system in the Born Oppenheimer approximation.	111
3.4	The form of the momentum space coupling functions $\mathcal{F}(k - k')$ and $\mathcal{G}(k - k')$	115
3.5	Avoided crossings in the electron dispersion relation when it is coupled to the Rydberg atom.	117
3.6	Analytically calculated single atom transition amplitudes to various final states.	134
3.7	Comparison of the spectra of rubidium and lithium about the state $ 55s\rangle$	137
3.8	Numerically calculated transition amplitudes for different angular momentum states in rubidium.	138
3.9	How the expectation values $\sqrt{\langle L^2 \rangle}$ and $\langle m \rangle$ vary with momentum κ for three values of the coupling strength η in rubidium.	140
3.10	Characterisation of the polarisation of the final state of rubidium.	141
3.11	Numerically calculated transition amplitudes for different angular momentum states in lithium.	143
3.12	How the expectation values $\sqrt{\langle L^2 \rangle}$ and $\langle m \rangle$ vary with momentum κ for three values of the coupling strength η in lithium.	145
3.13	Characterisation of the polarisation of the final state of lithium. .	146
3.14	Initial state probabilities, numerical transition amplitudes and analytic p -state occupation for both rubidium and lithium.	147

3.15	Polarisations of the final states of rubidium and lithium when different initial conditions are taken.	149
3.16	An illustration of the system where multiple atoms are trapped along a length of the electron wire.	153
3.17	Single state and total transition amplitudes for the two trapped atom system.	160

List of Tables

1.1	Scaling laws for some properties of Rydberg atoms.	12
2.1	Table showing the average percentage errors of the single excitation manifold state energies of the strong laser driving regime.	71
A.1	Atomic and SI unit conversion table.	165

Chapter 1

Introduction

In this thesis there are two main research chapters, each investigating distinctly different problems. For this reason, this introduction covers only the topics which are common to both problems, with a second more focused introduction given at the start of each research chapter.

1.1 An Overview of Cold Atom Physics

Cold atom physics is one of the most diverse and active research fields today. It provides us with a unique opportunity to study a wide range of many-body systems in clean and decoherence-free environments [1–3]. Advances in our ability to trap and cool atoms [4,5] led to the first observation in 1995 of a Bose-Einstein Condensate (BEC) [6,7], a new state of matter first predicted 70 years earlier [8,9]. These seminal experiments paved the way for a wealth of theoretical and experimental studies of the phenomena associated with a macroscopic occupation of the quantum ground state. A few examples of the subsequently undertaken studies are the observation of interfering condensates [10,11], the optical confinement and formation of condensates [12,13], long-range phase coherence [14] and the formation of quantised vortices [15,16]. In addition to these there have been nu-

merous experiments that have achieved BEC with different atomic species. More recently, there has been significant interest in the miniaturisation of the condensing process with the use of atom chips [17–19], leading to a great advancement in the fields of atom optics [20] and atom interferometry [21].

A key element of cold atom physics that has thus far been omitted in this brief review is the optical lattice [22]. A simple description of this novel technique is the storage of cold atoms in artificial periodic potentials formed by the superposition of counter-propagating laser beams. Trapping of the atoms relies on the interaction between an induced atomic dipole moment and the external electric field of the incident laser light, thus forming an optical dipole trap [23]. Using counter-propagating laser beams creates a standing wave in the associated electric field, the detuning of the laser thus determining where the atoms are trapped. For optical lattices created by red detuned lasers, it may be shown that the atoms are attracted to the maxima in the electric field, whereas in the case of blue detuned lattices the atoms are expelled from these maxima. Therefore, creating a trap using blue detuned lattices is more complicated, requiring extra potentials to be introduced to stop the atoms being completely expelled from the laser field. However, it has been shown that it is possible to trap atoms using blue detuned light [24, 25]. Optical lattices are therefore an incredibly versatile tool in the study of many cold atom systems in the fact that both the geometry and strength of the confining potential are easily varied. In order to vary the geometry of the system, the associated laser beams need merely be interfered under a different angle. The depth of the confining potential is even simpler to vary, as it is simply altered by changing the intensity of the incident laser beams. This powerful technique is central to both the topics detailed in this thesis, therefore remainder of this section outlines many, but by no means all, of the fields in which optical lattices have been instrumental.

It was Richard Feynman who initially championed the idea that the simulation of one complex quantum system required a different highly controllable quantum system [26–28]. The problem being posed by the simulation of a quantum system is the scaling of its Hilbert space. The size of this complex vector space, in which the wavefunctions of the quantum system exist, increases exponentially with the size of the system. A measure of the system size is the number of variables required to completely describe it. This scaling of the Hilbert space renders even the problem of recording the quantum state of the system intractable using a classical computer, as it requires an exponential amount of memory. The insight Feynman gave was to question whether this exponential growth of resources could be bypassed by having the simulator itself a quantum system, thus obeying the same equations of motion as the simulated system. This is the fundamental description of a quantum simulator. A variety of possible systems which may be used as these simulators are outlined in [29].

The quantum simulator finds some of its most striking realisations to date in the simulation of condensed matter systems using optical lattices [30,31]. The famous Hubbard model [32], where interacting particles on a lattice are described by only two parameters - their on-site interaction energy and a site-hopping potential - has long been used as an approximate model for the extremely complicated problem of interacting electrons in condensed matter systems. This is the perfect model to describe interacting particles in a zero temperature optical lattice. Indeed one of the key predictions of the Hubbard model; the superfluid (tunnelling dominant) to Mott insulator (on-site interaction dominant) phase transition, was observed in an optical lattice in 2002 [33]. Further to these initial studies, where the lattice was loaded with bosonic atoms, has been the realisation of the Mott insulating state of fermionic atoms [34]. This is an important step, as it brings the field closer to the case of electrons in a solid, where proximity to the Mott

insulating phase has been proposed as a possible origin of high temperature superconductivity [35].

Further to the idea of using one quantum system to simulate another, the idea that the laws of quantum mechanics could also be used to enhance or supersede the capabilities of classical computers has also been developed [36]. The fact that quantum mechanical states may exist in superpositions allows the classical ‘bit’ of information to be replaced in a quantum computer by a *quantum* bit, or qubit. These qubits may be viewed as two-level systems whose possible states, $|0\rangle$ and $|1\rangle$, may also form superpositions following the laws of quantum mechanics. The basis for the quantum computer itself is a quantum register [37] formed by an entangled string of qubits. A quantum computation is performed when a unitary operation is made on the state of the register, which may be decomposed into a sequence of single- and two-qubit operations, the former performing a rotation of a specific qubit in the register, and the latter entangling the two involved qubits. The role of quantum entanglement in quantum computation is considered in [38], where one its main applications is to provide exponential speed up of algorithms over classical computation [39]. This ability has been famously demonstrated with the predicted efficiency gain in the factorisation of large numbers using an algorithm only possible on a quantum computer [40]. There have been many proposals using cold atoms in optical lattices as the foundation for such a quantum computer [41–44]. One such example is based on the formation of a Mott insulator state with precisely one atom per lattice site where only one specific internal state of the atom is trapped [45]. Overlapping two lattices that trap different internal atomic states, which must be carefully chosen, may form the basis of a quantum register, where moving one lattice relative to the other can implement computation operations. Complementing this method is the more recent development of single-site addressability of the lattice [46], which allows the internal

state of the atom at a specific site to be changed.

This brief review has only scratched the surface of the astounding variety of proposals and experiments being carried out in the world of cold atoms. This thesis details two further areas of research, both of which rely on the ability to trap and store atoms in regular arrays or by themselves. The following section introduces the reader to the current state of research into quantum interfaces between light and atomic ensembles, which is particularly important for the systems described in chapter 2.

1.2 Interactions between Light and Atomic Ensembles

As discussed briefly in the previous section, the interaction between an atom and an electromagnetic field is governed primarily by the electric field inducing an atomic dipole moment which subsequently interacts with the inducing field. In optical lattices, the frequency of the field is far detuned from any of the atomic transition frequencies, so as to trap the atom rather than induce state transitions in it. The focus here will be on near-resonant fields, such that a single atom undergoes Rabi oscillations when subject to them. As neatly derived and explained in [47], the presence of a strong and near-resonant laser field means that only two atomic states are relevant to the dynamics, the ground and close to resonance excited state, with the dominant population oscillating between the two. An example of a level scheme and applied laser in this regime can be seen in Fig. 1.1, where it is clear that as the frequency of the laser becomes further detuned from that of the atomic transition, the population transfer is reduced whereas the frequency of the oscillation is increased.

Of course, the situation becomes more complicated when the single atom is

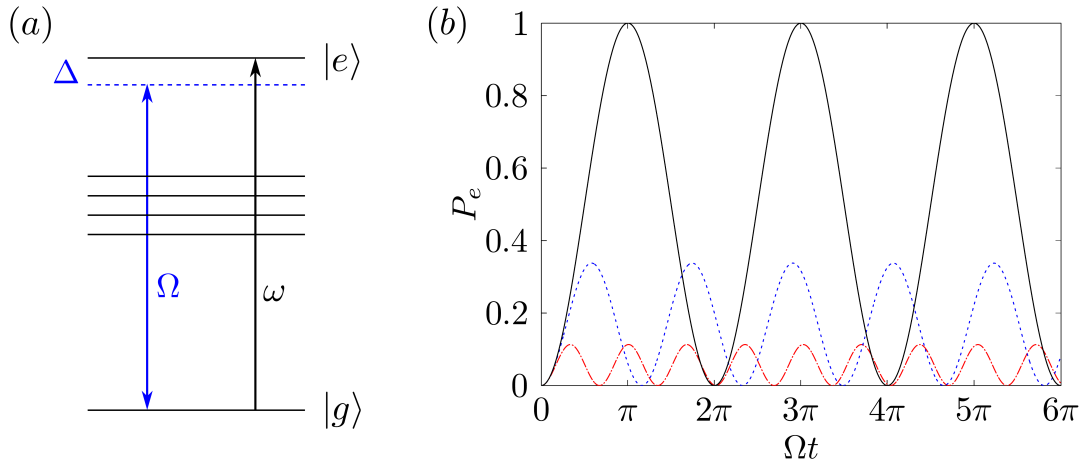


Figure 1.1: (a) Simplified representation of the level scheme of an atom where a laser of Rabi frequency $\Omega = -\langle e | \mathbf{d} \cdot \mathbf{E}_0 | g \rangle$ is close to resonance with the atomic transition $|g\rangle \rightarrow |e\rangle$. (b) The resulting Rabi oscillations when the laser has three different values of detuning; $\Delta = 0$ (black, solid), $\Delta = 2.8\Omega$ (blue, dashed) and $\Delta = 5.6\Omega$ (red, dot-dash), where P_e is the probability of finding the atom in the excited state.

replaced by an interacting atomic ensemble. In this case collective excitation states of the atomic ensemble may be coupled to the light field [48]. One of the initial proposals to couple light and atomic ensembles was to map a squeezed light state onto the spin state of the atomic ensemble [49]. The experimental verification of this proposal [50], demonstrated that the storage of a quantum state of light in an atomic ensemble was indeed possible and motivated the development of numerous further approaches. An example of these is based on using electromagnetically induced transparency [51] to reduce the speed of light in the atomic ensemble [52] to zero, thereby creating an atomic memory for light [53]. The following paragraphs outline just a few fledgling technologies in which these quantum memories, where the quantum state of light is stored in an atomic state, could play a central role.

Once again, the main implementations of this technology, but by no means the only ones, are found in the field of quantum computation and communication. Specifically, atoms and photons fulfil the three main requirements for a distributed

quantum computer network, which are outlined succinctly in [48] as: mapping the light state onto a memory, storage and computing operations on the memory and efficient retrieval of the memory state back into light for transport and further operations. In the quantum computing sense, such a network may be seen as a step towards a quantum computer with a very high number of qubits. Such a large qubit number quantum computer, which is currently technologically out of reach, may be simulated using a number of low qubit number computers between which the quantum information is transferred in various channels [54]. The initial outline of a quantum computer network may be found in [55], where examples of proposals for state transfer between the computational nodes are given in [56,57]. The following ideas are based on using photons to transfer the quantum state between nodes which are comprised of atomic ensembles.

One of the challenges of this model of a quantum computer is the efficient transport of a quantum state between different memories in the network, which is hampered by the information photon being absorbed by or depolarised within an optical fibre. A proposal to overcome this issue is the idea of a quantum repeater [58]¹, the building blocks of which are sources of entangled photons and quantum measurement devices. It has been subsequently shown that a variation on this scheme can be used to result in the entanglement of atomic ensembles that are spatially separated [59]. A diagram representing how the necessary entanglement between the ensembles is generated is provided in Fig. 1.3. This more complicated scheme is capable of creating entanglement in collective excitation

¹In general, a single quantum repeater has two sources each producing two entangled photons. The entangled state created from each source should be the same. After some distance d , which is within the length over which entanglement is reliably conserved, one photon from each source is measured. If the result of the measurement is the same for each photon then the two remaining photons are entangled. An advantage here is that when the remaining photons are counter-propagating, their entanglement now exists over a distance $2d$. This scheme is represented diagrammatically in Fig. 1.2. Adding another repeater and measuring one of the resulting photons from each increases the entanglement distance to $4d$ and so on. This is a simplified picture of a quantum repeater, but is intended to convey the main idea that such a device may increase the distance over which quantum state transfer is reliable.

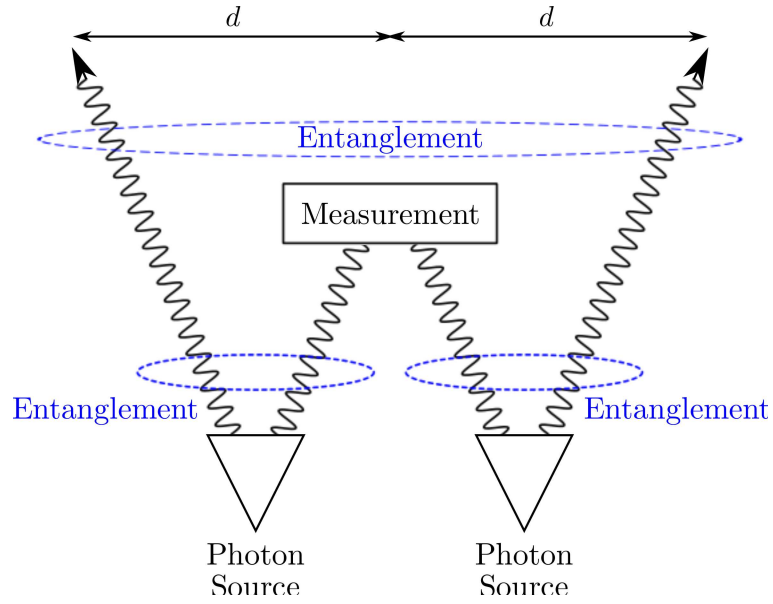


Figure 1.2: A schematic representation of a quantum repeater. The measurement of one photon each from the two sources of entangled photons leaves the remaining two photons, one from each source, entangled. This setup may be used to increase the distance over which entanglement may be conserved.

states of atomic ensembles over distances greater than those possible with a single photon and therefore may be used to copy the exact state of a system over distance. The first steps towards the experimental achievement of this protocol are documented in [60]. This initial paper shows how the write pulse generates a photon which may subsequently be used for ensemble entanglement, with a later read pulse transferring the ensemble state into a photon. Further studies focus on the interpretation of the photon produced by the readout laser as retrieving information from a quantum memory [61–64].

This section has introduced how the interactions between light and atomic ensembles may be used in a number of applications in the field of quantum information. A further use of this type of interaction is the generation of non-classical states of light using ensembles of Rydberg atoms. This proposal, which is particularly relevant to the research presented in chapter 2, is presented in section 1.3.2, after the following section introduces Rydberg atoms and their properties.

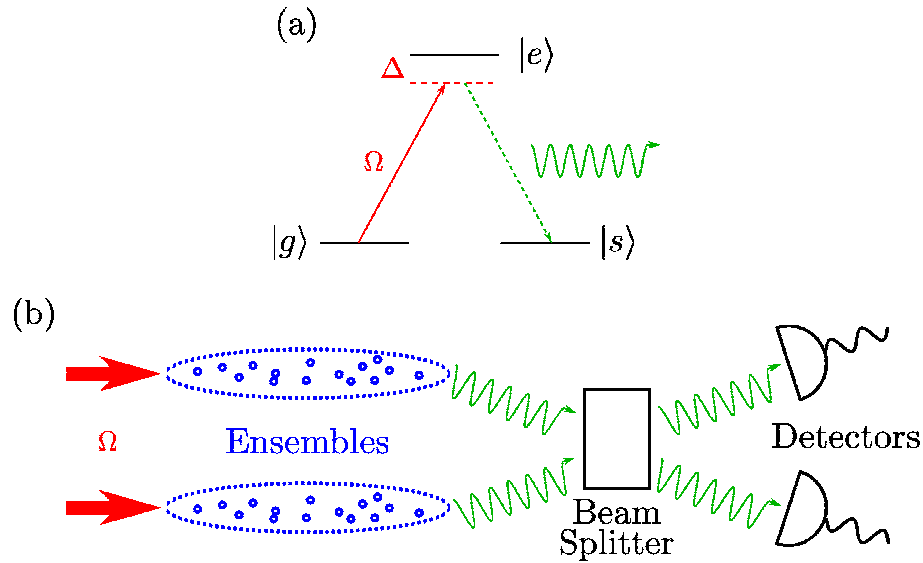


Figure 1.3: (a) The atomic level scheme required for the ensemble quantum repeater. A classical laser with Rabi frequency Ω couples the levels $|g\rangle$ and $|e\rangle$ off resonantly with a photon subsequently emitted on the transition $|e\rangle \rightarrow |s\rangle$. (b) Two ensembles are illuminated with the a pulse of the laser of Rabi frequency Ω such that the transition $|g\rangle \rightarrow |s\rangle$ is achieved via auxiliary level $|e\rangle$. With the initial pulse light filtered out (not shown), the remaining light is interfered at a 50 – 50 beam splitter such that the ensembles are entangled when a photon emitted with the $|e\rangle \rightarrow |s\rangle$ frequency and polarisation is detected at either detector. The resulting entangled pairs of atomic ensembles then act as the basis for an ensemble quantum repeater. This image is an adapted version of that found in [59].

1.3 Rydberg Atoms

The term ‘Rydberg atom’ refers to an atom whose valence electron is excited to a very high principal quantum number, $n \gg 1$. In this section, some of the exaggerated properties of these atoms will be introduced, which is followed by a review of proposals and experiments where they play a central role. It will be shown that many properties of Rydberg atoms scale with their principal quantum number. The idea of the principal quantum number itself was initially encountered in Bohr’s model of the atom, where the requirement of the quantisation of the angular momentum of the valence electron in units of \hbar was first introduced.

Following the later development of quantum mechanics, it has also been shown that this quantisation follows naturally from solution of the Schrödinger equation.

The scaling of the orbital radius of a Rydberg atom will be introduced first. A simple calculation of this property utilises the classical model of the motion of the single bound electron in a hydrogen atom,

$$\frac{m_e v^2}{r} = \frac{e^2}{4\pi\epsilon_0 r^2},$$

where m_e is the mass of the electron, e is its charge, r is the radius of its circular motion and $1/(4\pi\epsilon_0)$ is the Coulomb constant. From Newton's second law, this equates the Coulomb interaction between the nucleus and electron with the electron mass times the centripetal acceleration when the electron is in a circular orbit with tangential velocity v . The requirement that the angular momentum of the electron be quantised in units of \hbar may be written as,

$$m_e v r = n\hbar,$$

which may be rearranged into an expression for v . Substituting the tangential velocity into Newton's equation yields the expression for the radius of the orbit

$$r = \frac{(4\pi\epsilon_0)\hbar^2}{e^2 m_e} n^2,$$

which clearly scales as the square of the principal quantum number, with the prefactor recognised as the Bohr radius, a_0 . Therefore, when the outer electron of any atom is in a highly excited state, it may be found at great distances from the core of the atom, which consists of the nucleus and the other orbiting electrons. This qualitative result is confirmed by solving the quantum mechanical problem of the electron moving in the attractive central potential of the hydrogen

nucleus, where the actual result changes to [65]

$$\langle r \rangle = \frac{a_0}{2} [3n^2 - l(l+1)],$$

and has introduced l , the orbital angular momentum quantum number of the electron. This result becomes important in chapter 3, where the minimum possible distance between two separate quantum systems needs to be fixed.

Further scaling laws for Rydberg atoms can be gleaned from the Bohr model. One that will be important in this thesis is the energy difference between adjacent n states. The energy, W of an atomic state is obtained by summing the kinetic and potential energies of the electron [66]

$$W = \frac{m_e v^2}{2} - \frac{e^2}{(4\pi\epsilon_0)r} = -\frac{e^2 m_e}{2(4\pi\epsilon_0)^2 n^2 \hbar^2} = -\frac{1}{2} \frac{1}{a_0(4\pi\epsilon_0)} \frac{1}{n^2},$$

where the fact that these energies are negative indicates that they are bound states. From this, it is possible to find the scaling of the energies between adjacent principal quantum number states of a Rydberg atom,

$$W_{n+1} - W_n = \frac{1}{2a_0(4\pi\epsilon_0)} \left(\frac{1}{n^2} - \frac{1}{(n+1)^2} \right) = \frac{1}{2a_0(4\pi\epsilon_0)} \frac{2n+1}{n^4 + 2n^3 + n^2} \\ \underset{n \gg 1}{\approx} \frac{1}{2a_0(4\pi\epsilon_0)} n^{-3}.$$

Therefore the higher lying Rydberg states lie closer together in energy with increasing n .

One further scaling law for the Rydberg atoms is that of the transition dipole moments, which will repeatedly be referred to in the research chapters of this thesis. Depending on whether a change in principal quantum number is involved in the dipole transition (there are no selection rules to govern a change of n), analytical expressions for these can be very difficult to calculate, for example see

the expression for the radial part only given in [67]. However, there is a simple analytical expression for the radial transition dipole moment when the principal quantum number is conserved, the derivation of this result will not be given here, but is laid out nicely in [68] and is quoted in [66] as being

$$\langle \mathcal{R}_{nl} | r | \mathcal{R}_{nl+1} \rangle = \frac{-3n\sqrt{n^2 - l^2}}{2} a_0,$$

where \mathcal{R}_{nl} is the radial wavefunction of the hydrogen atom with quantum numbers n and l . The scaling of the dipole transition elements for atoms in Rydberg states with low angular momentum is therefore proportional to n^2 . Due to the extremely large size of Rydberg atoms, the resulting scaling of the transition dipole moments means that they are very sensitive to electric fields, a fact which will specifically utilised in chapter 3, with relevant experiments provided in section 1.3.2 of this introduction.

This section has briefly outlined the main scaling laws for atoms in Rydberg states. Provided in table 1.1 are all of the scalings that are used in this thesis, where a further point to note is the scaling of the radiative lifetime, which shows

Property	Scaling
Binding Energy	n^{-2}
Energy between adjacent n states	n^{-3}
Orbital Radius	n^2
Transition Dipole Moment	n^2
Radiative Lifetime	n^3

Table 1.1: Scaling laws for some properties of Rydberg atoms. Those not already examined are given in [66].

that these highly excited states are actually longer lived as the level of excitation increases.

The following section of this introduction details the interaction between two Rydberg atoms, which will be important in both research chapters of this thesis.

1.3.1 Rydberg Atom Interactions

The interaction between two Rydberg atoms whose nuclei are separated by a distance $R_{ab} \equiv |\vec{R}_{ab}|$ which is much greater than the orbital radius of the specific Rydberg state, $\langle r \rangle \approx 3/2 \times n^2$, is given by the dipole-dipole interaction. The labels that are used to describe this interaction are shown in the schematic in Fig. 1.4. Viewing the nuclei as single positive charges fixed in position, the full

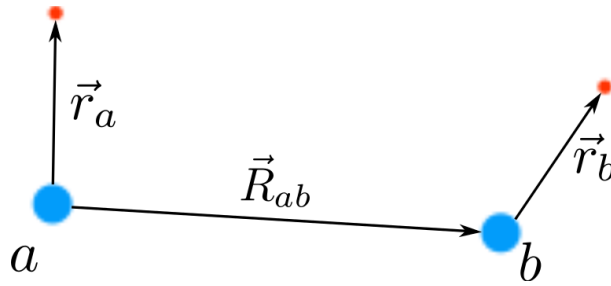


Figure 1.4: Diagram showing the labels used in characterising the dipole-dipole interaction.

Coulomb interaction potential may be written as

$$V_{\text{dd}} = \frac{1}{R_{ab}} - \frac{1}{|\vec{R}_{ab} + \vec{r}_b|} - \frac{1}{|\vec{R}_{ab} - \vec{r}_a|} + \frac{1}{|\vec{R}_{ab} + \vec{r}_b - \vec{r}_a|},$$

where \vec{r}_a and \vec{r}_b are the vectors describing the positions of the valence electrons of atoms a and b respectively, with \vec{R}_{ab} the displacement of the two nuclei. The four terms all describe Coulomb interactions in atomic units; the first is that between the two nuclei, the second and third are between each nucleus and the valence electron of the other atom with the final term being that between the two valence electrons. Under the assumption $R_{ab} \gg r_a, r_b$, where $r_a \equiv |\vec{r}_a|$ and $r_b \equiv |\vec{r}_b|$, this expression may be Taylor expanded about $r_a, r_b = 0$ to yield

$$V_{\text{dd}} \approx \frac{\vec{r}_a \cdot \vec{r}_b}{R_{ab}^3} - 3 \frac{(\vec{r}_a \cdot \vec{R}_{ab})(\vec{r}_b \cdot \vec{R}_{ab})}{R_{ab}^5}.$$

To see the effect of this interaction, consider the example where two atoms are initially laser excited to the same Rydberg state. As explained in [69], the dipole-dipole interaction will cause dipole transitions to other states, of which there are an infinite number. However, due to differing energy gaps and dipole transition elements between these states, the interactions are dominated by the coupling between only two of them [70]. The following characterisation of the strength of this atomic interaction is based on the simple model described in [71].

For simplicity, the two atoms are initially excited to the state $|ns\rangle$, a situation which will be expressed as $|ss\rangle$. A further simplification of the problem sees the separation between the atoms be only in the z -direction, such that $\vec{R}_{ab} = R_{ab}\hat{z}$. The dipole transition rules mean that the initial state only couples to those where both atoms are in a p -state, but further approximations to the strength of these transitions may be made. Using the spectrum of a rubidium atom, which may be seen in Fig. 3.2(b), the p -states which are closest in energy to $|ns\rangle$ are $|np\rangle$ and $|(n-1)p\rangle$, therefore only the coupling to these states is considered, as illustrated in Fig. 1.5, with E_{np} and $E_{(n-1)p}$ their respective energies, and the energy of the

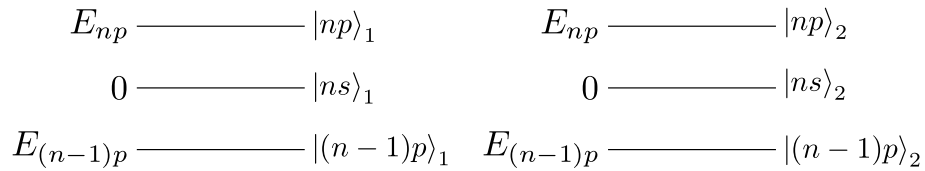


Figure 1.5: Simplified level scheme of the two atoms which will be used to characterise the Rydberg-Rydberg interaction.

initial state is set to zero. Using these as the only relevant states of the atom, there are only three possible states to which the initial state is coupled,

$$\begin{aligned}
 |npp\rangle &= |np\rangle_1 |np\rangle_2, \\
 |(n-1)pp\rangle &= |(n-1)p\rangle_1 |(n-1)p\rangle_2 \quad \text{and} \\
 |nnpp\rangle &= \frac{1}{\sqrt{2}} (|np\rangle_1 |(n-1)p\rangle_2 + |(n-1)p\rangle_1 |np\rangle_2).
 \end{aligned}$$

Furthermore, when considering that $|E_{np}| \approx |E_{(n-1)p}|$, with $|E_{np}| > 0$ and $|E_{(n-1)p}| < 0$, the couplings to both $|npp\rangle$ and $|(n-1)pp\rangle$ can be neglected as these energy differences are much greater than that to $|nnpp\rangle$, $E_{np} + E_{(n-1)p}$. Including only these two states, the two atom Hamiltonian may be written as

$$H \approx \begin{pmatrix} E_{np} + E_{(n-1)p} & \frac{\gamma}{R_{ab}^3} \\ \frac{\gamma}{R_{ab}^3} & 0 \end{pmatrix} \equiv \begin{pmatrix} \delta & V_{12} \\ V_{12} & 0 \end{pmatrix},$$

where $\gamma = \langle ss | \vec{r}_a \cdot \vec{r}_b - 3(\vec{r}_a \cdot \hat{z})(\vec{r}_b \cdot \hat{z}) | nnpp \rangle$. The energies of the system are found by diagonalisation of the Hamiltonian,

$$E_{\pm} = \frac{\delta}{2} \left[1 \pm \sqrt{1 + \left(\frac{2V_{12}}{\delta} \right)^2} \right] \approx \frac{\delta}{2} \pm \left(\frac{\delta}{2} + \frac{V^2}{\delta} \right),$$

where the approximation considers the interaction energy smaller than the state separation, $V \ll \delta$. The solution E_- corresponds to the situation where the atoms are initially in the state $|ns\rangle$ and therefore the atoms have been shown to interact according to the van der Waals potential

$$V_{\text{vdW}}(R_{12}) = -\frac{V^2}{\delta} = \frac{C_6}{R_{12}^6},$$

where $C_6 = \gamma^2 / (E_{np} + E_{(n-1)p})$ is the van der Waals coefficient and typically scales as n^{11} [72, 73]. A simple way to estimate the scaling of this coefficient is to recognise that the numerator is essentially the square of the product of two transition dipole elements and the denominator roughly the energy level spacing, the individual scalings of which are seen in table 1.1. Due to this scaling of the interaction with the principal quantum number of the state, Rydberg atoms typically interact with a strength in the region of MegaHertz over micrometre distances [73]. Having briefly outlined the derivation of the Rydberg interactions

presented in [70], this section now provides a short explanation of the Rydberg (dipole) blockade, which is central to many of the proposals and experiments introduced in section 1.3.2.

The strength of the Rydberg-Rydberg interaction leads to a phenomenon called the Rydberg blockade, the observation of which is documented in [74] and is beautifully explained in [75]. To understand this effect, consider two atoms initially in the ground state, $|g\rangle$ and separated by a distance \mathbf{r} . Considering this ground state is coupled resonantly to the Rydberg state, $|r\rangle$, by a laser with Rabi frequency Ω_0 , the state where both atoms are in the Rydberg state has energy twice the atomic transition plus the energy of the interaction $V(\mathbf{r}) = C_6/|\mathbf{r}|^6$. A schematic representation of this situation can be seen in Fig. 1.6. Thus for both

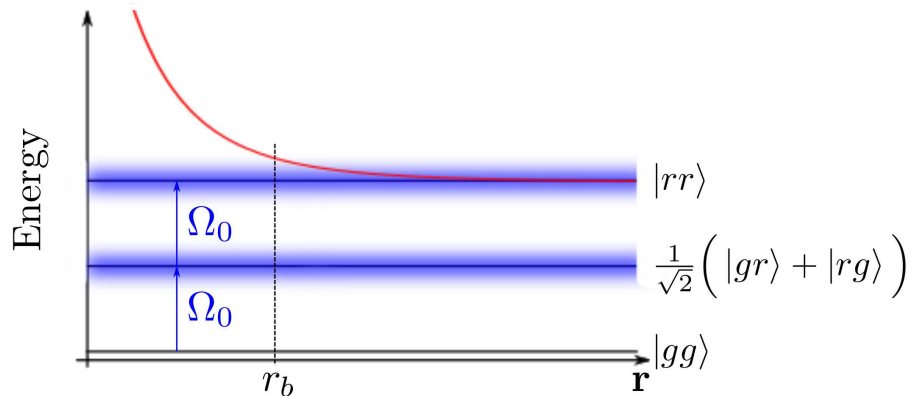


Figure 1.6: A schematic showing how the energy level of the simultaneous excitation situation changes with atomic separation (red curve) and how this is used to define the blockade radius, r_b . The blurred blue line represents the linewidth of the laser.

atoms to be excited simultaneously the interaction energy must be overcome by the laser. The probability of simultaneous excitation thus rests on the linewidth of the laser, which for strong laser driving is determined by the Rabi frequency. Therefore, the atoms may not be simultaneously excited if the interaction energy is larger than the Rabi frequency. This condition puts a limit on the separation

below which the atoms may not be simultaneously in the Rydberg state as

$$r_b \approx \left(\frac{C_6}{\Omega_0} \right)^{\frac{1}{6}},$$

which is known as the blockade radius.

The large distances over which Rydberg atoms interact and their sensitivity to electric fields [76–78] arising from the nucleus-valence electron separation may be used to interface different types of quantum system. In this context, the Rydberg atom forms one element of what is termed a *hybrid* quantum system. This is a particularly active research field with one of its main applications being the field of quantum computing, where with careful design these hybrid devices may combine the features of two very different quantum systems. In particular, advances in quantum computing place ever tighter requirements on the level of control of the quantum state. Various studies of interfacing a myriad of different quantum systems with various solid state devices may be found in [79–83]. One recent proposal couples Rydberg atoms to superconducting qubits via a nanomechanical resonator [84], which is shown to be a system suitable for both information storage and processing. A further composite system coupling a Rydberg atom to a superconducting transmission line is described in section 1.3.2, where a general overview of Rydberg experiments is provided. The idea of these hybrid quantum systems is employed in chapter 3 of this thesis, where a Rydberg atom is coupled to a moving electron to achieve quantum state control.

Having introduced the origin of the strong Rydberg-Rydberg interaction and one of its main consequences, this section concludes with a review of the very varied proposals where Rydberg atoms are a key feature, along with experiments which have been carried out.

1.3.2 Summary of Proposals and Experiments

Delving into the diverse world of Rydberg atom proposals and experiments, one finds many applications are in the field of quantum information, a comprehensive overview of which may be found in [69]. Many of these proposals are based on the idea of using the Rydberg blockade to create quantum gates [85] between two atoms, each of which may act as a qubit for quantum computing. Shortly after this initial proposal was made, it was also shown that the Rydberg blockade could be used to create quantum gates where the qubits are ensembles of atoms [86]. This second proposal uses the Rydberg blockade to ensure that only a single atom within the blockade radius is in the Rydberg state. The qubits are then the state where all atoms are in the ground state and the state which is a superposition of all possible combinations where only a single atom in the blockade radius is excited. The building blocks for this second regime were subsequently shown to be achievable when the Rydberg blockade was used to produce a collective excitation between two atoms in 2009 [87]. Further to the idea of using the Rydberg blockade as a tool to create quantum gates, the storage and manipulation of a large number of Rydberg atoms in a large-spacing optical lattice has recently been suggested as the basis for a quantum simulator [88], which would also make use of the single site addressability previously discussed [46].

The field focused on the interaction of ensembles of Rydberg atoms with quantum states of light is particularly active. One proposal taking such an approach is based on the use of a ring lattice occupied by Rydberg atoms to generate collective excitation states [89,90]. Following a mapping scheme detailed in [91,92], such collective excitations are shown to produce exotic states of light [93], where the photon is emitted into a superposition of different directions. It is shown that the emission distribution is governed by the coupling of the collective excitation to the readout laser field, and specifically the degree to which the collective spin

wave acts as a single degree of freedom on the scale of the laser wavelength. This work has clear applications in the field of quantum memories, showing not only that a particular excitation may be stored within an ensemble of atoms but also that the excitation may be retrieved deterministically, with the features of the excitation actually mapped into the retrieved photonic state. This work is extended in chapter 2 of this thesis, where Rydberg atoms are trapped in various two-dimensional geometries, with a detailed description of how the atomic states may be created and subsequently mapped into photonic states is provided. Furthermore, there have been two very encouraging experiments using this type of idea. One of these [94] creates a collective excitation in an atomic ensemble and subsequently retrieves only a single photon when the initial excitation is stored using very high principal quantum number states. The other [95] uses electromagnetically induced transparency to slow a single photon through an atomic ensemble, whilst ensuring that the shift of energy levels of the atoms due to the Rydberg-Rydberg interaction does not allow the similar storage of multiple photons.

Many proposals place Rydberg atoms in optical lattices as the ideal tool for the study of quantum many-body systems [96–98]. Whilst having great value in aiding our understanding of fundamental physics, advances in experimental techniques in this area of research will undoubtedly aid in the development of the many other proposals relying on the creation of collective excitation states. Indeed, as is shown in chapter 2 of this thesis, schemes are available that allow many body states to be created in such systems. Many proposals use lasers in order to create the specific collective excitations in the system, as will be seen to be the case in chapter 2. However, there have also been detailed studies into the changing of Rydberg states using collisions with either charged or neutral particles, for a very detailed review of this topic see [99]. As is shown in [100],

collisions of low energy electrons with Rydberg atoms can lead to changes in the orbital angular momentum state of the atom, and so this technique could be seen as complementary to the laser fields initially used to bring the atom to the Rydberg state. The research detailed in chapter 3, uses a similar method to control the state of a Rydberg atom using its interaction with a travelling electron, although in this scheme there is a fixed minimum distance between the two objects as the electron is guided. Whilst focusing mainly on how the passing electron changes the state of a single Rydberg atom, the chapter concludes with the description of when the electron passes a chain of interacting atoms. It is shown here that entanglement may be created between the atoms when a single electron passes the interacting ensemble. This is a very simple way to produce very interesting quantum many-body states. The fact that the electron passes the atoms within a waveguide is unique within the field of collisions of electrons with Rydberg atoms and as shown in chapter 3 may even allow the creation of *permanent* electric dipoles of the atom.

1.4 Structure of this Thesis

In conclusion of this introductory chapter, this brief section provides an overview of the research presented in the following chapters. A more detailed summary of each chapter may be found in its own introductory section. Chapter 2 describes how non-classical states of light may be produced from collective excitation states formed using Rydberg atoms in two dimensional lattices. First of all, as the laser driving of the lattice system is rather complex, the Hamiltonian is introduced and an approximate solution method outlined. This is then followed by a scheme for the preparation of the collective excitation states, detailing both the excitation spectra for perfectly prepared lattices and those where uncertainty in the atomic positions is present. Following the derivation of an exact diagonalisation method

for the Hamiltonian of this system, the focus moves to the generation of photons from these excitations. The full derivation of the photonic angular distribution is given, which is followed by distributions from the three lattice geometries considered, including once again those with finite uncertainty in the position of the atoms. This chapter concludes with a section dedicated to summarising the main results and suggesting some possible extensions.

In chapter 3, the research is distinctly different from that concerning Rydberg atoms on a lattice. As alluded to previously, the research here focuses on the interaction between a trapped Rydberg atom and a moving electron and how, by tuning the momentum of the electron, it may be used to alter the initial atomic state. Once again, this chapter starts with a detailed introduction of the Hamiltonian of the system and how the interaction part may be simplified under certain conditions. An initial study of how the interaction affects the states of the system is carried out using perturbation theory. Two more powerful techniques are subsequently employed, approximate solution of the time-dependent Schrödinger equation and Lippmann-Schwinger scattering theory, both of which are capable of describing the changing state of the atom and yield identical results. Upon introducing the real level structure of the atom, a numerical approach is employed based on the Schrödinger equation method, the results of which for both rubidium and lithium are detailed and compared. The analytical approach is then extended to the case of multiple trapped interacting Rydberg atoms interacting with the electron, and some preliminary results are given. Concluding this chapter is a brief summary of the research presented along with a small number of possible extensions and alternatives.

Chapter 2

Photon Emission from a Rydberg Atom Lattice

2.1 Introduction and Background

The drive to understand the quantum interface between light and atomic ensembles has been underway for well over a decade [48]. One of the initial studies of this interface [49] showed that it was possible to map the squeezing of a light beam onto the spin states of an atomic ensemble, and helped to show that proposals relying on the coherent coupling between the two systems were feasible. Examples of these proposals which will be relevant here are those of implementation of quantum information processing protocols [86, 101–104], quantum memories [61–64] and the often closely related creation of deterministic and manipulable photon sources [62, 105–108]. Such photon sources rely on the ability to create entangled atomic many-body states and map them efficiently onto the desired photon states [91, 93, 109, 110]. The current myriad of techniques available for the trapping and manipulation of ultracold atoms [1] places them as one of the front running candidates for the creation of these required atomic many-body states.

Enhancing the already impressive range of systems available by the use of these techniques is our ability to excite the trapped atoms to Rydberg states [66], which have strong state-dependent interactions and thus allow atomic interactions over distances of several micrometres [69, 88, 111].

An example of work emerging from the use of the strong interactions between cold trapped Rydberg atoms is the observation of electromagnetically induced transparency in such a system [112], which is the phenomenon best described in [51] as occurring when ‘an opaque atomic transition is rendered transparent to radiation at its resonance frequency’. A comprehensive review of the theory and experiments on this topic may be found in [113], though specific knowledge in this area is not required for the reader to follow the work presented in this thesis. This study has not only led to the advancement of the theoretical methods employed to describe such a system [114], but also to proposals for their application in the ever-growing field of quantum information [115]. However, as brilliant as this work may be, it is not directly related to what will be considered here. Recent work combining the features of cold atoms and Rydberg states which will be relevant here is the proposal of a ring lattice occupied by Rydberg atoms for the generation of collective excitations [89, 90]. The subsequent mapping of these collective excitations resulted in the creation of non-classical states of light [93] when a single photon is emitted from the lattice. The properties of this photon were shown to be dependent upon the interplay between the ring geometry and nature of the specific atomic excitation initially realised.

This chapter details the extension of the work detailed in [89, 90, 93] to three medium-scale complex two-dimensional lattice geometries: square, triangular and hexagonal. Such geometries, which increase in complexity, may be realised with the aid of microtrap array technology [116], which not only allows the creation of complex lattices, but may also be reconfigured with relative ease. While there

are many similarities between this work and the one-dimensional system, it will become apparent that the Jordan-Wigner transformation used to solve the Hamiltonian of the one-dimensional system is not applicable in two-dimensions, and an alternative is introduced. The solution of the Hamiltonian allows in a specific laser regime defines collective atomic states in the system, the excitation properties of which are thoroughly investigated. Following from this, the aim is to map these atomic states onto states of light, the procedure for which is described prior to a detailing of the states which may be obtained. Numerical investigations on the effect of atomic position uncertainty on both the atomic and photonic states are also detailed, such that the results are related to effects that will undoubtedly be encountered in an experimental situation.

The chapter is structured as follows. Section 2.2 introduces the system and its Hamiltonian and shows that a two-level description is valid. Section 2.3 details the solution of the Hamiltonian when it is limited to the regime where the laser driving is dominant and describes the approximate spectrum resulting from this parameter choice. Provided in section 2.4 is a description of how the initial state of the system may be prepared, followed by a detailed analysis of the creation of the many-body states and the associated excitation spectra for each of the three lattice geometries. This section concludes with an explanation of the source of the common features seen in each geometry and a brief analysis of how they are affected by the introduction of atomic position uncertainty. Before making use of these many-body states to create quantum states of light, section 2.5 describes a numerical method for exact diagonalisation of the Hamiltonian, subsequently comparing these exact results with those valid only in the strong laser driving regime. Following from the comparison of these results, section 2.6 presents the full derivation of how the atomic excitations may be mapped onto quantum states of light, and culminates in an expression for the angular density matrix

of the resulting photonic state. Concluding the research part of this chapter, section 2.7 illustrates the photonic distributions expected from the most likely excited states of the three lattice geometries before going on to describe their robustness when atomic positional uncertainty is introduced. Finally, the chapter concludes in section 2.8, where a brief summary of the results is provided, along with suggestions for possible extensions.

2.2 System and Hamiltonian

The system and its Hamiltonian are described in this opening section. Initially the focus will be on the Hamiltonian describing the atoms in the lattice and how this may be solved under certain conditions and how the resulting excited states may be accessed. The work laid out here is then used in sections 2.6 and 2.7, which show how photonic states may be produced from the atomic excitations and provide an analysis of these, respectively. The main element of the system is a gas of atoms trapped in a regular two-dimensional lattice with a total of N sites. The lattice spacing a is of the order of a few micrometres and each site is to be considered deep, such that the vibrational states within each site are well approximated by the harmonic oscillator eigenstates and tunnelling between the sites is absent. In this setup, the lattice is uniformly filled with a single atom per site, the internal degrees of freedom of which are approximated by a two-level system¹. These two levels are the ground state, $|g\rangle$, and a Rydberg ns -state, $|r\rangle$, where n is the principal quantum number and s refers to the angular momentum quantum number l being zero. This lattice system is subject to a laser with Rabi frequency Ω_0 and detuning Δ which couples the two atomic states. A diagram showing the lattice parameters and the internal level scheme of the

¹This is a simplified picture of the atom as the Rydberg states are typically accessed via two-photon absorption [117], where a third off-resonant state is used as an intermediate step in the excitation process

atoms can be seen in Fig. 2.1(a), where the aim to produce non-classical photons

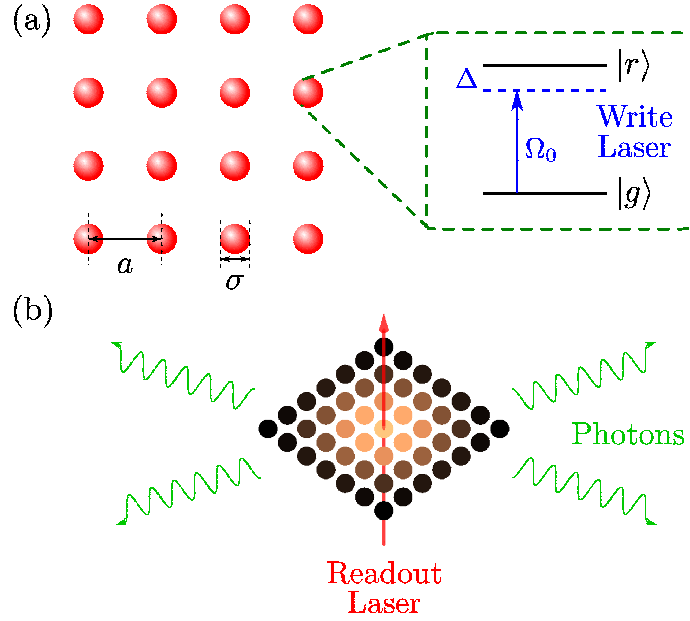


Figure 2.1: (a) A diagram showing the two dimensional square lattice with lattice spacing a and the internal level structure of each individual trapped atom. How the laser with Rabi frequency Ω_0 is used to write a specific collective excitation state onto the lattice is described in section 2.4.1.(b) An illustration of the intended photon production from a collective excitation stored in the lattice. This process uses a second laser, with the resulting photonic states shown in section 2.7.

from such a lattice is illustrated in part (b) of the figure. This figure shows the specific example of a square lattice, though other geometries are considered in the following sections.

The Hamiltonian of the non-interacting system may be written as

$$H_0 = \Omega_0 \sum_{i=1}^N \left(\hat{b}_i^\dagger \hat{r}_i + \hat{r}_i^\dagger \hat{b}_i \right) + \Delta \sum_{i=1}^N \hat{n}_i, \quad (2.1)$$

where \hat{b}_i^\dagger (\hat{b}_i) and \hat{r}_i^\dagger (\hat{r}_i) define the bosonic creation (annihilation) operators of a ground state or Rydberg atom in the lowest vibrational eigenstate of lattice site i , respectively, with \hat{n}_i the number operator for Rydberg atoms at site i , defined

as

$$\hat{n}_i = \hat{r}_i^\dagger \hat{r}_i.$$

It should be noted that atomic units are used throughout this chapter, the definitions of these being given in appendix A. The atoms in the lattice interact when in the Rydberg state via the van der Waals interaction. This scales as C_6/r^6 where r is the distance between the two atoms, therefore being heavily dependent on the lattice spacing a . The notation C_6 in this interaction represents a polynomial in the principal quantum number of the atom, having a leading power of n^{11} for ns -states [73], thus illustrating one of the reasons why Rydberg atoms are such attractive candidates for strongly interacting lattice systems. With the presence of such a strong Rydberg-Rydberg interaction, ground-Rydberg and ground-ground interactions may safely be neglected here. The interaction Hamiltonian may thus be written as

$$H_{\text{int}} = \sum_{i \neq j} V_{ij} \hat{n}_i \hat{n}_j,$$

where the interaction coefficients are

$$V_{ij} = \frac{C_6}{2 |\mathbf{R}_i - \mathbf{R}_j|^6}, \quad (2.2)$$

with \mathbf{R}_i denoting the position of the atom at site i and the factor of $1/2$ compensating the double counting due to the summation over both i and j .

As there are only two possible states in this regime it is possible to use spin-1/2 algebra in order to analyse the system. The two possible atomic states may therefore be represented as

$$|g\rangle_i = \begin{pmatrix} 0 \\ 1 \end{pmatrix}^{(i)} \quad \text{and} \quad |r\rangle_i = \begin{pmatrix} 1 \\ 0 \end{pmatrix}^{(i)}.$$

A set of ladder operators may subsequently be defined using the Pauli matrices as

$$\hat{\sigma}_+^i = \frac{1}{2} (\hat{\sigma}_x^i + i\hat{\sigma}_y^i) \equiv \begin{pmatrix} 0 & 1 \\ 0 & 0 \end{pmatrix}^{(i)} \quad \text{and} \quad \hat{\sigma}_-^i = \frac{1}{2} (\hat{\sigma}_x^i - i\hat{\sigma}_y^i) \equiv \begin{pmatrix} 0 & 0 \\ 1 & 0 \end{pmatrix}^{(i)},$$

such that $\hat{\sigma}_+^i$ replaces a ground state atom by an excited atom at the site i , with $\hat{\sigma}_-^i$ doing the opposite. The atom laser Hamiltonian (2.1) is subsequently modified to include these ladder operators by performing the substitutions

$$\hat{b}_i^\dagger \hat{r}_i \rightarrow \hat{\sigma}_-^i \quad \text{and} \quad \hat{r}_i^\dagger \hat{b}_i \rightarrow \hat{\sigma}_+^i$$

to yield

$$H_0 = \sum_{i=1}^N \left[\Omega_0 \hat{\sigma}_x^i + \Delta \hat{n}_i \right], \quad (2.3)$$

where $\hat{\sigma}_x^i = \hat{\sigma}_+^i + \hat{\sigma}_-^i$ swaps the atomic state at site i . The number operator may also be conveniently written in terms of the Pauli matrices as

$$\hat{n}_i = \frac{1}{2} \left[\hat{\mathbb{I}}^i + \hat{\sigma}_z^i \right],$$

where $\hat{\mathbb{I}}^i$ represents a 2×2 identity matrix acting on site i . The total Hamiltonian of the system may thus be written as

$$H = \sum_{i=1}^N \left[\Omega_0 \hat{\sigma}_x^i + \Delta \hat{n}_i + \sum_{j \neq i} V_{ij} \hat{n}_i \hat{n}_j \right]. \quad (2.4)$$

Before finding the solution of this Hamiltonian, it is important to note that the ladder operators from which it is constructed obey neither bosonic or fermionic

algebra. Instead they obey the standard spin commutation relations [118]

$$\begin{aligned} \{\hat{\sigma}_+^i, \hat{\sigma}_-^i\} &= 1 \quad \text{and} \quad \{\hat{\sigma}_\pm^i, \hat{\sigma}_\pm^i\} = 0 \\ [\hat{\sigma}_+^i, \hat{\sigma}_-^j] &= \delta_{ij} \hat{\sigma}_z^i \quad \text{and} \quad [\hat{\sigma}_\pm^i, \hat{\sigma}_\pm^j] = 0 \quad \forall i, j, \end{aligned} \quad (2.5)$$

which obey anti-commutation and commutation relations whether they belong to the same or different sites, respectively. This algebra makes a solution of the system very difficult to find, as approximate procedures to solve these systems are more readily available for those which are either wholly bosonic or fermionic. The following section addresses this issue in two steps and within a certain parameter regime.

2.3 Solution of the Hamiltonian

This section describes the method used to obtain the eigenstates and eigenenergies of the Hamiltonian (2.4), which is only approximate and must be carried out in a specific parameter regime. The system is assumed to be in the *strong driving regime*, where the laser driving Ω_0 is its largest energy scale. This is represented as $\Omega_0 \gg V^{\text{nn}}, |\Delta|$, with $V^{\text{nn}} = C_6/a^6$ being the maximum strength of the interaction, which occurs between atoms in neighbouring lattice sites. As alluded to previously, the process of obtaining the approximate eigenvalues and eigenstates of the system in this regime will be performed in two steps. The first step is to make the dominant term diagonal, which is done by means of a unitary rotation of the form

$$U_R = \prod_{i=1}^N \exp \left[-i \frac{\pi}{4} \sigma_y^i \right] \equiv \prod_{i=1}^N \begin{pmatrix} \frac{1}{\sqrt{2}} & -\frac{1}{\sqrt{2}} \\ \frac{1}{\sqrt{2}} & \frac{1}{\sqrt{2}} \end{pmatrix}^{(i)},$$

and performs the transformations $\hat{\sigma}_z \rightarrow -\hat{\sigma}_x$ and $\hat{\sigma}_x \rightarrow \hat{\sigma}_z$. Application of this rotation to the Hamiltonian brings it into the form

$$\begin{aligned}
 H' = U_R^\dagger H_0 U_R = & \Omega_0 \sum_{i=1}^N \hat{\sigma}_z^i + \frac{\Delta}{2} \sum_{i=1}^N (\hat{\mathbb{I}} - \hat{\sigma}_x^i) + \frac{1}{4} \sum_{i \neq j} V_{ij} (\hat{\sigma}_+^i \hat{\sigma}_-^j + \hat{\sigma}_-^i \hat{\sigma}_+^j) \\
 & + \frac{1}{4} \sum_{i \neq j} V_{ij} (\hat{\sigma}_+^i \hat{\sigma}_+^j + \hat{\sigma}_-^i \hat{\sigma}_-^j) - \frac{1}{2} \sum_{i=1}^N V_{ij} \hat{\sigma}_x^i + \frac{1}{4} \sum_{i \neq j} V_{ij}, \quad (2.6)
 \end{aligned}$$

where it is clear that the first term is now diagonal. However, the problem remains that the ladder operators obey neither bosonic or fermionic algebra. The second step of the process is to remove this issue. As explained in the following section, this is achieved by application of the Holstein-Primakoff transformation, which expresses the Hamiltonian in terms of operators which obey purely bosonic algebra.

2.3.1 The Holstein-Primakoff Transformation

This section will detail how the Holstein-Primakoff transformation [119] is used to convert the spin operators introduced in the previous sections into operators which obey purely bosonic algebra. The previous work on Rydberg atoms trapped in a ring configuration [90] used the Jordan-Wigner transformation [120] to convert the spin operators to those which obey canonical fermionic algebra. Analogues for this transformation in two dimensions are very complex [121], and so this alternative Holstein-Primakoff method is used. Following the notation used in [122], the Holstein-Primakoff transformation makes the following substi-

tutions

$$\begin{aligned}\hat{\sigma}_-^i &\rightarrow \sqrt{2S} \sqrt{1 - \frac{\hat{a}_i^\dagger \hat{a}_i}{2S}} \hat{a}_i \\ \hat{\sigma}_+^i &\rightarrow \sqrt{2S} \hat{a}_i^\dagger \sqrt{1 - \frac{\hat{a}_i^\dagger \hat{a}_i}{2S}} \\ \hat{\sigma}_z^i &\rightarrow 2 \left(\hat{a}_i^\dagger \hat{a}_i - S \right),\end{aligned}$$

with S being the spin of each particle and \hat{a}_i^\dagger (\hat{a}_i) bosonic operators creating (annihilating) non-interacting bosonic excitations at the site i . These transformed operators obey the original spin commutation relations (2.5), thus preserving the physics of the system. As spin-1/2 algebra has been used to describe the system up to this point, this transformation may be simplified by inserting $S = 1/2$ to yield the final transformation,

$$\begin{aligned}\hat{\sigma}_-^i &\rightarrow \sqrt{1 - \hat{a}_i^\dagger \hat{a}_i} \hat{a}_i \\ \hat{\sigma}_+^i &\rightarrow \hat{a}_i^\dagger \sqrt{1 - \hat{a}_i^\dagger \hat{a}_i} \\ \hat{\sigma}_z^i &\rightarrow 2 \left(\hat{a}_i^\dagger \hat{a}_i - \frac{1}{2} \right).\end{aligned}\tag{2.7}$$

At this point, the transformed ladder operators may be inserted into the Hamiltonian (2.6), which allows it to be rewritten as

$$\begin{aligned}H_{\text{HP}} &= 2\Omega_0 \sum_{i=1}^N \left(\hat{a}_i^\dagger \hat{a}_i - \frac{1}{2} \right) - \frac{\Delta}{2} \sum_{i=1}^N \left[\hat{a}_i^\dagger \left(1 - \hat{a}_i^\dagger \hat{a}_i \right)^{\frac{1}{2}} + \left(1 - \hat{a}_i^\dagger \hat{a}_i \right)^{\frac{1}{2}} \hat{a}_i \right] \\ &\quad + \frac{1}{4} \sum_{i \neq j} V_{ij} \left[\hat{a}_i^\dagger \left(1 - \hat{a}_i^\dagger \hat{a}_i \right)^{\frac{1}{2}} \hat{a}_j^\dagger \left(1 - \hat{a}_j^\dagger \hat{a}_j \right)^{\frac{1}{2}} + \left(1 - \hat{a}_i^\dagger \hat{a}_i \right)^{\frac{1}{2}} \hat{a}_i \left(1 - \hat{a}_j^\dagger \hat{a}_j \right)^{\frac{1}{2}} \hat{a}_j \right. \\ &\quad \left. + \hat{a}_i^\dagger \left(1 - \hat{a}_i^\dagger \hat{a}_i \right)^{\frac{1}{2}} \hat{a}_i \left(1 - \hat{a}_j^\dagger \hat{a}_j \right)^{\frac{1}{2}} \hat{a}_j + \left(1 - \hat{a}_i^\dagger \hat{a}_i \right)^{\frac{1}{2}} \hat{a}_i \hat{a}_j^\dagger \left(1 - \hat{a}_j^\dagger \hat{a}_j \right)^{\frac{1}{2}} \right] \\ &\quad - \frac{1}{2} \sum_{i \neq j} V_{ij} \left[\hat{a}_i^\dagger \left(1 - \hat{a}_i^\dagger \hat{a}_i \right)^{\frac{1}{2}} + \left(1 - \hat{a}_i^\dagger \hat{a}_i \right)^{\frac{1}{2}} \hat{a}_i \right] + \sum_{i=1}^N \left\{ \frac{1}{4} \sum_{i \neq j} V_{ij} + \frac{\Delta}{2} \right\}.\end{aligned}\tag{2.8}$$

Up to this point this transformation is exact, though it has introduced square roots of bosonic operators, which are difficult to treat in practical calculations. For this reason, the approximation is made that the system will remain in a subspace where the total number of bosonic excitations present is much smaller than the number of sites. This may be expressed as

$$N_b = \sum_i \langle \hat{a}_i^\dagger \hat{a}_i \rangle \ll N,$$

such that the boson number expectation value $\langle \hat{a}_i^\dagger \hat{a}_i \rangle \ll 1$ for all sites i . This allows what is referred to in [122] as the ‘ $1/S$ expansion’ to be performed, which is a Taylor expansion of the square roots in the Hamiltonian (2.8) about $\langle \hat{a}_i^\dagger \hat{a}_i \rangle = 0$. This yields

$$\sqrt{1 - \hat{a}_i^\dagger \hat{a}_i} \approx 1 - \frac{\hat{a}_i^\dagger \hat{a}_i}{2} - \frac{\hat{a}_i^\dagger \hat{a}_i}{8} - \frac{\hat{a}_i^\dagger \hat{a}_i \hat{a}_i \hat{a}_i}{8} + \dots$$

where the operators have been put in normal order [123]. The $1/S$ expansion is further explained in [124]. Substituting this expansion into the Hamiltonian and keeping only terms quadratic or lower in the bosonic operators yields the approximate Hamiltonian of the system in the low excitation number subspace

$$\begin{aligned} H_{\text{HP}} \approx & 2\Omega_0 \sum_{i=1}^N \left(\hat{a}_i^\dagger \hat{a}_i - \frac{1}{2} \right) - \frac{\Delta}{2} \sum_{i=1}^N \left(\hat{a}_i^\dagger + \hat{a}_i \right) \\ & + \frac{1}{4} \sum_{i \neq j} V_{ij} \left[\hat{a}_i^\dagger \hat{a}_j^\dagger + \hat{a}_i \hat{a}_j + \hat{a}_i^\dagger \hat{a}_j + \hat{a}_j^\dagger \hat{a}_i \right] \\ & - \frac{1}{2} \sum_{i \neq j} V_{ij} \left(\hat{a}_i^\dagger + \hat{a}_i \right) + \sum_{i=1}^N \left(\frac{\Delta}{2} + \frac{1}{4} \sum_{i \neq j} V_{ij} \right), \end{aligned} \quad (2.9)$$

the terms and eigenstates of which are analysed in the following section.

2.3.2 Constrained Dynamics

The final bosonic Hamiltonian (2.9) shows that the two step diagonalisation process applied has achieved the diagonalisation of the laser driving term such that $\hat{\sigma}_x \rightarrow 2\hat{a}_i^\dagger \hat{a}_i - 1$. It is straightforward to show that the eigenstates of $\hat{\sigma}_x^{(i)}$ are

$$|\pm\rangle_i = \frac{1}{\sqrt{2}} \{ |g\rangle_i \pm |r\rangle_i \},$$

such that $\hat{\sigma}_x^i |\pm\rangle_i = \pm |\pm\rangle_i$. Using the diagonalised bosonic form of this operator it can be shown that the equivalent bosonic states are $|-\rangle_i \equiv |0\rangle_i$, where the site i is void of bosonic excitations, and $|+\rangle_i \equiv |1\rangle_i = \hat{a}_i^\dagger |0\rangle_i$, where a single excitation is present at the site. Therefore each eigenstate of the dominant laser driving term has a well defined number of bosonic excitations.

In further analysis, the system Hamiltonian (2.9) has four distinct terms, three of which have different effects on the on the number of bosonic excitations in the system. The Hamiltonian contains an overall energy offset, which does not change the relative energy levels of the system and is formed from those terms which do not contain any bosonic operators,

$$E_0 = -N \left(\Omega_0 - \frac{\Delta}{2} \right) + \frac{1}{4} \sum_{i \neq j} V_{ij}. \quad (2.10)$$

Following from this energy offset, there are those terms which will not change the number of excitations in the system,

$$H_1 = 2\Omega_0 \sum_{i=1}^N \hat{a}_i^\dagger \hat{a}_i + \frac{1}{4} \sum_{i \neq j} V_{ij} \left[\hat{a}_i^\dagger \hat{a}_j + \hat{a}_j^\dagger \hat{a}_i \right], \quad (2.11)$$

as they contain the same number of creation and annihilation operators. There are also a number of terms which may change the number of bosonic excitations

in the system by one, which may be gathered together to form

$$H_2 = -\frac{\Delta}{2} \sum_{i=1}^N (\hat{a}_i^\dagger + \hat{a}_i) - \frac{1}{2} \sum_{i \neq j} V_{ij} (\hat{a}_i^\dagger + \hat{a}_i), \quad (2.12)$$

and contain unpaired creation and annihilation operators. Finally, there are those terms which may change the number of bosonic excitations in the system by two at a time,

$$H_3 = \frac{1}{4} \sum_{i \neq j} V_{ij} [\hat{a}_i^\dagger \hat{a}_j^\dagger + \hat{a}_i \hat{a}_j].$$

These three distinct terms therefore form the full Hamiltonian as

$$H_{\text{HP}} = E_0 + H_1 + H_2 + H_3$$

and may be used to describe the dynamics of the system.

The excitation number conserving part of the Hamiltonian (2.11) contains the dominant laser driving term. This defines a coarse energy structure of the system where manifolds of quasi-degenerate states are separated by energy gaps of approximately $2\Omega_0$. These manifolds are formed by the states where the number of bosonic excitations in the system, N_b , is the same. An illustration of this energy structure is given in Fig. 2.2, where the actions of the different parts of

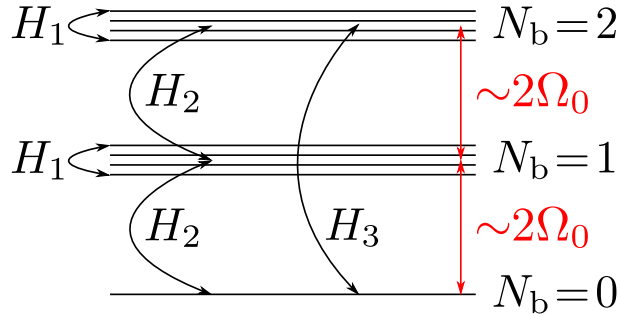


Figure 2.2: An illustration of how the manifolds of the system are defined by the number of bosonic excitations present, N_b . Also shown is how the three parts of the Hamiltonian can stimulate transitions between/within the manifolds.

the Hamiltonian are also shown. The second term in H_1 does not change the number of excitations in any given state of the system, thus it couples states in the same manifold and can be seen to have a strength of the order of the terms in V_{ij} . The remaining parts of the full Hamiltonian, H_2 and H_3 , create or destroy one or two bosonic excitations in the system, respectively. As a result, the states that they couple are separated in energy by $2\Omega_0$ and $4\Omega_0$ respectively. The associated transitions are therefore strongly suppressed and using second order perturbation theory [125] may be shown to have rates proportional to Δ^2/Ω and $(V^{\text{nn}})^2/\Omega$, which are very small quantities in the strong driving regime.

As a result of the chosen parameter regime, it is clearly the Hamiltonian H_1 (2.11) which governs the dynamics of the entire system. Therefore, to obtain the form of the eigenexcitations of the system in this regime, H_1 requires diagonalisation. Since the first term of H_1 is already diagonal this amounts to the diagonalisation of V_{ij} as

$$\sum_{ij} U_{ki}^\dagger V_{ij} U_{jm} \equiv D_{km},$$

where D_{km} is a diagonal matrix containing its eigenvalues. Using $V_{ij} \equiv V_{ji}$, this diagonalisation process allows this part of the Hamiltonian to be written as

$$H_1 = \sum_k \varepsilon_k \hat{b}_k^\dagger \hat{b}_k, \quad (2.13)$$

where the operators \hat{b}_k^\dagger are defined as

$$\hat{b}_k^\dagger = \sum_{i=1}^N \hat{a}_i^\dagger U_{ik} \quad (2.14)$$

and the eigenvalues $\varepsilon_k = 2\Omega_0 + D_k/2$. Hence it can be seen that the operator \hat{b}_k^\dagger creates a collective excitation of energy ε_k in the system, as it is defined as a superposition of all the single site excitation operators \hat{a}_i^\dagger , where the coefficients

are given by the eigenvectors of V_{ij} .

It is now possible to write down the approximate eigenstates of the system and their corresponding eigenenergies. The ground state of the system is that which contains no bosonic excitations, such that it may be written as

$$|0\rangle = \prod_{i=1}^N |0\rangle_i, \quad (2.15)$$

where $|0\rangle_i$ is the state where there are no bosonic excitations present at site i . This state has energy E_0 as defined in equation (2.10). There are N possible states of the first excited manifold, as there are N different \hat{b}_k^\dagger creation operators. These may then be written

$$|1_k\rangle = \hat{b}_k^\dagger |0\rangle \quad (2.16)$$

and have eigenenergies given as $E_{1_k} = E_0 + \varepsilon_k$. Making sure not to repeat any of the combinations of two excitations in the system (ensured by taking $j \geq i = 1, 2, \dots, N$), the manifold with $N_b = 2$ has $N(N+1)/2$ possible states, which are written as

$$|2_{ij}\rangle = \frac{1}{\sqrt{1 + \delta_{ij}}} \hat{b}_i^\dagger \hat{b}_j^\dagger |0\rangle \quad (2.17)$$

and have energy $E_{2_{ij}} = E_0 + \varepsilon_i + \varepsilon_j$. A state with any number N_b of bosonic excitations may be created by application of N_b collective excitation creation operators to the zero excitation state, $|0\rangle$. The limit on the number comes in the form of the previously described $1/S$ expansion, which means that the Hamiltonian H_1 (2.11) is only valid in the limit where the number of bosonic excitations is much smaller than the number of sites of the lattice.

This section has detailed how an approximate bosonic description of the system may be formed in the strong laser driving regime. This allows the Hamiltonian to be split up into terms describing inter- and intra-manifold couplings, where the manifolds themselves are denoted by the number of bosonic excita-

tions present in the system. The following section details how the ground state of the system may be formed experimentally and the transitions to the collective excitation states stimulated.

2.4 Excitation of the Many-Particle States

This section describes how the many particle states of the system may be accessed experimentally. The method detailed here follows the description in [126] that was first proposed in [89, 90]. The state in which the experiment is initially prepared will be that where all atoms are in the ground state $|g\rangle$, which may be written as

$$|\text{init}\rangle = \prod_i |g\rangle_i.$$

The first step in the process aimed at generating the collective excitations is to create from this experimental starting point the ground state of the Hamiltonian H_1 (2.11), which is given in the previous section as equation (2.15). The process described here will consist of two laser pulses, and requires that the atom has a third available state, which will be labelled as $|s\rangle_i$, and in practice may correspond to an extra state of the hyperfine ground state manifold. This new level scheme can be seen in Fig. 2.3, which also shows the Rabi frequencies of the lasers that will be used to make the atoms undergo state transitions. Note that the two lasers shown in this diagram are only to be used in this state preparation as a sequence of pulses with a given duration, where the previously mentioned laser of frequency Ω_0 is turned off. This is also a simplified picture of the atom, as accessing the Rydberg state $|r\rangle$ will often require multiple photon absorption. The first laser pulse is of the laser with Rabi frequency Ω_{gs} , which is on resonance with the transition $|g\rangle_i \rightarrow |s\rangle_i$, and has a duration of $\tau_1 = \pi/(2\Omega_{\text{gs}})$. As described in the context of the Rabi model of absorption and emission of radiation by atoms

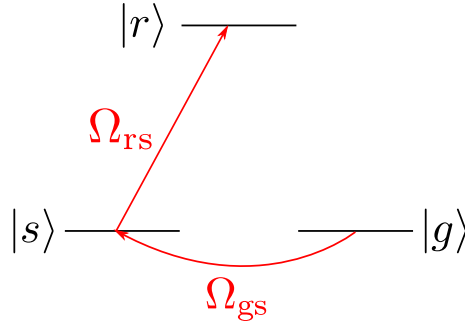


Figure 2.3: The level scheme of the atom and the Rabi frequencies connecting them where a second stable state $|s\rangle$ has been introduced. This stable state may in practice be an extra state of the hyperfine ground state manifold.

in [47], a pulse of this duration relative to the transition frequency is known as a $\pi/2$ -pulse, and leaves the atom in a coherent superposition state between the two states involved. This first laser pulse thus produces the transition

$$\prod_i |g\rangle_i \xrightarrow{\tau_1} \prod_i \frac{1}{\sqrt{2}} \{|g\rangle_i + i |s\rangle_i\}.$$

The second pulse is of the laser with Rabi frequency Ω_{rs} , which is on resonance with the atomic transition $|s\rangle_i \rightarrow |r\rangle_i$. This pulse has duration $\tau_2 = \pi/\Omega_{rs}$, which constitutes a π -pulse and transfers the population of the state $|s\rangle_i$ to $|r\rangle_i$. This second laser may be represented as

$$\prod_i \frac{1}{\sqrt{2}} \{|g\rangle_i + i |s\rangle_i\} \xrightarrow{\tau_2} \prod_i \frac{1}{\sqrt{2}} \{|g\rangle_i - |r\rangle_i\} \equiv |0\rangle,$$

whose result is the state in which all atoms are in the state $|-\rangle$, and is the desired ground state of the bosonic Hamiltonian. In order for this process to be efficient, the laser with Rabi frequency Ω_{rs} has to be strong enough to overcome the energy shifts due to the interaction between Rydberg atoms, which are explained in section 1.3.1. Thus to avoid reductions in efficiency of the second laser pulse due to the Rydberg blockade the second laser must fulfill $\Omega_{rs} \gg N_{nn} \times V^{nn}$, where N_{nn}

is the number of nearest neighbours to each site for the particular two-dimensional geometry.

Having explained how the ground state of H_1 (2.11) may be prepared experimentally, the following will explain how varying the experimental parameters allows the collective excitation states of the system to be accessed. This explanation follows that for the one-dimensional Rydberg lattice described in [75]. The transitions induced will take the system from the ground state with $N_b = 0$ and energy E_0 to those where a small number of collective bosonic excitations are present. The transfer of the system between different N_b manifolds may be brought about in single steps by the use of the laser detuning term of H_2 (2.12),

$$H_\Delta = -\frac{\Delta}{2} \sum_{i=1}^N (\hat{a}_i^\dagger + \hat{a}_i), \quad (2.18)$$

due to the fact that it may create or annihilate single bosonic excitations in the system. A problem with using this parameter to induce transitions is the suppression due to implementation of the strong laser driving regime, as explained in section 2.3.2. However, what is particularly useful about this term is the fact that the detuning is a controllable quantity, and by making it oscillate such that

$$\Delta(t) = \Delta_{\text{osc}} \cos(\omega_\Delta t),$$

it is possible to couple the manifolds when the frequency ω_Δ matches the energy between them. The details of this process are outlined in the next section.

2.4.1 Addressing the Many-Body States

The first part of this section details how the oscillating detuning will allow transitions to be induced between the bosonic ground state $|0\rangle$ and those states where a single bosonic excitation is present, $|1_k\rangle = \hat{b}_k^\dagger |0\rangle$. This method is used exten-

sively for the ring lattice in [75, 89, 90] and here a more detailed derivation will be presented of the results obtained in [126]. Being interested only in the diagonal part of the Hamiltonian, H_1 (2.13), which defines the energy levels of the states, and the detuning term, the matrix elements of the Hamiltonian $H = H_1 + H_\Delta$ may be shown to be

$$\begin{aligned}\langle 1_k | H | 1_k \rangle &= \varepsilon_k \\ \langle 1_k | H | 0 \rangle &= -\frac{\Delta_{\text{osc}}}{2} \sum_q U_{kq}^\dagger \cos(\omega_\Delta t) \\ \langle 0 | H | 1_k \rangle &= -\frac{\Delta_{\text{osc}}}{2} \sum_q U_{qk} \cos(\omega_\Delta t) \\ \langle 0 | H | 0 \rangle &= 0,\end{aligned}$$

where the energy offset E_0 has been set to zero. The first step to show that the oscillating detuning may make the system undergo transitions is to move to a frame of reference which rotates with the same frequency as the detuning. This is achieved with a unitary rotation of the form

$$U_\Delta = \begin{pmatrix} e^{i\omega_\Delta t} & 0 \\ 0 & 1 \end{pmatrix},$$

within which, as explained in appendix C, an effective Hamiltonian H' may be defined as

$$H' = U_\Delta H U_\Delta^\dagger - i U_\Delta \partial_t U_\Delta^\dagger$$

which acts on the rotated states of the system, $U_\Delta |0\rangle$ and $U_\Delta |1_k\rangle$. The matrix form of the effective Hamiltonian after the rotating wave approximation [127]

may be written as

$$H' = \begin{pmatrix} \varepsilon_k - \omega_\Delta & 0 \\ 0 & 0 \end{pmatrix} - \frac{\Delta_{\text{osc}}}{4} \sum_q \begin{pmatrix} 0 & U_{kq}^\dagger \\ U_{qk} & 0 \end{pmatrix},$$

which shows that, in this frame, the ground and first excited manifolds are brought closer together by an energy of ω_Δ . Thus, when the oscillation frequency ω_Δ is tuned to match the energy gap between the manifolds, it effectively acts as an on resonance laser with a Rabi frequency proportional to Δ_{osc} . The effective Rabi couplings between the states may be quantified by the intensity of this effective laser, which is calculated as the absolute value squared of the transition (off-diagonal) matrix elements.

The first transition which has to occur is that from the ground state $|0\rangle$ to one of the states in the first excited manifold. The intensity of these transitions can be calculated as

$$I_1(k) \equiv |\langle 0 | H' | 1_k \rangle|^2 = \frac{|\Delta_{\text{osc}}|^2}{16} \left| \sum_{q=1}^N U_{qk} \right|^2. \quad (2.19)$$

The validity of the rotating wave approximation as considered in [128, 129], implies that in this particular implementation the energy difference between the manifolds ($\sim \Omega_0$) must be much larger than the detuning, i.e. $|\Delta_{\text{osc}}| \ll \Omega_0$, which is already ensured in this strong laser driving regime. Also, in defining the above transition intensity, the assumption has been made that only the ground state $|0\rangle$ and a single state in the first excited manifold $|1_k\rangle$ are involved, thus forming a two-level description. Such an approximation is only valid if the separation between the levels within a manifold is much larger than the Rabi frequency of the inter-manifold transitions. In this system, the energy separation of the states within a manifold is proportional to V^{nn} with the effective Rabi frequency being

proportional to Δ_{osc} . This requirement therefore refines further the inequality describing the constrained dynamics, such that now $|\Delta_{\text{osc}}| \ll V^{\text{nn}}$ must also be ensured.

The intensity of the transitions from the states of the first excited manifold to those of the second excited manifold may be calculated using the same procedure as those from the ground state. Perhaps the most important feature results from the matrix elements of the Hamiltonian when the states $|1_k\rangle$ (2.16) and $|2_{ij}\rangle$ (2.17) are the involved states, which may be shown to be

$$\begin{aligned}\langle 2_{ij} | H | 2_{ij} \rangle &= \frac{1}{1 + \delta_{ij}} (\varepsilon_i + \varepsilon_j) \\ \langle 2_{ij} | H | 1_k \rangle &= \frac{1}{\sqrt{1 + \delta_{ij}}} \frac{\Delta_{\text{osc}}}{2} \sum_q \left(\delta_{kj} U_{iq}^\dagger + \delta_{ki} U_{jq}^\dagger \right) \cos(\omega_\Delta t) \\ \langle 1_k | H | 2_{ij} \rangle &= \frac{1}{\sqrt{1 + \delta_{ij}}} \frac{\Delta_{\text{osc}}}{2} \sum_q \left(\delta_{kj} U_{qi} + \delta_{ki} U_{qj} \right) \cos(\omega_\Delta t) \\ \langle 1_k | H | 1_k \rangle &= \varepsilon_k.\end{aligned}$$

The time-dependent part of these elements is once again removed using the procedure of moving to a rotating frame of reference and applying the rotating wave approximation, as previously discussed. The intensity of the transition is then calculated as the square of the coupling matrix elements as

$$I_2(k; ij) \equiv |\langle 1_k | H | 2_{ij} \rangle|^2 = \frac{\delta_{kj} I_1(i) + \delta_{ki} I_1(j) + 2\delta_{kj}\delta_{ki} I_1(k)}{1 + \delta_{ij}}. \quad (2.20)$$

Stemming from the matrix elements themselves, it is clear that this intensity of the transition between these two manifolds will be zero unless at least one of the excitations present in the double excitation state is the same as that in the initial singly excited state. This fact appears in the delta functions in the numerator of the expression, which all require either $i = k$ or $j = k$ for the intensities to be non-zero. This is the first of two selection rules for the allowed excitations of the

system, the second stems from the geometry of the lattice and will be shown in the next section to affect transitions from the ground state as well as those to higher excitation states.

2.4.2 Excitation Properties

This section describes the properties of the states that are achievable using the method of the oscillating detuning previously outlined. This is done for three different lattice geometries: square, triangular and hexagonal. When the one-dimensional analogue of this system was proposed [75], it was possible to justify an approximation that only the nearest-neighbour interactions need be considered. This is due to the fact that the next-nearest-neighbour interaction is a factor $1/2^6 = 1/64$ weaker than that of the nearest-neighbour. In the three two-dimensional setups considered here, an explanation is provided of the limits of such an approximation. The collective states attainable will be described by the probability of the bosonic excitation being found at a single lattice site, and as this is common to all three geometries, is explained first.

A single excitation in the system created using the oscillating detuning may be written as $|1_k\rangle = \hat{b}_k^\dagger |0\rangle$ and has energy $E_{1_k} = E_0 + \varepsilon_k$. In order to picture the distribution of this collective excitation among the lattice sites, the expectation value

$$N_u(k) = \langle 1_k | \hat{n}_u | 1_k \rangle$$

may be evaluated, where $\hat{n}_u = \hat{a}_u^\dagger \hat{a}_u$ is the number operator for the bosonic excitation on the u^{th} lattice site. Using the definition of the collective excitation operators (2.14), this expectation value is shown to yield the simple result

$$N_u(k) \equiv |U_{uk}|^2.$$

This expression therefore describes the probability of finding a bosonic excitation on site u of the lattice considering that it contains the collective excitation state $|1_k\rangle$. Examples of these excitations can be seen throughout the following sections.

This procedure may be repeated for any number of excitations present in the system, although increasing complexity is encountered with increasing number of collective excitations. The position expectation value for two excitations in the system may be written as

$$N_u(i, j) = \langle 2_{ij} | \hat{n}_u | 2_{ij} \rangle,$$

where the double collective excitation states $|2_{ij}\rangle$ are as given in (2.17). The full expression for two excitations in the system follows from this as

$$N_u(i, j) = \frac{1}{1 + \delta_{ij}} \left[|U_{ui}|^2 + |U_{uj}|^2 + \delta_{ij} \left(U_{iu}^\dagger U_{uj} + U_{ju}^\dagger U_{ui} \right) \right],$$

examples of which are given in the following sections. It should be noted that the figures showing the transition intensities (Figs. 2.4-2.11) represent the various collective excitation states by their energy eigenvalue $D_k/2$, as given in section 2.3.2. The value of $2\Omega_0$ subtracted from the detuning oscillation frequency represents the energy separation between the excitation number manifolds.

Square Lattice

This section describes the achievable many-body states of the system when the atoms are held in a square lattice, a pictorial example of which may be seen in Fig. 2.1(a). In contrast to the one-dimensional case, in the square lattice the next-nearest-neighbour is a distance $\sqrt{2}a$ away, instead of $2a$, and there are four of them, instead of two. Therefore, the nearest-neighbour approximation is not valid for most sizes of square lattice. For the nearest-neighbour approxima-

tion to be valid, the interaction strength when there are only two neighbouring excited atoms in the system, V^{nn} , must be much greater than that where the maximum possible number of next-nearest-neighbours are excited, $V_{\text{max}}^{\text{nnn}}$. It may be shown that, for all sizes of square lattice, described by $L_{\text{sq}} = \sqrt{N}$, there are $(L_{\text{sq}} - 1)^2$ pairs of interacting atoms for those configurations where all possible next-nearest-neighbouring atoms are excited. As the distance between the next-nearest-neighbours is $\sqrt{2}a$, the previously given equality may be evaluated as

$$V^{\text{nn}} \gg V_{\text{max}}^{\text{nnn}} \implies \frac{C_6}{a^6} \gg (L_{\text{sq}} - 1)^2 \frac{C_6}{(\sqrt{2}a)^6}$$

The solution of this inequality yields the limit below which the nearest neighbour approximation is comfortably valid to be $L_{\text{sq}} \ll 4\sqrt{2} + 1 \approx 6.7$, which limits it to only small lattice sizes. For this reason, the full interaction matrix V_{ij} without the nearest-neighbour approximation is calculated and diagonalised in order to find the eigenvectors which appear in the expressions for the intensities I_1 (2.19) and I_2 (2.20) that are evaluated in this section.

The intensity profile for the transitions from the ground state to the first excited manifold in an $L_{\text{sq}} = 10$ square lattice are shown in Fig. 2.4, with insets showing the excitation position probability for the three single collective excitation states with the highest transition intensity. What is clear in the figure is that out of the one hundred possible single collective excitation states, there are less than ten states for which the transition intensity is finite. Furthermore, the state with the highest transition intensity is that with the highest energy, which in this notation is represented as $|1_N\rangle$.

A description of the intensities to the double excitation manifold is now given, making sure that the initial state is one which has a finite transition intensity from the ground state. In this case, the choice is made to have the starting single collective excitation state as the one with the highest transition intensity,

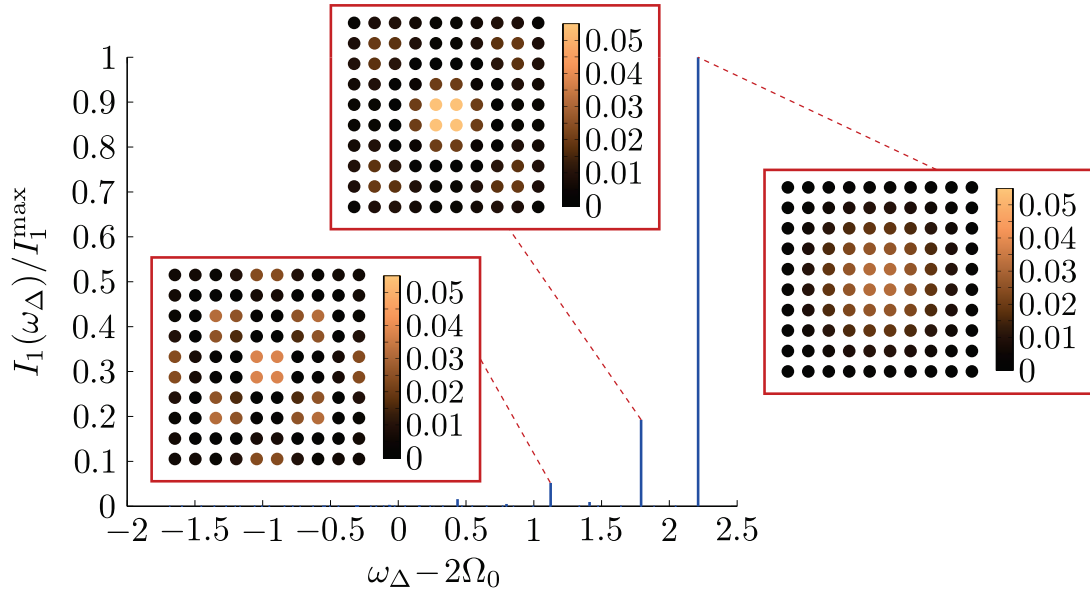


Figure 2.4: Normalised intensity profile for the transitions $|0\rangle \rightarrow |1_i\rangle$ for the $L_{\text{sq}} = 10$ square lattice. Inset are the excitation probability distributions for the three most likely excited collective excitation states. The energies are given in units of V^{nn} .

$|1_N\rangle$, as shown in Fig. 2.4. The intensities of the transitions from $|1_N\rangle \rightarrow |2_{iN}\rangle$ are shown in Fig. 2.5, which clearly shows that there are a limited number of accessible states. The insets showing the bosonic probability distributions of the three most likely excited double excitation states are very similar to those shown for the single excitation states in Fig. 2.4. The reason for this is that with one of the excitations being fixed as that which is already present in the system, the second excitation is effectively produced from the ground state of the system. Thus the most likely second excitations to be produced are those which are most likely produced from the ground state.

Triangular Lattice

This section gives details of the most likely excited states of a system where both the internal and external geometries are equilateral triangles, as is illustrated in Fig. 2.6. This figure shows a small triangular lattice with $L_{\text{tri}} = 4$ sites per side,

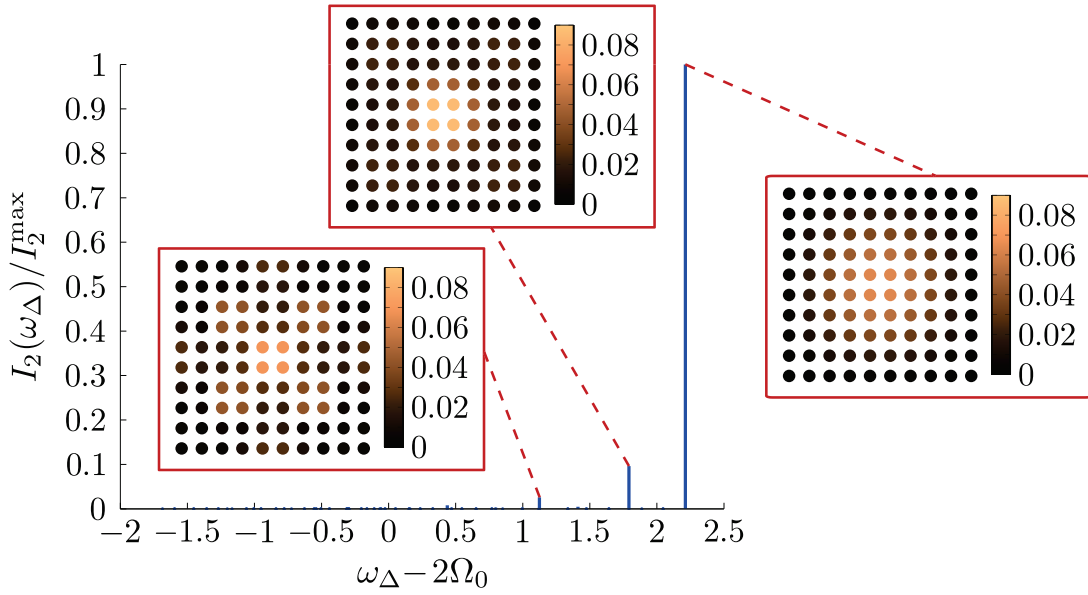


Figure 2.5: The normalised intensity profile for the transitions $|1_N\rangle \rightarrow |2_{iN}\rangle$ for an $L_{\text{sq}} = 10$ square lattice. Inset are the excitation probability distributions for the three most likely excited double collective excitation states. The energies are given in units of V^{nn} .

which is how the triangular lattices are characterised. For reference, the total number of sites is given by the binomial coefficient

$$N_{\text{tri}} = \binom{L_{\text{tri}} + 1}{2} \equiv \frac{(L_{\text{tri}} + 1)!}{2(L_{\text{tri}} - 1)!} = \frac{L_{\text{tri}}^2 + L_{\text{tri}}}{2}.$$

In the triangular lattice case, a central site (i.e. not near the edges of the lattice) has six nearest-neighbours and three next-nearest-neighbours, which are a distance $\sqrt{3}a$ away. Therefore, the expectation is that taking only nearest-neighbours to describe the interaction would be slightly more robust in the triangular case than for the square lattice, but will ultimately not hold for larger lattices. It may be shown that the number of pairs of next-nearest-neighbours in the triangular lattice is $(1/2)(L_{\text{tri}} - 2)(L_{\text{tri}} - 1)$. Following the same approach as detailed for the square lattice, the interaction energy when all the next-nearest-neighbouring atoms are excited must be less than that when only two neighbour-

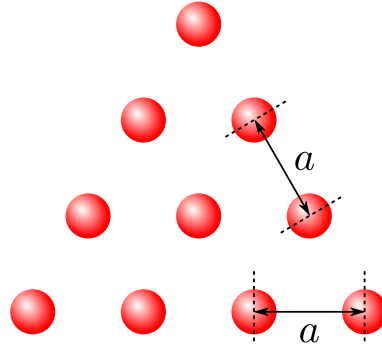


Figure 2.6: The equilateral triangular lattice with lattice spacing a which is considered in this section.

ing atoms are in the Rydberg state in order for the nearest-neighbour approximation to be valid. The inequality is thus formed as

$$V^{\text{nn}} \gg V_{\text{max}}^{\text{nnn}}(\text{tri}) \implies \frac{C_6}{a^6} \gg \frac{C_6(L_{\text{tri}}^2 - 3L_{\text{tri}} + 2)}{2(\sqrt{3}a)^6}$$

which after rearrangement may be solved to find $L_{\text{tri}} \ll 8.87$ in order for the nearest-neighbour approximation to be valid. As expected, this is a slightly greater number than that found for the square lattice, but ultimately is still a very tight constraint. Therefore, the full interaction matrix V_{ij} is diagonalised without using the nearest-neighbour approximation in order to find the transition intensities and state distributions described in this section.

The intensity profile for the transitions from the ground state to the first excited manifold in an $L_{\text{tri}} = 10$ triangular lattice are shown in Fig. 2.7, where the insets show the bosonic probability distributions of the three single collective excitation states with the highest transition intensities. As in the case of the square lattice, there are very few states which have a finite transition intensity. The state with the highest transition intensity in the triangular lattice is that with the highest energy, $|1_{N_{\text{tri}}}\rangle$, equivalent to the square lattice case. Also in line with the square lattice case, it appears that this is a collective excitation state where, upon repeated measurements, the bosonic excitation would most likely be

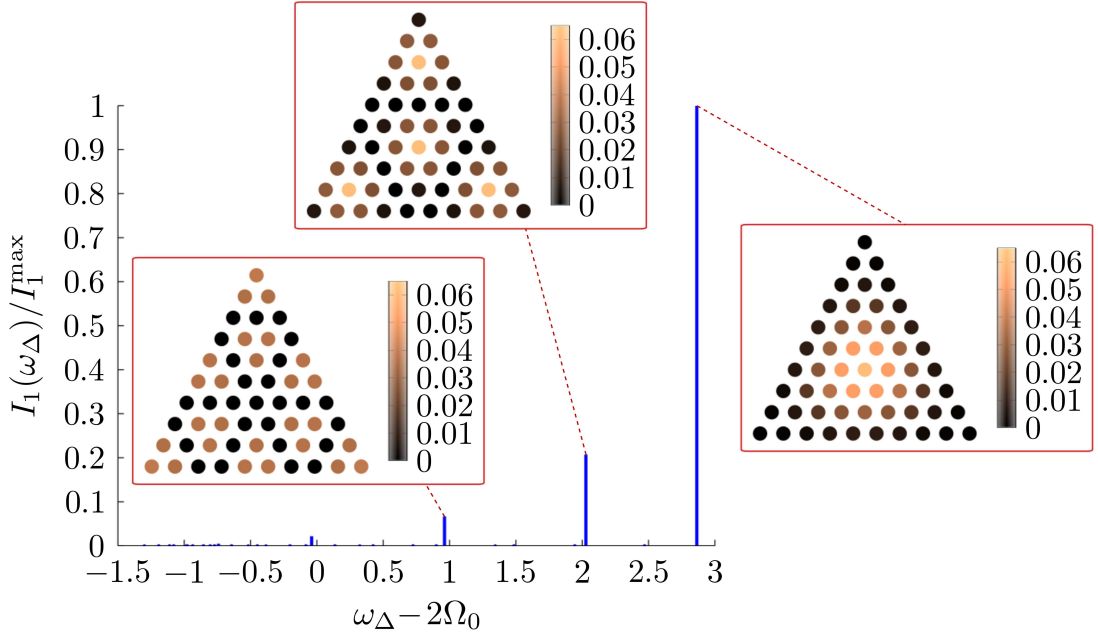


Figure 2.7: Normalised intensity profile for the transitions $|0\rangle \rightarrow |1_i\rangle$ for the $L_{\text{tri}} = 10$ triangular lattice. Inset are the excitation probability distributions for the three most likely excited collective excitation states. The energies are given in units of V^{nn} .

found at the centre of the lattice.

As previously described, the intensity of the transitions from the first excited states to the double collective excitation states may be calculated. As Fig. 2.7 shows the highest energy state, $|1_{N_{\text{tri}}}\rangle$, having the largest transition intensity, this state is chosen as the initial state from which to calculate the second order transition intensities $|1_{N_{\text{tri}}}\rangle \rightarrow |2_{iN_{\text{tri}}}\rangle$. The results of this calculation are illustrated in Fig. 2.8, which shows that the distributions of the accessible states are comprised of that of the initial $|1_{N_{\text{tri}}}\rangle$ state and those single collective excitation states which have the highest transition intensities from the ground state.

Hexagonal Lattice

This section details the most complicated system geometry which will be described; that of a hexagonal lattice where the external dimensions form a rhom-

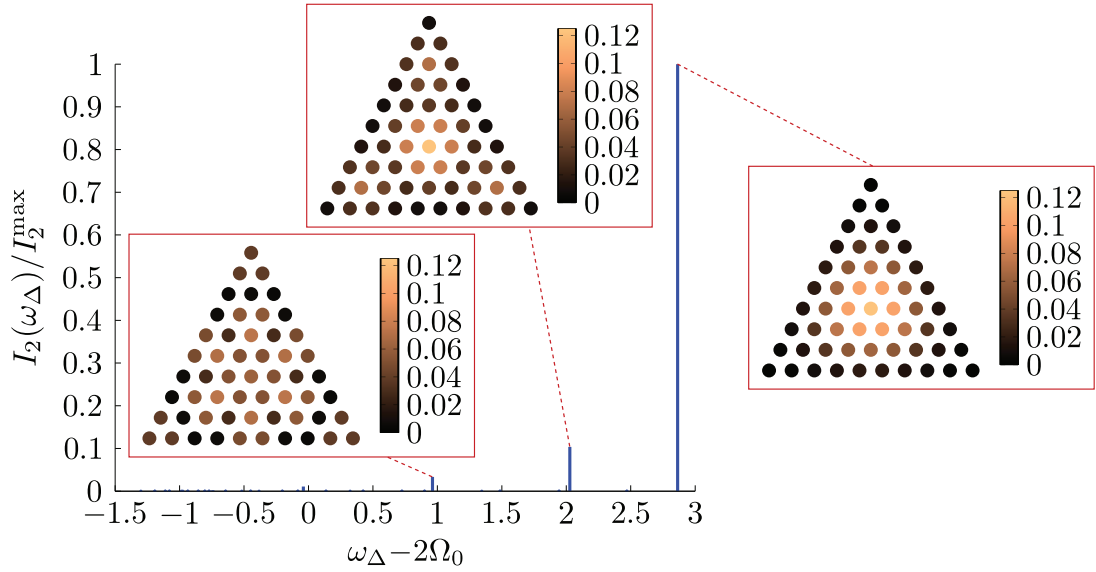


Figure 2.8: Normalised intensity profile for the transitions $|1_{N_{\text{tri}}}\rangle \rightarrow |2_{i_{N_{\text{tri}}}}\rangle$ for the $L_{\text{tri}} = 10$ triangular lattice. Inset are the excitation probability distributions for the three most likely excited double collective excitation states. The energies are given in units of V^{nn} .

bus. Such a lattice with $L_{\text{hex}} = 6$ is illustrated in Fig. 2.9, where the sites are

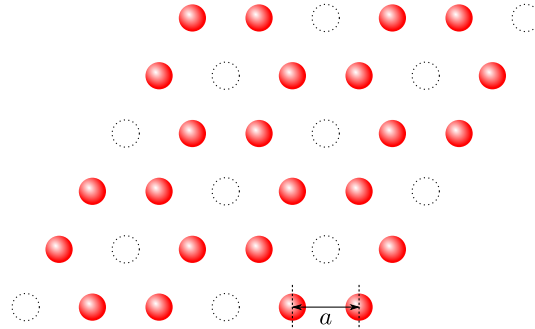


Figure 2.9: An illustration of the hexagonal lattice whose external geometry is a rhombus. Shown with dotted lines are the absent or unoccupied sites.

chosen such that there is never an occupied site in the tighter corner of the rhombus, thus making the analytic expressions (slightly) simpler to deal with. For reference, the number of sites in the lattice for a rhombus with L_{hex} sites per side (the characterising L_{hex} includes the dotted sites shown in Fig. 2.9) and the

restriction on where the sites are, may be calculated as

$$N_{\text{hex}} = \frac{2}{3}L_{\text{hex}}(L_{\text{hex}} - [L_{\text{hex}} \bmod 3]) + \delta_{[L_{\text{hex}} \bmod 3],1} \left(\frac{2L_{\text{hex}} + 2}{3} \right) + \delta_{[L_{\text{hex}} \bmod 3],2} \left(\frac{4L_{\text{hex}} - 2}{3} \right),$$

where $[a \bmod n]$ is the modulo operation and yields the remainder of a/n .

As shown for the previous geometries, first an analysis is presented showing why it is not possible to use the nearest-neighbour approximation in the two dimensional case. In this hexagonal case, each lattice site has three nearest-neighbours and six next-nearest-neighbours, which are each a distance of $\sqrt{3}a$ away. This is the opposite case to that of the triangular lattice, so it is expected that the hexagonal lattice is much less likely suited to the nearest-neighbour approximation. The number of pairs of next-nearest-neighbours in a hexagonal lattice formed from a rhombus of side length L_{hex} can be calculated as

$$N_{\text{nnn}}^{\text{hex}} = (L_{\text{hex}} - 2) L_{\text{hex}} - \left(\frac{L_{\text{hex}} - [L_{\text{hex}} \bmod 3]}{3} + 2 \right). \quad (2.21)$$

Thus, in order for the nearest-neighbour approximation to be valid, the case where only two neighbouring atoms are excited must have a much higher energy than that where all possible $N_{\text{nnn}}^{\text{hex}}$ next-nearest-neighbouring atoms are excited. This is not as straightforward as in previous cases, as the expression for the number of next-nearest-neighbours (2.21) clearly has the issue that there are effectively three conditions which depend on the value of $[L_{\text{hex}} \bmod 3]$. The choice is therefore made to use the situation where $[L_{\text{hex}} \bmod 3 = 2]$ as an example, as this is the worst case for the nearest-neighbour approximation as it has the highest number

of next-nearest-neighbour pairs. The inequality may then be written as

$$V^{\text{nn}} \gg V_{\text{max}}^{\text{nnn}}(\text{hex}) \implies \frac{C_6}{a^6} \gg \frac{C_6}{(\sqrt{3}a)^6} \left[(L_{\text{hex}} - 2)L_{\text{hex}} - \left(\frac{L_{\text{hex}} + 4}{3} + 2 \right) \right]$$

and may be solved to find the condition $L_{\text{hex}} \ll 6.62$ in order for the nearest-neighbour approximation to be valid. This has shown that, as expected, the nearest-neighbour approximation will only be valid for very small lattices, with a limit smaller than that found in both the triangular and square cases. Therefore, the following details the results gained using diagonalisation of the full interaction matrix without application of the nearest-neighbour approximation.

The intensity profile for the transitions from the ground state to the first excited state manifold of the $L_{\text{hex}} = 11$ hexagonal lattice is shown in Fig. 2.10, where the insets show the three single excitation states to which the transition

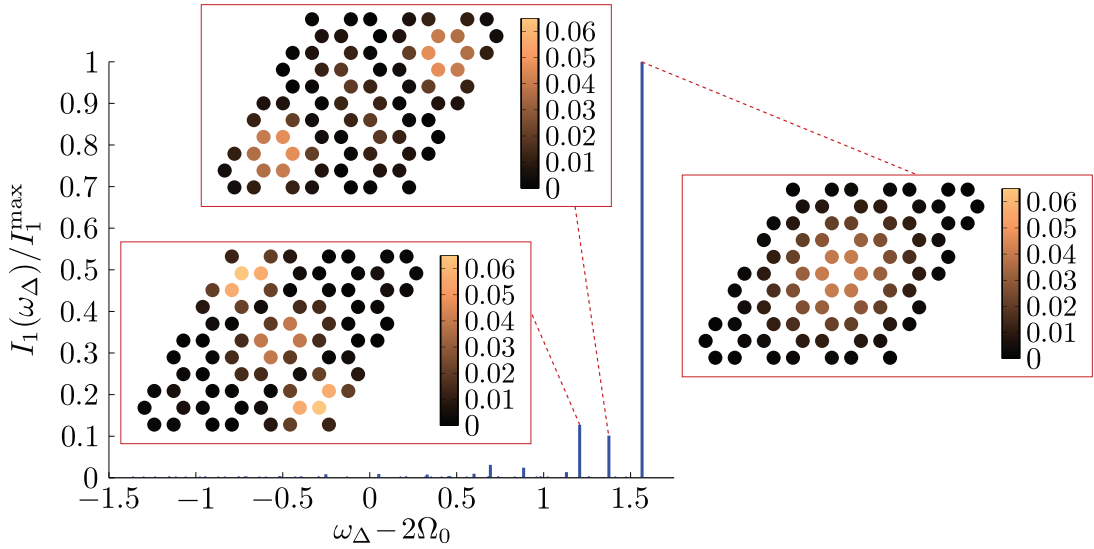


Figure 2.10: Normalised intensity profile for the transitions $|0\rangle \rightarrow |1_i\rangle$ for the $L_{\text{hex}} = 11$ hexagonal lattice. Inset are the excitation probability distributions for the three most likely excited collective excitation states. The energies are given in units of V^{nn} .

intensities are highest. Once again, the highest transition intensity corresponds to the single collective excitation state with the highest energy, $|1_{N_{\text{hex}}}\rangle$, which, as

precisely referred to in [126], is the closest state to a uniformly shared collective excitation.

In aiming to conclude the section showing the collective excitation states which are most likely generated, the final results presented here are those transition intensities from the most likely excited single excitation state, $|1_{N_{\text{hex}}}\rangle$ to the accessible states of the doubly excited manifold $|2_{iN_{\text{hex}}}\rangle$. These results are shown in Fig. 2.11, which shows that there is clearly one dominant peak, being that of the

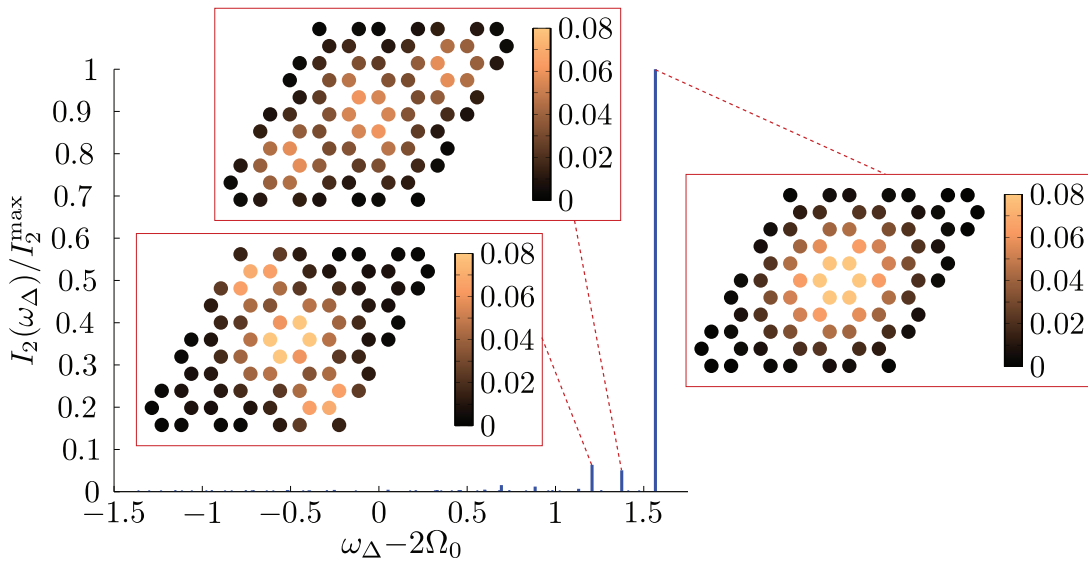


Figure 2.11: Normalised intensity profile for the transitions $|1_{N_{\text{hex}}}\rangle \rightarrow |2_{iN_{\text{hex}}}\rangle$ for the $L_{\text{hex}} = 11$ hexagonal lattice. Inset are the excitation probability distributions for the three most likely excited collective excitation states. The energies are given in units of V^{nn} .

transition intensity to the state containing two copies of the highest energy single excitation state. The secondary peaks correspond to those states containing the initial state and the second and third most likely excited single excitation states. What should be noted in both diagrams relating to the hexagonal lattice is that the second and third highest intensity peaks are very close to being of the same order, whereas in the previously explained cases there was a more pronounced gap in both the intensity and energy.

It has clearly been the case in all the geometries considered that the highest energy state always has the largest transition intensity. Increasing the system size in all cases only acts to increase the number of secondary peaks. The following section explains how, although belonging to different lattice geometries, these states have very similar properties.

2.4.3 Selection Rules for Accessing the Many-Body States

The previous sections concerned with various geometries of the system have shown that the majority of the transition intensities between the different excitation manifolds are zero. As this section explains, the reason for this is rooted in the symmetries of the various geometries, each of which will be considered here.

Each of the three geometries considered here belong to a different dihedral symmetry group [130], the square lattice belonging to D_4 , the triangular belonging to D_3 and the hexagonal (when constructed as described in section 2.4.2, with no sites in the tighter corners of the rhombus) D_2 . These three groups consist of the following transformations,

Square

- Cyclic group C_4 : Rotations of $2\pi n/4$ about the centre with $n = 1, 2, 3, 4$.
- F_x, F_y : Flips about the horizontal and vertical axes.
- F_u, F_v : Flips about the two main diagonals.

Triangular

- Cyclic group C_3 : Rotations of $2\pi n/3$ about the centre with $n = 1, 2, 3$.
- F_a, F_b, F_c : Flips about the three axes through the vertices.

Hexagonal

- Cyclic group C_2 : Rotations of $2\pi n/2$ about the centre with $n = 1, 2$.
- F_i, F_{ii} : Flips about the two axes running corner to corner.

which are illustrated in Fig. 2.12, where subfigure (c) makes clearer the require-

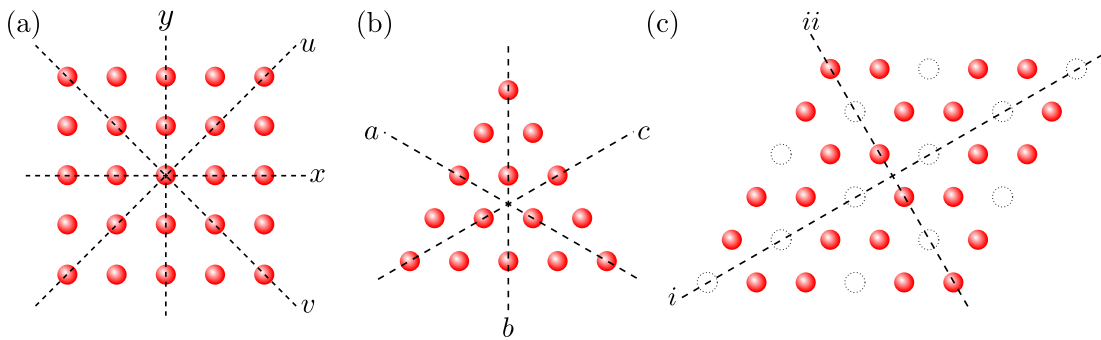


Figure 2.12: The three system geometries and their symmetries. (a) The square lattice showing the four symmetry axes. (b) The triangular lattice showing the three symmetry axes. (c) The hexagonal lattice showing the two axes of symmetry.

ment described in section 2.4.2, which ensures that the hexagonal lattice contained within the dimensions of a rhombus will always fulfil the two symmetries illustrated.

Upon inspection of both the full system Hamiltonian H , (2.4), and that describing the detuning in the bosonic system H_Δ , (2.18), it may be seen that they conserve all symmetries relating to the geometry of the system. This is justified by looking at the terms contained in each Hamiltonian: the full system Hamiltonian contains both a spin-flip term and two counting terms, with the detuning Hamiltonian creating or annihilating bosonic excitations at each site. As all the terms contained operate on each site independently and in the same way, both conserve all symmetries of the system itself. Therefore, when the initial state is an eigenstate of the previously quoted symmetry operators, the time evolution is restricted to the subspace spanned by states with the same quantum number with respect to these operators. The experimental initial state $|\text{init}\rangle$ describes when the atom at each lattice site is in the ground state. Moreover, the bosonic ground

state has each site void of bosonic excitations. Thus, these uniform states, being symmetric, are eigenstates of the all the operators which form the symmetry groups with eigenvalue $+1$. Such states which have eigenvalue $+1$ with respect to all symmetry operators of their geometry belong to the subspace A_1 , which is called totally symmetric. Therefore, only the collective excitation states which belong to the totally symmetric subspace may be accessed when the time evolution under Hamiltonians H and H_Δ is considered.

These symmetries explain why only a small number of the possible collective states of the system have non-zero transition intensities, as seen in the previous sections describing each of the three geometries. Furthermore, from the insets of the figures in these sections, the bosonic densities at each site of the lattice clearly show that the states with these finite transition intensities belong to the subspace A_1 . Of course, this reasoning is not restricted to only transitions from the ground state of the system. The previous section also detailed the transition from the singly to doubly excited states. The single collective excitation state is only accessible if it is a member of subspace A_1 , thus having eigenvalue $+1$ with respect to all symmetry operators of the system. The subsequent transition to the double collective excitation states once again uses the method of the oscillating detuning, therefore the same selection rules must be followed. It has already been documented that one of the collective states in the double excitation manifold must be the same as that present in the initial single excitation state. Including now these symmetry selection rules, there will only be the same number of possible transitions from each single excitation state as there is from the ground state to the single excitation manifold.

2.4.4 Transition Intensities to Imperfect Lattices

As detailed in the previous subsection, it is the geometry of the lattice which governs the transition profiles seen where only a handful of the possible states are likely to be excited. However, in an experimental setup the atoms are very unlikely to be fixed perfectly to the centres of the lattice sites. This short subsection details how the transition intensities between the ground and singly excited states are altered when uncertainty in the atomic position is introduced, as the symmetries discussed in the previous section are lifted.

To quantify the effect of the uncertainty in position, each atom is distributed at a random position about the centre of its respective lattice site with a finite standard deviation $\sigma \neq 0$, which is considered isotropic (see Fig. 2.1). Shown in Fig. 2.13 is the normalised transition intensity profile for an $L_{\text{sq}} = 10$

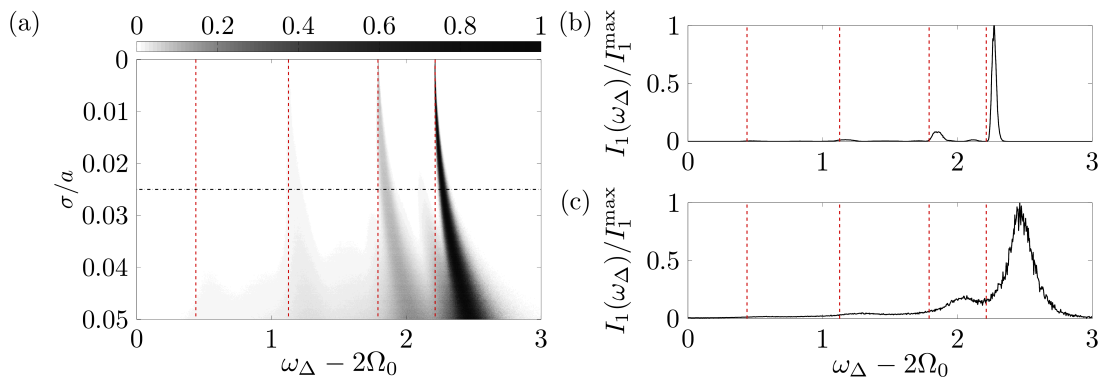


Figure 2.13: (a) Normalised intensity profile for the transition from the ground state to those in the single excitation manifold for an $L_{\text{sq}} = 10$ square lattice when the positions of the atoms are randomly distributed about the centre of the lattice sites with standard deviation σ . The red vertical lines show the position of the four most prominent transition intensities seen in Fig. 2.4. The horizontal black line shows the cross section of the profile seen in (b) for $\sigma/a = 0.025$. (c) The same cross section for $\sigma/a = 0.05$.

square lattice averaged over 10^4 realisations each of a range of uncertainties up to $\sigma/a = 0.05$. For each realisation, the system is initialised with atoms randomly distributed about the centre of each lattice site such that they fulfil the

desired position uncertainty. The full interaction matrix is then calculated and diagonalised followed by the calculation of the transition intensity to each single collective excitation state. At the end of each realisation of the same position uncertainty, the intensity results are summed to the previous ones and stored within discrete bins referring to the energy of each transition. It is these results for a range of different uncertainties which are normalised to the highest intensity and combined to form Fig. 2.13.

In Fig. 2.13, it is clear that as the uncertainty in atomic position increases, the initial sharp transition intensities become broader and shift towards higher energies. Such a shift towards higher energy transitions may be attributed to the lattice geometry, and may be explained by considering a shift in position of just a single atom. Consider a perfect lattice ($\sigma = 0$) where only a single atom may be moved from the centre of its lattice site. This atom may move in six possible directions, i.e. $\pm\hat{x}$, $\pm\hat{y}$ or $\pm\hat{z}$. If the atom moves in the xy -plane, it will be closer to at least one of its neighbouring atoms (considering here a lattice which is infinite in size). The atomic interaction thus increases, as it grows as $1/r^6$. Conversely, if the atom moves in the \hat{z} direction, it is definitely further away from its neighbours than previously, and the interaction is reduced. In this case of a single atom being allowed to move, four of the six possibilities give rise to a larger interaction energy. This therefore explains the overall shift of the transitions to higher energies observed in Fig. 2.13. Considering now a finite lattice size, as the number lattice sites increases, the proportion of the sites on its boundaries becomes smaller and therefore the shift to higher energies becomes more pronounced. The broadening of the transition lines may be attributed to the fact that the atoms are distributed randomly, meaning that the symmetry of the system discussed in section 2.4.3 is removed. Therefore, there are small but finite transition intensities to states that were not previously possible, and those

states which most closely resemble the states of the perfect lattice have varying energies depending on the particular atomic distribution.

The same analysis for an $L_{\text{sq}} = 7$ square lattice is produced in previous work [126], which will allow the reader to analyse how these results are common for varying lattice sizes. This same reasoning may be applied to either of the other lattice geometries previously considered.

Before going on to show how the collective excitations may be mapped onto quantum states of light, which is done in section 2.6, the following section details the steps towards an exact numerical diagonalisation of the Holstein-Primakoff transformed Hamiltonian (2.9). Such a diagonalisation procedure is subsequently applied and used to test the validity of the eigenstates and eigenenergies found in the strong laser driving regime.

2.5 Exact Diagonalisation of the Holstein Primakoff Hamiltonian

It is possible to perform an exact diagonalisation of the Holstein-Primakoff transformed Hamiltonian of this system (2.9) *without* being restricted to the strong driving regime which is documented in the preceding sections. This section follows the prescription detailed in [131] for the algorithm allowing such a diagonalisation, with necessary proofs reproduced and the conditions such that it is valid for this specific lattice Hamiltonian outlined. After the procedure has been detailed, it will be applied to the system Hamiltonian in order to provide a measure of the validity of the eigenspectrum found in the strong laser driving regime.

The original paper [131] details the diagonalisation of the quadratic boson

Hamiltonian, which may be written in the form

$$\mathcal{H} = \sum_{r',r=1}^m \left[\hat{\alpha}_{r'}^\dagger \mathcal{D}_{1r'r} \hat{\alpha}_r + \hat{\alpha}_{r'}^\dagger \mathcal{D}_{2r'r} \hat{\alpha}_r^\dagger + \hat{\alpha}_{r'} \mathcal{D}_{3r'r} \hat{\alpha}_r + \hat{\alpha}_{r'} \mathcal{D}_{4r'r} \hat{\alpha}_r^\dagger \right], \quad (2.22)$$

where $\hat{\alpha}$ ($\hat{\alpha}^\dagger$) are bosonic annihilation (creation) operators obeying the usual commutation relations and $\mathcal{D}_{nr'r}$ represents the element in the r'^{th} row and r^{th} column of the n^{th} block of matrix \mathcal{D} . For the procedure given, there are conditions placed upon the block matrix \mathcal{D} whereby its off-diagonal blocks, \mathcal{D}_2 and \mathcal{D}_3 , are symmetric and the diagonal blocks, \mathcal{D}_1 and \mathcal{D}_4 , are Hermitian. In the following, a matrix fulfilling these requirements will be written as

$$\mathcal{D}^{\text{req}} = \begin{pmatrix} A & B \\ B^* & A^* \end{pmatrix}.$$

Upon inspection of the Hamiltonian of the lattice system in question (2.9), it is not quite in the form where its corresponding matrix \mathcal{M} fulfils the above requirement, as there are no terms $\hat{a}_i \hat{a}_i^\dagger$ that have a prefactor of Ω_0 , which would fulfil the requirement of it being Hermitian. This is rectified using the bosonic commutation relations such that the first term of (2.9) may be rewritten as

$$\begin{aligned} 2\Omega_0 \sum_{i=1}^N \hat{a}_i^\dagger \hat{a}_i &\equiv \Omega_0 \sum_{i=1}^N \left(\hat{a}_i^\dagger \hat{a}_i + \hat{a}_i^\dagger \hat{a}_i \right) \\ &= \Omega_0 \sum_{i=1}^N \left(\hat{a}_i^\dagger \hat{a}_i + \hat{a}_i \hat{a}_i^\dagger - 1 \right) \\ &= -N\Omega_0 + \Omega_0 \sum_{i=1}^N \left(\hat{a}_i^\dagger \hat{a}_i + \hat{a}_i \hat{a}_i^\dagger \right). \end{aligned}$$

This allows the specific form of the matrix \mathcal{D}^{req} corresponding to the lattice

system Hamiltonian to be defined as

$$\mathcal{M} = \begin{pmatrix} \mathcal{M}_1 & \mathcal{M}_2 \\ \mathcal{M}_2^\dagger & \mathcal{M}_1^* \end{pmatrix},$$

where the blocks are given by

$$(\mathcal{M}_1)_{ij} = \frac{V_{ij}}{4} + \delta_{ij}\Omega_0 \quad \text{and} \quad (\mathcal{M}_2)_{ij} = \frac{V_{ij}}{4}.$$

The next step of the process groups together the creation and annihilation operators into a single vector, which is written as

$$\hat{\mathbf{a}}^\dagger = \left(\hat{a}_1^\dagger, \hat{a}_2^\dagger, \dots, \hat{a}_N^\dagger, \hat{a}_1, \hat{a}_2, \dots, \hat{a}_N \right),$$

such that the quadratic part of the Hamiltonian (2.9) is now written as

$$H_{\text{quad}} \equiv -N\Omega_0 + \hat{\mathbf{a}}^\dagger \mathcal{M} \hat{\mathbf{a}}. \quad (2.23)$$

The diagonalisation of this Hamiltonian is performed, using the terminology employed in [131], *para*-unitarily. Such a para-unitary diagonalisation is described by a transformation of the bosonic operator vectors, $\hat{\mathbf{a}}$ and $\hat{\mathbf{a}}^\dagger$, to new vectors $\hat{\gamma}$ and $\hat{\gamma}^\dagger$ of the form

$$\begin{aligned} \hat{\gamma} &= \mathcal{T} \hat{\mathbf{a}} \\ \hat{\gamma}^\dagger &= \hat{\mathbf{a}}^\dagger \mathcal{T}^\dagger, \end{aligned}$$

where $\hat{\gamma}^\dagger$ is of the same form as $\hat{\mathbf{a}}^\dagger$ (containing both creation and annihilation operators) with the entries the new operators $\hat{\gamma}^\dagger$ and $\hat{\gamma}$. The $2N$ square para-

unitary transformation matrix \mathcal{T} thus transforms H_{quad} into a diagonal form as

$$H'_{\text{quad}} = \hat{\mathbf{a}}^\dagger \mathcal{M} \hat{\mathbf{a}} = \hat{\mathbf{a}}^\dagger \mathcal{T}^\dagger (\mathcal{T}^\dagger)^{-1} \mathcal{M} \mathcal{T}^{-1} \mathcal{T} \hat{\mathbf{a}} = \hat{\boldsymbol{\gamma}}^\dagger \mathcal{E} \hat{\boldsymbol{\gamma}}$$

where \mathcal{E} is the diagonal matrix given by

$$(\mathcal{T}^\dagger)^{-1} \mathcal{M} \mathcal{T}^{-1} = \mathcal{E} \equiv \frac{1}{2} \text{diag}(\omega_1, \omega_2, \dots, \omega_N, \omega_1, \omega_2, \dots, \omega_N). \quad (2.24)$$

The special form of the diagonal eigenvalue matrix \mathcal{E} seen here, where the second N entries are a repeat of the first N , is reliant upon the specific block form of \mathcal{D}^{req} and the condition that \mathcal{T} is para-unitary. For a proof of this statement, the reader is referred to the original paper [131].

Aside: Para-Unitarity of \mathcal{T} Before going on to describe the algorithm proposed in [131], it is important that the main points of the para-unitary matrix are explained. As with a unitary transformation, a para-unitary transformation must conserve the commutation relations, which in the case of the vectors previously described, are written as

$$[\hat{\mathbf{a}}_r, \hat{\mathbf{a}}_r^\dagger] = \begin{cases} 1 & r \leq N \\ -1 & r \geq N. \end{cases}$$

Conservation of these bosonic operators through the transformation is ensured by a *para*-unitary matrix of which fulfils the condition

$$\mathcal{T} \tilde{\mathbb{I}} \mathcal{T}^\dagger = \tilde{\mathbb{I}},$$

where $\tilde{\mathbb{I}}$ is the para-identity matrix which has first N diagonal elements equal to 1 and second N diagonal elements equal to -1 . With the aid of this equation, it may also be shown that a para-unitary matrix

and its inverse are related as

$$\mathcal{T} = \begin{pmatrix} U & W \\ V & X \end{pmatrix} \quad \text{and} \quad \mathcal{T}^{-1} = \begin{pmatrix} U^\dagger & -V^\dagger \\ -W^\dagger & X^\dagger \end{pmatrix}, \quad (2.25)$$

which is used in the diagonalisation algorithm.

The following subsection details how the algorithm given in [131] may be applied to the lattice Hamiltonian, and the conditions under which it is valid. Said conditions rely on the matrix \mathcal{M} having the properties detailed in this section, with the procedure itself using other concepts also introduced here.

2.5.1 Exact Diagonalisation Algorithm

The algorithm for exact diagonalisation of the bosonic Hamiltonian (2.22) proposed in [131] relies on the matrix \mathcal{D}^{req} being positive-definite [132]. In general, a Hermitian matrix \mathcal{A} is positive definite if $\hat{v}^\dagger \mathcal{A} \hat{v}$ is real and positive for all non-zero complex vectors \hat{v} . In the specific case of the quadratic part of the lattice Hamiltonian (2.23), which is defined by the matrix \mathcal{M} containing all positive real entries, positive definiteness is ensured under the condition that the laser driving elicits a diagonally dominant matrix [133]. This condition places a less stringent condition on the strength of the laser driving than that of the strong driving regime considered in section 2.3, but does require that the diagonal (Rabi frequency elements) are larger than both the sum of the other elements in the same row and the sum of the other elements in the same column. The numerical verification of this condition comes in the first step of the procedure.

If and only if the matrix \mathcal{M} is positive-definite, it may be decomposed as $\mathcal{M} = \mathcal{K}^\dagger \mathcal{K}$, where the $2N$ square matrix \mathcal{K} is formed by a Cholesky decomposition [134] of \mathcal{M} . The matrix \mathcal{K} is a $2N$ square matrix which contains non-zero entries only in the leading diagonal and the entries above it, which is known as upper-triangular.

The next step is to unitarily diagonalise the matrix $\mathcal{K}\tilde{\mathbb{I}}\mathcal{K}^\dagger$ using a unitary matrix \mathcal{U} whose columns are arranged such that the first N diagonal elements of the resulting matrix \mathcal{L} are positive, and the second N negative. Assuming the as yet unknown matrix \mathcal{T} , which para-unitarily diagonalises \mathcal{M} , exists, the matrix \mathcal{U} may be defined as

$$\mathcal{U} = \mathcal{K}\mathcal{T}^{-1}\mathcal{E}^{-\frac{1}{2}}, \quad (2.26)$$

where the matrices $\mathcal{E}^{\pm\frac{1}{2}}$ are those with the entries of \mathcal{E} (2.24) to the power $\pm\frac{1}{2}$. This matrix may be proved to be unitary by the following calculation

$$\mathcal{U}^\dagger\mathcal{U} = \mathcal{E}^{-\frac{1}{2}}(\mathcal{T}^{-1})^\dagger\mathcal{K}^\dagger\mathcal{K}\mathcal{T}^{-1}\mathcal{E}^{-\frac{1}{2}} = \mathcal{E}^{-\frac{1}{2}}(\mathcal{T}^{-1})^\dagger\mathcal{M}\mathcal{T}^{-1}\mathcal{E}^{-\frac{1}{2}} = \mathcal{E}^{-\frac{1}{2}}\mathcal{E}\mathcal{E}^{-\frac{1}{2}} = \hat{\mathbb{I}},$$

where $\hat{\mathbb{I}}$ represents a $2N$ standard identity matrix. Using properties of the Hermitian conjugate found in [135], it may be shown that \mathcal{U} diagonalises the matrix $\mathcal{K}\tilde{\mathbb{I}}\mathcal{K}^\dagger$ according to the scheme

$$\begin{aligned} \mathcal{U}^\dagger \left[\mathcal{K}\tilde{\mathbb{I}}\mathcal{K}^\dagger \right] \mathcal{U} &\equiv \mathcal{U}^{-1}\mathcal{U}\mathcal{U}^\dagger \left[\mathcal{K}\tilde{\mathbb{I}}\mathcal{K}^\dagger \right] \mathcal{U}\mathcal{U}^\dagger (\mathcal{U}^\dagger)^{-1} = \mathcal{U}^{-1} \left[\mathcal{K}\tilde{\mathbb{I}}\mathcal{K}^\dagger \right] (\mathcal{U}^\dagger)^{-1} \\ &= \mathcal{E}^{\frac{1}{2}}\mathcal{T}\mathcal{K}^{-1} \left[\mathcal{K}\tilde{\mathbb{I}}\mathcal{K}^\dagger \right] (\mathcal{K}^\dagger)^{-1} \mathcal{T}^\dagger \mathcal{E}^{\frac{1}{2}} \\ &= \mathcal{E}^{\frac{1}{2}}\mathcal{T}\tilde{\mathbb{I}}\mathcal{T}^\dagger \mathcal{E}^{\frac{1}{2}} = \mathcal{E}^{\frac{1}{2}}\tilde{\mathbb{I}}\mathcal{E}^{\frac{1}{2}} = \mathcal{L}, \end{aligned}$$

where $(\mathcal{T}^\dagger)^{-1} = (\mathcal{T}^{-1})^\dagger$ has been used, and overall shows that the resulting diagonal matrix \mathcal{L} has the first N entries those of \mathcal{E} with the second N entries the negative of those of \mathcal{E} . The diagonal matrix \mathcal{E} resulting from the para-unitary diagonalisation of \mathcal{M} (2.24) is simply found as $\mathcal{E} = \tilde{\mathbb{I}}\mathcal{L}$.

Before providing a procedure for finding the form of the para-unitary matrix \mathcal{T} , it is important to show that it is indeed of this particular form. The para-unitarity of the matrix \mathcal{T} may be proved using the form of \mathcal{U} , which defines

$\mathcal{T}^{-1} = \mathcal{K}^{-1}\mathcal{U}\mathcal{E}^{\frac{1}{2}}$, as

$$(\mathcal{T}^{-1})^\dagger \tilde{\mathbb{I}}\mathcal{T}^{-1} = \mathcal{E}^{\frac{1}{2}}\mathcal{U}^\dagger (\mathcal{K}^\dagger)^{-1} \tilde{\mathbb{I}}\mathcal{K}^{-1}\mathcal{U}\mathcal{E}^{\frac{1}{2}} = \mathcal{E}^{\frac{1}{2}}\mathcal{U}^\dagger (\mathcal{K}^\dagger)^{-1} \tilde{\mathbb{I}}\mathcal{K}^{-1}\mathcal{U}\mathcal{E}^{\frac{1}{2}} = \mathcal{E}^{\frac{1}{2}}\mathcal{L}^{-1}\mathcal{E}^{\frac{1}{2}} = \tilde{\mathbb{I}},$$

where the fact that $\mathcal{K}\tilde{\mathbb{I}}\mathcal{K}^\dagger$ is Hermitian was used to find the form of \mathcal{L}^{-1} . Also using the form of \mathcal{T} found from \mathcal{U} , it may be shown that \mathcal{T}^{-1} diagonalises \mathcal{M} according to the scheme given in (2.24) as

$$(\mathcal{T}^\dagger)^{-1} \mathcal{M}\mathcal{T}^{-1} \equiv (\mathcal{T}^{-1})^\dagger \mathcal{M}\mathcal{T}^{-1} = \mathcal{E}^{\frac{1}{2}}\mathcal{U}^\dagger (\mathcal{K}^\dagger)^{-1} [\mathcal{K}^\dagger\mathcal{K}] \mathcal{K}^{-1}\mathcal{U}\mathcal{E}^{\frac{1}{2}} = \mathcal{E}.$$

So far, it has been shown that this scheme of para-unitary diagonalisation is possible. In what follows the meanings of the steps detailed above are considered.

The Cholesky decomposition of the matrix \mathcal{M} may be performed numerically, as may the subsequent unitary diagonalisation of the matrix $\mathcal{K}\tilde{\mathbb{I}}\mathcal{K}^\dagger$. At this point, it is likely that the eigenvectors which form the diagonalising matrix \mathcal{U} need re-ordering such that they form the matrix \mathcal{L} . The form of the unitary matrix \mathcal{U} (2.26) may now be used to find the columns of \mathcal{T}^{-1} using the equation $\mathcal{U}\mathcal{E}^{\frac{1}{2}} = \mathcal{K}\mathcal{T}^{-1}$. This procedure may be simplified using the specific form of the matrix \mathcal{T} , which will now be investigated. In order for the form of the linear transformation from operators \hat{a} to $\hat{\gamma}$ to be of the form $\hat{\gamma} = \mathcal{T}\hat{a}$, the matrix \mathcal{T} must transform the $\hat{\gamma}^\dagger$ creation operators such that their composition is the exact Hermitian conjugate of the annihilation operators $\hat{\gamma}$. In order for this to be the case, \mathcal{T} must have the block form,

$$\mathcal{T} = \begin{pmatrix} P & Q \\ Q^* & P^* \end{pmatrix}.$$

The inverse of a matrix with this block form may be formed simply using the

property of a para-unitary matrix given in (2.25), which yields

$$\mathcal{T}^{-1} = \begin{pmatrix} P^\dagger & -(Q^*)^\dagger \\ -Q^\dagger & (P^*)^\dagger \end{pmatrix}$$

and shows that that only the first N columns of \mathcal{T}^{-1} require calculation using $\mathcal{U}\mathcal{E}^{\frac{1}{2}} = \mathcal{K}\mathcal{T}^{-1}$, with the second N being found using the block form above.

The calculation of the para-unitary matrix detailed here thus completes the para-unitary diagonalisation of the quadratic part of the lattice Hamiltonian, which is now written as

$$H'_{\text{quad}} = -N\Omega_0 + \hat{\gamma}^\dagger \mathcal{E} \hat{\gamma},$$

and the focus now switches to removing the linear terms from the full Hamiltonian.

2.5.2 Removal of the Linear Terms

To obtain an exact diagonalisation of the system Hamiltonian (2.9), the linear terms must be accounted for. The procedure detailed in this section follows that originally proposed in [136], and will focus specifically on the lattice Hamiltonian. The linear part of the Hamiltonian must first be written in terms of the $\hat{\mathbf{a}}$ vectors containing both the creation and annihilation operators introduced in the previous section

$$H'_{\text{lin}} = -\frac{\Delta}{2} \sum_{i=1}^N (\hat{a}_i^\dagger + \hat{a}_i) - \frac{1}{2} \sum_{i \neq j} V_{ij} (\hat{a}_i^\dagger + \hat{a}_i) \equiv \vec{J} \hat{\mathbf{a}} + \hat{\mathbf{a}}^\dagger \vec{J}^\dagger,$$

where the elements of the row vector \vec{J} may be written as

$$\vec{J}_r = \begin{cases} -\frac{1}{4} \left(\Delta + \sum_{r' \neq r}^N V_{rr'} \right) & r \leq N \\ -\frac{1}{4} \left(\Delta + \sum_{r' \neq r-N}^N V_{(r-N)r'} \right) & N < r \leq 2N. \end{cases}$$

It should be noted here that the external factor of 1/4 is included as both the creation and annihilation operators appear in each of the vectors $\hat{\mathbf{a}}$ and $\hat{\mathbf{a}}^\dagger$.

Following such a re-writing of the linear part, the procedure detailed in the previous section which diagonalises the quadratic part of the Hamiltonian may be performed on all the terms. This performs the transformation

$$\begin{aligned} H' &= E_0 - N\Omega_0 + \hat{\mathbf{a}}^\dagger \mathcal{T}^\dagger (\mathcal{T}^\dagger)^{-1} \mathcal{M} \mathcal{T}^{-1} \mathcal{T} \hat{\mathbf{a}} + \vec{J} \mathcal{T}^{-1} \mathcal{T} \hat{\mathbf{a}} + \hat{\mathbf{a}}^\dagger \mathcal{T} (\mathcal{T}^\dagger)^{-1} \vec{J}^\dagger \\ &= E_0 - N\Omega_0 + \hat{\gamma}^\dagger \mathcal{E} \hat{\gamma} + \vec{J} \mathcal{T}^{-1} \hat{\gamma} + \hat{\gamma}^\dagger (\mathcal{T}^\dagger)^{-1} \vec{J}^\dagger, \end{aligned}$$

where, as before, $(\mathcal{T}^\dagger)^{-1} \mathcal{M} \mathcal{T}^{-1} = \mathcal{E}$. The next step is to make an element-wise shift of the $\hat{\gamma}$ vectors,

$$\hat{\gamma} = \hat{\beta} + \mathbf{t} \quad \text{and} \quad \hat{\gamma}^\dagger = \hat{\beta}^\dagger + \mathbf{t}^\dagger,$$

where the entries of \mathbf{t} are complex numbers, which may be inserted into the full Hamiltonian to yield

$$\begin{aligned} H' &= E_0 - N\Omega_0 + \hat{\beta}^\dagger \mathcal{E} \hat{\beta} + \hat{\beta}^\dagger \left(\mathcal{E} \mathbf{t} + (\mathcal{T}^\dagger)^{-1} \vec{J}^\dagger \right) \\ &\quad + \left(\vec{J} \mathcal{T}^{-1} + \mathbf{t}^\dagger \mathcal{E} \right) + \mathbf{t}^\dagger \mathcal{E} \mathbf{t} + \vec{J} \mathcal{T}^{-1} \mathbf{t} + \mathbf{t}^\dagger (\mathcal{T}^\dagger)^{-1} \vec{J}^\dagger, \end{aligned}$$

and leaves the bosonic commutation relations unaffected. The choice of the vector which shifts the bosonic operators may be made such that it removes the terms linear in the bosonic operators from the Hamiltonian. This cancellation requires

satisfying the condition

$$\mathcal{E}\mathbf{t} + (\mathcal{T}^\dagger)^{-1} = 0$$

and may be achieved by defining the elements as

$$\mathbf{t}_r = -\frac{\left[(\mathcal{T}^\dagger)^{-1} \vec{J}^\dagger\right]_r}{\mathcal{E}_{rr}} \quad \text{and} \quad \mathbf{t}_r^\dagger = -\frac{\left[\vec{J}\mathcal{T}^{-1}\right]_r}{\mathcal{E}_{rr}}.$$

With this definition made, the linear shift of the operators completely removes the linear terms from the full Hamiltonian, such that it may be written as

$$H' = E_0 - N\Omega_0 + \hat{\beta}^\dagger \mathcal{E} \hat{\beta} + \mathbf{t}^\dagger \mathcal{E} \mathbf{t} + \vec{J}\mathcal{T}^{-1}\mathbf{t} + \mathbf{t}^\dagger (\mathcal{T}^\dagger)^{-1} \vec{J}^\dagger. \quad (2.27)$$

The final step of the procedure is to put the Hamiltonian into fully diagonal form. The Hamiltonian where the linear terms have been removed (2.27) is in terms of vectors containing both the creation and annihilation operators, such that terms of the form $\hat{\beta}_i \hat{\beta}_i^\dagger$ are still present. Taking into account that the second N entries of the diagonal matrix \mathcal{E} are the same of the first N , an $N \times N$ matrix $\mathcal{E}_{\frac{1}{2}}$ whose diagonal entries are the first N entries of \mathcal{E} is defined. This allows the diagonal part of the Hamiltonian to be put into conventional form as

$$\begin{aligned} \hat{\beta}^\dagger \mathcal{E} \hat{\beta} &\equiv \sum_{j=1}^N \left[\left(\mathcal{E}_{\frac{1}{2}}\right)_{jj} \hat{\beta}_j^\dagger \hat{\beta}_j + \left(\mathcal{E}_{\frac{1}{2}}\right)_{jj} \hat{\beta}_j \hat{\beta}_j^\dagger \right] \\ &= \sum_{j=1}^N \left[\left(\mathcal{E}_{\frac{1}{2}}\right)_{jj} \hat{\beta}_j^\dagger \hat{\beta}_j + \left(\mathcal{E}_{\frac{1}{2}}\right)_{jj} \left(1 + \hat{\beta}_j^\dagger \hat{\beta}_j\right) \right] \\ &= \sum_{j=1}^N \left(\mathcal{E}_{\frac{1}{2}}\right)_{jj} + 2 \sum_{j=1}^N \left(\mathcal{E}_{\frac{1}{2}}\right)_{jj} \hat{\beta}_j^\dagger \hat{\beta}_j, \end{aligned}$$

where the commutation relations have been used to put the relevant operators into normal order. The final expression for the exactly diagonalised Hamiltonian

may be written as

$$H' = E_0 - N\Omega_0 + \mathbf{t}^\dagger \mathcal{E} \mathbf{t} + \vec{J} \mathcal{T}^{-1} \mathbf{t} + \mathbf{t}^\dagger (\mathcal{T}^\dagger)^{-1} \vec{J}^\dagger + \sum_{j=1}^N \left(\mathcal{E}_{\frac{1}{2}} \right)_{jj} + 2 \sum_{j=1}^N \left(\mathcal{E}_{\frac{1}{2}} \right)_{jj} \hat{\beta}_j^\dagger \hat{\beta}_j$$

and may be used as a measure of the accuracy of the diagonalisation used in the strong driving regime.

2.5.3 Validity of the Strong Driving Solutions

In this final section concerning the exact diagonalisation of the lattice Hamiltonian, the state energies found in the strong laser driving regime will be compared with those found from the exact diagonalisation. A comparison of the energies found using the two approaches for an $L_{\text{sq}} = 10$ square lattice with $\Delta = 0$ may be seen in Fig. 2.14. In this figure the energy offset E_0 has been neglected in both cases, which sets the zero excitation state to have energy zero and allows the manifold separation of approximately $2\Omega_0$ predicted in the strong driving regime to be seen. Qualitatively, this figure shows that the two spectra converge as the ratio Ω_0/V^{nn} increases, which is to be expected. For the smallest laser driving, shown in Fig. 2.14(a), the whole of the strong laser driving regime spectrum is shifted up in energy from that of the exact diagonalisation calculation by approximately $3\Omega_0$. Of course, the strong laser driving calculation is not expected to deal with a situation where the laser driving and atomic interactions are of the same order, therefore such a difference is expected. Close inspection also shows that the internal structure of the manifold is different in the two cases. Increasing the ratio of Ω_0/V^{nn} , as seen in Fig. 2.14(b) and (c) shows that this overall offset reduces as the strong laser driving regime becomes more valid. What these two figures also show is that the internal structures of the manifolds are almost identical once $\Omega_0/V^{\text{nn}} = 100$. A final remark on this figure is that, as described in

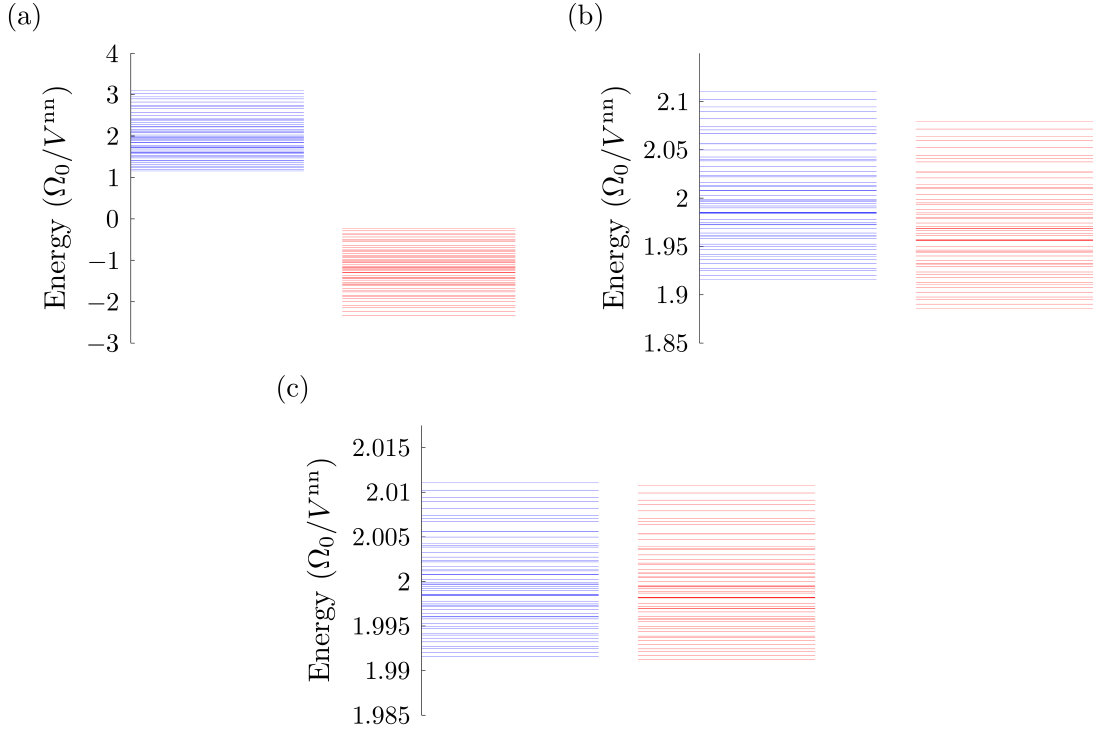


Figure 2.14: Figure showing how spectra of the singly excited manifold compare for the strong laser driving regime (blue/left) and exact diagonalisation (red/right) for an $L_{\text{sq}} = 10$ square lattice. The three values of the laser driving are: (a) $\Omega_0/V^{\text{nn}} = 1$, (b) $\Omega_0/V^{\text{nn}} = 10$ and (c) $\Omega_0/V^{\text{nn}} = 100$.

section 2.3.2, when the strong laser driving regime is valid both spectra suggest quasi-degenerate manifolds separated by approximately $2\Omega_0$ (as $E_0=0$ here).

In order to quantify the difference in the spectra given by the strong driving regime and the exact diagonalisation scheme, the average percentage error of the states in the single excitation manifold is calculated. The percentage error for each state of the manifold is carried out as $(E_{1_k}^{\text{ED}} - E_{1_k}^{\text{SD}}) / E_{1_k}^{\text{ED}} \times 100$ where ED and SD refer to the exact diagonalisation and strong driving regimes respectively. The resulting averages for various lattice sizes and laser driving strengths are given in table 2.1, and clearly show a trend of increasing inaccuracy as the lattice size increases. The values given in the table show that the laser driving $\Omega_0/V^{\text{nn}} > 10$ in order for the strong driving regime calculation to be within 10% of the exact diagonalisation regime for the lattice sizes considered here. Also, as is to be

		L				
		5	10	15	20	25
$\frac{\Omega_0}{V^{\text{nn}}}$	5	1.38	6.12	15.36	31.6	60.97
	10	0.34	1.47	3.45	6.4	10.47
	25	0.054	0.23	0.549	0.975	1.546
	50	0.014	0.058	0.134	0.243	0.383
	100	0.0034	0.0145	0.0336	0.0606	0.0955

Table 2.1: Average percentage error of the strong laser driving single excitation state energies for $\Delta = 0$ and different values Ω_0/V^{nn} and lattice sizes $L = \sqrt{N}$.

expected, the strong laser driving regime becomes more accurate as the laser driving becomes more dominant. The trend that the strong driving regime is less accurate the larger the lattice size is also to be expected, as the sources of error come from terms depending on the atomic interactions and laser detuning. As in the results presented here the laser detuning Δ is set to zero, the error comes purely from the atomic interactions, which are obviously greater for larger lattices.

This section has detailed the numerical method which may be applied to exactly diagonalise the lattice Hamiltonian (2.9), with a comparison of the results from the two different methods provided. The low level of the errors given in table 2.1 justify confidence in the results detailed in the previous sections, which are based on the strong laser driving calculation. Having shown this, the following section details how to create quantum states of light using the collective excitation states described in section 2.4.

2.6 Single Photon Sources

This section details how to create quantum states of light from the collective excitation states which are thoroughly analysed in section 2.4. The description given here is based on the schemes developed in [91] and explained for a one-

dimensional Rydberg lattice in [93]. As the reader will discover, the states of light generated are essentially mapped directly from the quantum collective excitation state of the atoms in the lattice, therefore being quantum in nature themselves.

2.6.1 Mapping to a Stable State

The limited lifetime of the Rydberg atoms places time constraints on any further manipulation of the collective state, which will be an issue for an experimental setup. Therefore the collective excitations are mapped onto superpositions of the two stable states $|g\rangle$ and $|s\rangle$ used previously in section 2.4 in order for the atom to photon mapping to be applied. This process is explained here.

Recalling that, as explained in section 2.3.1, the single site bosonic states $|0\rangle_i$ and $|1\rangle_i = \hat{a}_i^\dagger |0\rangle_i$ are equivalent to the single atom states $|-\rangle_i$ and $|+\rangle_i$ respectively, using two laser pulses it is possible to perform the following mapping. Inversion of the laser pulses given in the introductory part of section 2.4, such that the π -pulse of the laser with Rabi frequency Ω_{rs} is applied first followed by the $\pi/2$ -pulse of the laser with Rabi frequency Ω_{gs} , performs the sequences

$$\begin{aligned} |0\rangle_i \equiv |-\rangle_i &= \frac{1}{\sqrt{2}} \{|g\rangle_i - |r\rangle_i\} \xrightarrow{\tau_2} \frac{1}{\sqrt{2}} \{|g\rangle_i - i|s\rangle_i\} \xrightarrow{\tau_1} |g\rangle_i \\ |1\rangle_i \equiv |+\rangle_i &= \frac{1}{\sqrt{2}} \{|g\rangle_i + |r\rangle_i\} \xrightarrow{\tau_2} \frac{1}{\sqrt{2}} \{|g\rangle_i + i|s\rangle_i\} \xrightarrow{\tau_1} i|s\rangle_i, \end{aligned}$$

such that the bosonic state $|0\rangle_i$ is mapped onto the atomic state $|g\rangle_i$ and $|1\rangle_i$ is mapped onto $i|s\rangle_i$. This sequence of laser pulses maps the bosonic excitations onto the two atomic hyperfine ground states, and therefore may be used to store the single and double collective bosonic excitations studied in the previous sections. In terms of the many-body atomic states, the single excitation state given

in (2.16) may be written as

$$\left| \Psi_k^{(1)} \right\rangle = \sum_{l=1}^N U_{lk} \sigma_{sg}^{(l)} |\text{init}\rangle, \quad (2.28)$$

with the double excitation state (2.17) similarly expressed as

$$\left| \Psi_{ij}^{(2)} \right\rangle = \sum_{l,m=1}^N U_{li} U_{mj} \sigma_{sg}^{(l)} \sigma_{sg}^{(m)} |\text{init}\rangle,$$

where the operator $\sigma_{sg}^{(k)} = |s\rangle_k \langle g|$.

2.6.2 The Atom-Light Hamiltonian

The storage of the collective excitation in a stable configuration using two hyperfine ground states, $|g\rangle_i$ and $|s\rangle_i$, is detailed in section 2.6.1. In order to produce quantum states of light from such atomic states, a third level of the atom is required, $|a\rangle_i$, which, as illustrated in Fig. 2.15, forms a lambda scheme with the

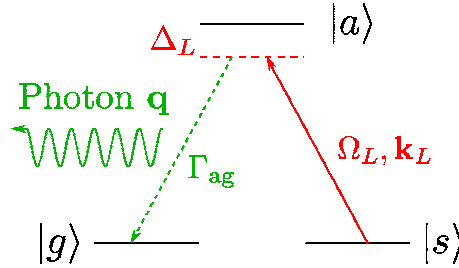


Figure 2.15: Scheme for the mapping from a collective excitation state to the photonic state. A laser with Rabi frequency Ω_L couples the states $|s\rangle$ and $|a\rangle$ off resonantly. The photon is then released on the decay of the atomic level $|a\rangle$ to $|g\rangle$.

two ground states. The state in which the collective excitation is stored, $|s\rangle_i$, is coupled off resonantly to the auxiliary state $|a\rangle_i$ by the application of a classical laser field with Rabi frequency Ω_L , detuning Δ_L and momentum \mathbf{k}_L . By careful choice of the atomic levels used, the decay of the state $|a\rangle_i$ back to $|s\rangle_i$ may be neglected, such that photons with momentum \mathbf{q} are emitted into the electro-

magnetic field when the state $|a\rangle_i$ decays to the atomic ground state $|g\rangle_i$. A level scheme of this nature is described in [91], which uses a cycling transition provided by the rubidium 87 D_2 line [137]. The basic idea of this scheme uses states where a two-photon transition is required to take the atom from $|s\rangle$ to $|a\rangle$, such that a single photon decay of the state $|a\rangle$ back to $|s\rangle$ is forbidden. However, the decay of the atom from $|a\rangle$ to $|g\rangle$ is dipole allowed and thus photons may be emitted on this transition. In ^{87}Rb , suggested levels are $|s\rangle = |5^2S_{1/2}, F = 1, m_F = 1\rangle$, $|g\rangle = |5^2S_{1/2}, F = 2, m_F = 2\rangle$ and $|a\rangle = |5^2P_{3/2}, F = 3, m_F = 3\rangle$, where F represents the total angular momentum of the atom and m_F is the total angular momentum projection along z , which will allow the experimental procedures detailed in [91] to be implemented.

For a single atom, the Hamiltonian of this system may be written as

$$\begin{aligned}
H = & \omega_s |s\rangle \langle s| + \omega_a |a\rangle \langle a| + \omega_g |g\rangle \langle g| + \sum_{\mathbf{q}\lambda} \omega_{\mathbf{q}\lambda} \hat{a}_{\mathbf{q}\lambda}^\dagger \hat{a}_{\mathbf{q}\lambda} \\
& + \Omega_L [e^{-i(\mathbf{k}_L \cdot \mathbf{r} - \omega_L t)} |s\rangle \langle a| + e^{i(\mathbf{k}_L \cdot \mathbf{r} - \omega_L t)} |a\rangle \langle s|] \\
& + (\Omega_{\text{em}} + \Omega_{\text{em}}^*) (|g\rangle \langle a| + |a\rangle \langle g|), \tag{2.29}
\end{aligned}$$

where the first three terms are the energies of the states $|s\rangle$, $|a\rangle$ and $|g\rangle$ respectively. The operators $\hat{a}_{\mathbf{q}\lambda}^\dagger$ ($\hat{a}_{\mathbf{q}\lambda}$) are the creation (annihilation) operators of the \mathbf{q}^{th} mode of the photonic field with energy $\omega_{\mathbf{q}\lambda}$ and unit polarization vector $\hat{\mathbf{e}}_{\mathbf{q}\lambda}$, ($\mathbf{q} \cdot \hat{\mathbf{e}}_{\mathbf{q}\lambda} = 0$), such that the fourth term describes the energy of the photons in the electromagnetic field. The photonic operators follow the usual bosonic commutation relations, expressed as

$$[\hat{a}_{\mathbf{q}\lambda}, \hat{a}_{\mathbf{q}'\lambda'}^\dagger] = \delta_{\mathbf{q},\mathbf{q}'} \delta_{\lambda,\lambda'}.$$

The term on the second line describes the interaction of a two level atom with

a linearly polarised classical laser field of Rabi frequency $\Omega_L = \mathcal{E}_L d_{as}/2$ in the rotating wave approximation, as derived in appendix B. The final term describes the interaction of the atom with a quantized electromagnetic field, with effective Rabi frequency to the mode $\omega_{\mathbf{q}\lambda}$ given by

$$\Omega_{\text{em}} = \sum_{\mathbf{q}\lambda} \sqrt{\frac{\omega_{\mathbf{q}\lambda}}{2\epsilon_0 V}} \mathbf{d}_{ga} \cdot \mathbf{e}_{\mathbf{q}\lambda} e^{i\mathbf{q}\cdot\mathbf{r}} \hat{a}_{\mathbf{q}\lambda},$$

calculated from the quantized electric field derived in [129]. This expression contains the normalisation volume V , the vacuum permittivity ϵ_0 and the dipole matrix element of the $|g\rangle \rightarrow |a\rangle$ transition, \mathbf{d}_{ga} .

The mapping to the photonic state takes place when the atoms undergo the transition $|a\rangle \rightarrow |s\rangle$ with the emission of a photon. This process may be described under a particular parameter regime, which is detailed here. The first step is the application of a unitary transformation which reduces the energy of the auxiliary state $|a\rangle$ by an amount ω_L . This unitary transformation is written as

$$U_a = e^{i\omega_L t} |a\rangle \langle a| + |s\rangle \langle s| + |g\rangle \langle g|$$

and, as explained in appendix C, may be used to find an effective Hamiltonian H' for the system

$$H' = U_a H U_a^\dagger - i U_a \partial_t U_a^\dagger.$$

Application of this transformation to the initial Hamiltonian (2.29) yields the transformed Hamiltonian

$$\begin{aligned} H' = & (\omega_a - \omega_L) |a\rangle \langle a| + \omega_s |s\rangle \langle s| + \omega_g |g\rangle \langle g| + \Omega_L (e^{-i\mathbf{k}_L \cdot \mathbf{r}} |s\rangle \langle a| + e^{i\mathbf{k}_L \cdot \mathbf{r}} |a\rangle \langle s|) \\ & + (\Omega_{\text{em}} + \Omega_{\text{em}}^*) (e^{i\omega_L t} |a\rangle \langle g| + e^{-i\omega_L t} |g\rangle \langle a|) + \sum_{\mathbf{q}\lambda} \omega_{\mathbf{q}\lambda} \hat{a}_{\mathbf{q}\lambda}^\dagger \hat{a}_{\mathbf{q}\lambda}, \end{aligned} \quad (2.30)$$

which clearly shows the reduction in energy of the auxiliary state. The assump-

tion is subsequently made that $|\Delta_L| \gg \Omega_L$, where $\Delta_L = \omega_a - \omega_L$ is the detuning of the laser frequency from the atomic transition frequency. Under this condition, it may be assumed that the population of atoms in the auxiliary state is a constant, allowing it to be adiabatically eliminated [127]. This process is detailed in appendix D, where it can be seen to induce small shifts of the energies of the two ground states (Hamiltonian (D.1)). Neglecting these small energy shifts, which amounts to the approximation that the detuning is much greater than the Rabi frequencies, the Hamiltonian may be approximated as

$$H' \approx \omega_s |s\rangle \langle s| + \omega_g |g\rangle \langle g| + \sum_{\mathbf{q}\lambda} \omega_{\mathbf{q}\lambda} \hat{a}_{\mathbf{q}\lambda}^\dagger \hat{a}_{\mathbf{q}\lambda} - \frac{\Omega_L (\Omega_{\text{em}} + \Omega_{\text{em}}^*)}{\Delta_L} (e^{-i(\mathbf{k}_L \cdot \mathbf{r} - \omega_L t)} |s\rangle \langle g| + e^{i(\mathbf{k}_L \cdot \mathbf{r} - \omega_L t)} |g\rangle \langle s|). \quad (2.31)$$

where the auxiliary level has been removed.

The next step in the simplification of this Hamiltonian is a second unitary transformation, which increases the energy of the state $|s\rangle$ by energy ω_L . The unitary transformation which performs this increase in energy of $|s\rangle$ may be written as

$$U_s = e^{-i\omega_L t} |s\rangle \langle s| + |g\rangle \langle g|,$$

such that following the procedure for application of the transformation as in appendix C, the Hamiltonian reads

$$H'' = \omega_L |s\rangle \langle s| + \sum_{\mathbf{q}\lambda} \omega_{\mathbf{q}\lambda} \hat{a}_{\mathbf{q}\lambda}^\dagger \hat{a}_{\mathbf{q}\lambda} - \frac{\Omega_L (\Omega_{\text{em}} + \Omega_{\text{em}}^*)}{\Delta_L} (e^{-i\mathbf{k}_L \cdot \mathbf{r}} |s\rangle \langle g| + e^{i\mathbf{k}_L \cdot \mathbf{r}} |g\rangle \langle s|)$$

where the bare energies of both the hyperfine ground states $|g\rangle$ and $|s\rangle$, ω_g and ω_s respectively, have been set to zero.

To this point, the Hamiltonian has only described a single atom at position \mathbf{r} interacting with a laser. Extending to the case of multiple atoms, each at position

\mathbf{r}_α , the atomic transition operator may be written as

$$\hat{\sigma}_\alpha = |g\rangle_\alpha \langle s|,$$

which may be shown to have the following commutation relations

$$\begin{aligned} [\hat{\sigma}_\alpha, \hat{\sigma}_\beta^\dagger] &= 0 \quad \text{if } \alpha \neq \beta \\ \{\hat{\sigma}_\alpha, \hat{\sigma}_\alpha^\dagger\} &= 1, \end{aligned}$$

such that they obey neither bosonic or fermionic algebra. These operators may be inserted into the Hamiltonian, which is extended to an N atom system to yield

$$H'' = \sum_{\alpha=1}^N \omega_L \hat{\sigma}_\alpha^\dagger \hat{\sigma}_\alpha + \sum_{\mathbf{q}\lambda} \omega_{\mathbf{q}\lambda} \hat{a}_{\mathbf{q}\lambda}^\dagger \hat{a}_{\mathbf{q}\lambda} - \frac{\Omega_L (\Omega_{\text{em}} + \Omega_{\text{em}}^*)}{\Delta_L} \sum_{\alpha=1}^N (e^{-i\mathbf{k}_L \cdot \mathbf{r}_\alpha} \hat{\sigma}_\alpha^\dagger + e^{i\mathbf{k}_L \cdot \mathbf{r}_\alpha} \hat{\sigma}_\alpha).$$

Close inspection of this Hamiltonian reveals terms that do not conserve energy, such as those where an atom becomes excited whilst emitting a photon and vice versa, $\hat{\sigma}_\alpha^\dagger \hat{a}_{\mathbf{q}\lambda}^\dagger$ and $\hat{\sigma}_\alpha \hat{a}_{\mathbf{q}\lambda}$ respectively. Upon insertion of time evolution of the free field and free atom operators [47], these terms may be neglected in the rotating wave approximation under the assumption that the laser detuning is small. Under this condition, removal of these terms from the Hamiltonian leaves it written in the beamsplitter form seen in [92],

$$\begin{aligned} H_{\text{BS}} &= \sum_{\alpha=1}^N \omega_L \hat{\sigma}_\alpha^\dagger \hat{\sigma}_\alpha + \sum_{\mathbf{q}\lambda} \omega_{\mathbf{q}\lambda} \hat{a}_{\mathbf{q}\lambda}^\dagger \hat{a}_{\mathbf{q}\lambda} \\ &\quad - \sum_{\alpha=1}^N \sum_{\mathbf{q}\lambda} \left(K_{\mathbf{q}\lambda} e^{i(\mathbf{q}-\mathbf{k}_L) \cdot \mathbf{r}_\alpha} \hat{a}_{\mathbf{q}\lambda} \hat{\sigma}_\alpha^\dagger + K_{\mathbf{q}\lambda}^* e^{-i(\mathbf{q}-\mathbf{k}_L) \cdot \mathbf{r}_\alpha} \hat{a}_{\mathbf{q}\lambda}^\dagger \hat{\sigma}_\alpha \right), \end{aligned} \quad (2.32)$$

where

$$K_{\mathbf{q}\lambda} = \left(\frac{\Omega_L}{\Delta_L} \right) \sqrt{\frac{\omega_{\mathbf{q}\lambda}}{2\epsilon_0 V}} \mathbf{d}_{\text{ga}} \cdot \mathbf{e}_{\mathbf{q}\lambda},$$

which, as explained in [91, 93], is essential for the atom photon mapping to be calculated. This is referred to as a beam-splitter Hamiltonian as the atom-light interaction (final) term describes the annihilation of an atomic excitation resulting in the creation of a photonic excitation or vice-versa [48].

This section has detailed the steps and approximations made to form a beam-splitter Hamiltonian, which describes the interaction of a three level system with both a quantised and a classical field.

2.6.3 The Atom-Photon Mapping

This section provides an explanation of how the atom photon mapping comes about and the approximations required for it to be valid. As in [126], the reader is directed to the original work for the mathematical details of the derivation of the operator determining the photonic modes into which light is emitted, [91, 92]. The details provided here will give the reader sufficient knowledge to interpret the results of when the mapping is applied to the two dimensional lattice systems considered in this work.

The state of the system before the atom-photon mapping is applied may be written as

$$|\psi(0)\rangle = |\Psi\rangle_{\text{at}} |0\rangle_{\text{ph}},$$

where $|0\rangle_{\text{ph}}$ is the photon vacuum and the initial atomic state may be written as

$$|\Psi\rangle_{\text{at}} = \sum_{n_1, \dots, n_N} \Psi_{n_1, \dots, n_N} \hat{\sigma}_{n_1}^\dagger \dots \hat{\sigma}_{n_N}^\dagger |0\rangle_{\text{at}},$$

where $|0\rangle_{\text{at}}$ is the state where all atoms are in the ground state, $|0\rangle_{\text{at}} = \prod_i |g\rangle_i$, and the coefficient Ψ_{n_α} is the coefficient of the atomic operator $\hat{\sigma}_{n_\alpha}^\dagger$, which performs the transition $|g\rangle_{n_\alpha} \rightarrow |s\rangle_{n_\alpha}$. These coefficients therefore define the initial collective excitation state of the system. As detailed in the previous section, the classical

laser with Rabi frequency Ω_L will transfer such an atomic state into a photonic state after a period of time much greater than the lifetime of the auxiliary state. The aim is thus to find an expression for the photonic state $|\Phi\rangle_{\text{ph}}$ after the atomic state has decayed

$$|\psi(t)\rangle = U_{\text{ph}}(t) |\psi(0)\rangle = |0\rangle_{\text{at}} |\Phi\rangle_{\text{ph}},$$

where $U_{\text{ph}}(t) = e^{-iH_{\text{BS}}t}$ is the time-evolution operator, with H_{BS} as given in (2.32). Using the fact that this operator is unitary ($U_{\text{ph}}^\dagger U_{\text{ph}} = \mathbb{I}$) and that it does not affect the vacuum state ($U_{\text{ph}}(t) |\text{vac}\rangle = |\text{vac}\rangle$), which is that void of both atomic and photonic excitations, $|\text{vac}\rangle = |0\rangle_{\text{ph}} |0\rangle_{\text{ph}}$, the state of the system at time t may be written explicitly as

$$\begin{aligned} |\psi(t)\rangle &= U_{\text{ph}}(t) |\psi(0)\rangle \\ &= \sum_{n_1, \dots, n_N} \Psi_{n_1, \dots, n_N} \left(U_{\text{ph}}(t) \hat{\sigma}_{n_1} U_{\text{ph}}^\dagger(t) \right) \dots \left(U_{\text{ph}}(t) \hat{\sigma}_{n_N} U_{\text{ph}}^\dagger(t) \right) |\text{vac}\rangle. \end{aligned} \quad (2.33)$$

The explicit expression for the state at time t (2.33) shows that it is defined by the form of the transformed atomic operators, which may be written as

$$U_{\text{ph}}(t) \hat{\sigma}_\alpha U_{\text{ph}}^\dagger(t) \equiv \sum_{\mathbf{q}\lambda} g_{\alpha\mathbf{q}\lambda}(t) \hat{a}_{\mathbf{q}\lambda}^\dagger + \sum_{\beta} h_{\alpha\beta}(t) \hat{\sigma}_\beta^\dagger,$$

where $g_{\alpha\mathbf{q}\lambda}(t)$ and $h_{\alpha\beta}(t)$ are the coefficients of the photonic and atomic parts, respectively. These coefficients are found by multiplying the expression from the left by $\hat{a}_{\mathbf{q}\lambda}$ and $\hat{\sigma}_\beta$ respectively and taking the vacuum expectation value, which yields

$$\begin{aligned} \langle \text{vac} | \underbrace{\hat{a}_{\mathbf{q}\lambda} U_{\text{ph}}(t)}_{=\hat{a}_{\mathbf{q}\lambda}(t)} \hat{\sigma}_\alpha^\dagger \underbrace{U_{\text{ph}}^\dagger(t)}_{=|\text{vac}\rangle} | \text{vac} \rangle &= \sum_{\mathbf{q}'\lambda'} g_{\alpha\mathbf{q}'\lambda'}(t) \langle \text{vac} | \hat{a}_{\mathbf{q}\lambda}(t) \hat{a}_{\mathbf{q}'\lambda'}^\dagger | \text{vac} \rangle \\ &+ \sum_{\beta} h_{\alpha\beta}(t) \langle \text{vac} | \hat{a}_{\mathbf{q}\lambda} \hat{\sigma}_\beta^\dagger | \text{vac} \rangle = g_{\alpha\mathbf{q}\lambda}(t) \end{aligned}$$

and

$$\begin{aligned} \left\langle \text{vac} \left| \underbrace{\hat{\sigma}_\beta U_{\text{ph}}(t)}_{=\hat{\sigma}_\beta(t)} \underbrace{\hat{\sigma}_\alpha^\dagger U_{\text{ph}}^\dagger(t)}_{=|\text{vac}\rangle} \right| \text{vac} \right\rangle &= \sum_{\mathbf{q}\lambda} g_{\alpha\mathbf{q}\lambda}(t) \left\langle \text{vac} \left| \hat{\sigma}_\beta(t) \hat{a}_{\mathbf{q}\lambda}^\dagger \right| \text{vac} \right\rangle \\ &+ \sum_{\gamma} h_{\alpha\gamma}(t) \left\langle \text{vac} \left| \hat{\sigma}_\beta \hat{\sigma}_\gamma^\dagger \right| \text{vac} \right\rangle = h_{\alpha\beta}(t), \end{aligned}$$

where the fact that states of differing excitation number are orthogonal has also been used. For times much greater than the atomic decay time, $t \gg \tau = 1/\Gamma_{\text{ag}}$ (where Γ_{ag} is the decay rate of the atom from $|a\rangle$ to $|g\rangle$) the state will be purely photonic and therefore the atomic coefficient $h_{\alpha\beta}(t \gg \tau) = 0$. The atom-photon mapping may therefore, in the limit of long times, be expressed as the unitary transformation

$$U_{\text{ph}}(t) \hat{\sigma}_\alpha^\dagger U_{\text{ph}}^\dagger(t) \stackrel{t \gg \tau}{\cong} \sum_{\mathbf{q}\lambda} g_{\alpha\mathbf{q}\lambda}(t) \hat{a}_{\mathbf{q}\lambda}^\dagger,$$

such that the resulting state relies on the coefficients

$$g_{\alpha\mathbf{q}\lambda}(t) = \left\langle \text{vac} \left| \hat{a}_{\mathbf{q}\lambda}(t) \hat{\sigma}_\alpha^\dagger \right| \text{vac} \right\rangle, \quad (2.34)$$

which in turn depend on the time evolution of the photonic annihilation operator.

The first step to find the time dependency of the photonic annihilation operator is to find its equation of motion in the Heisenberg picture, the starting point of which is [92]

$$\dot{\hat{a}}_{\mathbf{q}\lambda}(t) = i [H_{\text{BS}}(t), \hat{a}_{\mathbf{q}\lambda}(t)],$$

as the annihilation operator has no explicit time dependence. Calculation of this

result may be written as

$$\begin{aligned}
i [H_{\text{BS}}, \hat{a}_{\mathbf{q}\lambda}] &= i \left[\sum_{\alpha=1}^N \omega_L \underbrace{[\hat{\sigma}_\alpha^\dagger \hat{\sigma}_\alpha, \hat{a}_{\mathbf{q}\lambda}]}_{=0} + \sum_{\mathbf{q}'\lambda'} \omega_{\mathbf{q}'\lambda'} \underbrace{[\hat{a}_{\mathbf{q}'\lambda'}^\dagger \hat{a}_{\mathbf{q}'\lambda'}, \hat{a}_{\mathbf{q}\lambda}]}_{=-\hat{a}_{\mathbf{q}'\lambda'} \delta_{\mathbf{q},\mathbf{q}'} \delta_{\lambda,\lambda'}} \right] \\
&\quad - \sum_{\alpha=1}^N \sum_{\mathbf{q}'\lambda'} \left(K_{\mathbf{q}'\lambda} e^{i(\mathbf{q}'-\mathbf{k}_L)\cdot\mathbf{r}_\alpha} \underbrace{[\hat{a}_{\mathbf{q}'\lambda'}^\dagger \hat{\sigma}_\alpha^\dagger, \hat{a}_{\mathbf{q}\lambda}]}_{=0} \right. \\
&\quad \left. + K_{\mathbf{q}'\lambda}^* e^{-i(\mathbf{q}'-\mathbf{k}_L)\cdot\mathbf{r}_\alpha} \underbrace{[\hat{a}_{\mathbf{q}'\lambda'}^\dagger \hat{\sigma}_\alpha, \hat{a}_{\mathbf{q}\lambda}]}_{=-\hat{\sigma}_\alpha \delta_{\mathbf{q},\mathbf{q}'} \delta_{\lambda,\lambda'}} \right) \Big] \\
\dot{\hat{a}}_{\mathbf{q}\lambda}(t) &= -i\omega_{\mathbf{q}} \hat{a}_{\mathbf{q}\lambda}(t) + i \sum_{\beta} K_{\mathbf{q}\lambda}^* e^{-i(\mathbf{q}-\mathbf{k}_L)\cdot\mathbf{r}_\beta} \hat{\sigma}_\beta(t), \tag{2.35}
\end{aligned}$$

where in the second step the position index has been changed to β such that there are no duplicate indices when the expression is later substituted into that for the $g_{\alpha\mathbf{q}\lambda}$ coefficients, (2.34). The choice was also made in the first step to neglect the notation showing that the operators are functions of time, for aesthetic reasons, though they are re-inserted in the final step. Solution of this differential equation yields

$$\hat{a}_{\mathbf{q}\lambda}(t) = e^{-i\omega_{\mathbf{q}}t} \hat{a}_{\mathbf{q}\lambda}(0) + iK_{\mathbf{q}\lambda}^* \sum_{\beta} e^{-i(\mathbf{q}-\mathbf{k}_L)\cdot\mathbf{r}_\beta} \int_0^t d\tau e^{-i\omega_{\mathbf{q}}\lambda(t-\tau)} \hat{\sigma}_\beta(\tau),$$

which may be substituted into the expression for the photon state coefficients (2.34) to yield

$$g_{\alpha\mathbf{q}\lambda}(t) = iK_{\mathbf{q}\lambda}^* \sum_{\beta} e^{-i(\mathbf{q}-\mathbf{k}_L)\cdot\mathbf{r}_\beta} \int_0^t d\tau e^{-i\omega_{\mathbf{q}}\lambda(t-\tau)} \langle \text{vac} | \hat{\sigma}_\beta(\tau) \hat{\sigma}_\alpha^\dagger | \text{vac} \rangle. \tag{2.36}$$

Therefore, the coefficients describing the generation of the photonic state from the collective excitation have a dependence on the time evolution of the atomic annihilation operator.

Atomic Operator Evolution in the Low Excitation Limit

This section outlines how the time evolution of the atomic operators may be derived in the low excitation number limit in which the initial system will be. Such a derivation is provided in [91, 93], which also give details of the full derivation which is not in this limit [92, 138].

As discussed thoroughly in section 2.4, the excitation regime detailed here is reliable only for those states where the number of excitations in the system is low. Using the matrix form of the atomic transition operators, the commutation relations may be shown to be

$$\left[\hat{\sigma}_\alpha, \hat{\sigma}_\beta^\dagger \right] = \delta_{\alpha,\beta} \hat{\sigma}_z \equiv -\delta_{\alpha,\beta} \left(\hat{\mathbb{I}} - 2\hat{n}_\alpha^{(s)} \right),$$

where $\hat{n}_\alpha^{(s)}$ is the number of atoms in the state $|s\rangle$ at site α . Now, under the approximation that the system is limited to the subspace where the excitation number is much lower than the number of sites of the lattice, the expectation value $\langle \hat{n}_\alpha^{(s)} \rangle \ll 1$. The commutation relations may therefore be approximated as those of bosons

$$\left[\hat{\sigma}_\alpha, \hat{\sigma}_\beta^\dagger \right] \approx \delta_{\alpha,\beta},$$

such that the atomic transition operators may be replaced by bosonic operators

$$\hat{\sigma}_\alpha^\dagger \rightarrow \hat{c}_\alpha^\dagger \quad \text{and} \quad \hat{\sigma}_\alpha \rightarrow \hat{c}_\alpha.$$

Under this approximation, the coefficients describing the creation of photons from the atomic state (2.36) may be written as

$$g_{\alpha\mathbf{q}\lambda}(t) \approx iK_{\mathbf{q}\lambda}^* \sum_{\gamma} e^{-i(\mathbf{q}-\mathbf{k}_L)\cdot\mathbf{r}_\gamma} \int_0^t d\tau e^{-i\omega_{\mathbf{q}\lambda}(t-\tau)} \langle \text{vac} | \hat{c}_\gamma(\tau) \hat{c}_\alpha^\dagger | \text{vac} \rangle, \quad (2.37)$$

such that it is the time correlation function of the bosonic operators that defines the photonic state created.

The time correlation function of the bosonic operator is calculated from the time evolution of the operator itself. This is governed by the master equation [92, 138]

$$\dot{\hat{c}}_\gamma(t) = \sum_{\alpha,\beta} \left[e^{-i\mathbf{k}_L \cdot \mathbf{r}_{\alpha\beta}} J_{\alpha\beta} (\hat{c}_\alpha^\dagger \hat{c}_\gamma \hat{c}_\beta - \hat{c}_\gamma \hat{c}_\alpha^\dagger \hat{c}_\beta) + e^{i\mathbf{k}_L \cdot \mathbf{r}_{\alpha\beta}} J_{\alpha\beta}^* (\hat{c}_\alpha^\dagger \hat{c}_\gamma \hat{c}_\beta - \hat{c}_\alpha^\dagger \hat{c}_\beta \hat{c}_\gamma) \right]$$

where all operators on the right hand side are taken to be at time t , $\mathbf{r}_{\alpha\beta} = \mathbf{r}_\alpha - \mathbf{r}_\beta$ and the matrix J , defined and explained in [93], contains details of multiple scattering events. In short, this matrix defines an operator that accounts for light scattering at multiple atoms as well as the interatomic dipole-dipole interactions and depends mainly on the relative orientation of the atomic transition dipole moments and the ratio between the interparticle separation and the wavelength of the laser, a/λ_L [92]. The master equation is vastly simplified by the recognition that it only contains one term which is not in normal order [123], the rearrangement of which leads to

$$\frac{d\langle \hat{c}_\gamma(t) \rangle}{dt} = - \sum_{\beta} e^{-i\mathbf{k}_L \cdot \mathbf{r}_{\gamma\beta}} J_{\gamma\beta} \langle \hat{c}_\beta(t) \rangle,$$

the equation of motion for the bosonic annihilation operator. To simplify the following steps the phase defined by the exponential is absorbed into the operators, which yields

$$\frac{d\langle \hat{c}'_\gamma(t) \rangle}{dt} = - \sum_{\beta} J_{\gamma\beta} \langle \hat{c}'_\beta(t) \rangle,$$

where $\hat{c}'_\gamma(t) \equiv e^{i\mathbf{k}_L \cdot \mathbf{r}_\gamma} \hat{c}_\gamma(t)$. In order to solve this equation of motion, which allows evaluation of the time correlation function seen in (2.37), the non-Hermitian

matrix J is written in terms of its eigenvalues κ and the eigenvector matrix χ as

$$J_{\gamma\beta} = \sum_{mn} \chi_{\gamma m} \kappa_n \delta_{mn} \chi_{m\beta}^{-1}.$$

Defining the eigenmodes of J as

$$C_k^{(\alpha)}(\tau) = \sum_{\gamma} \chi_{k\gamma}^{-1} (\hat{c}'_{\gamma}(\tau) \hat{c}'_{\alpha}{}^{\dagger}),$$

the quantum regression theorem for the time correlation function of a bosonic operator [139, 140]

$$\frac{d \langle \hat{c}'_{\gamma}(\tau) \hat{c}'_{\alpha}{}^{\dagger} \rangle}{d\tau} = - \sum_{\beta} J_{\gamma\beta} \langle \hat{c}'_{\beta}(\tau) \hat{c}'_{\alpha}{}^{\dagger} \rangle. \quad (2.38)$$

may be used to find their equation of motion as

$$\frac{d \langle C_k^{(\alpha)}(\tau) \rangle}{d\tau} = -\kappa_k \langle C_k^{(\alpha)}(\tau) \rangle.$$

The solution of this simple equation,

$$\langle C_k^{(\alpha)}(\tau) \rangle = e^{-\kappa_k \tau} \langle C_k^{(\alpha)}(0) \rangle,$$

is related to the time correlation function seen in (2.37), in such a way that it may be used to find

$$\begin{aligned} \langle \hat{c}'_{\gamma}(\tau) \hat{c}'_{\alpha}{}^{\dagger} \rangle &= \sum_k \chi_{\gamma k} \langle C_k^{(\alpha)}(\tau) \rangle = \sum_k \chi_{\gamma k} e^{-\kappa_k \tau} \langle C_k^{(\alpha)}(0) \rangle \\ &= \sum_{kl} \chi_{\gamma k} e^{-\kappa_k \tau} \chi_{kl}^{-1} \langle \hat{c}'_l(0) \hat{c}'_{\alpha}{}^{\dagger} \rangle, \end{aligned}$$

such that

$$e^{i\mathbf{k}_L \cdot \mathbf{r}_{\gamma\alpha}} \langle \hat{c}_\gamma(\tau) \hat{c}_\alpha^\dagger \rangle \equiv \sum_{kl} \chi_{\gamma k} e^{-\kappa_k \tau} \chi_{kl}^{-1} e^{i\mathbf{k}_L \cdot \mathbf{r}_{l\alpha}} \underbrace{\langle \hat{c}_l \hat{c}_\alpha^\dagger \rangle}_{=\delta_{l\alpha}}$$

$$\langle \hat{c}_\gamma(\tau) \hat{c}_\alpha^\dagger \rangle = e^{i\mathbf{k}_L \cdot \mathbf{r}_{\alpha\gamma}} \sum_k \chi_{\gamma k} e^{-\kappa_k \tau} \chi_{k\alpha}^{-1}.$$

This result may thus replace the time correlation in the definition of $g_{\alpha\mathbf{q}\lambda}(t)$ (2.37)

such that it becomes

$$g_{\alpha\mathbf{q}\lambda}(t) = iK_{\mathbf{q}\lambda} e^{-i(\omega_{\mathbf{q}\lambda} t - \mathbf{k}_L \cdot \mathbf{r}_\alpha)} \sum_{\gamma k} e^{-i\mathbf{q} \cdot \mathbf{r}_\gamma} \chi_{\gamma k} \int_0^t e^{(i\omega_{\mathbf{q}\lambda} - \kappa_k)\tau} d\tau \chi_{k\alpha}^{-1}$$

$$= iK_{\mathbf{q}\lambda} e^{-i(\omega_{\mathbf{q}\lambda} t - \mathbf{k}_L \cdot \mathbf{r}_\alpha)} \sum_{\gamma k} \chi_{\gamma k} e^{-i\mathbf{q} \cdot \mathbf{r}_\gamma} \frac{e^{(i\omega_{\mathbf{q}\lambda} - \kappa_k)t} - 1}{i\omega_{\mathbf{q}\lambda} - \kappa_k} \chi_{k\alpha}^{-1}. \quad (2.39)$$

The final step in the derivation is to apply the fact that the interesting regime is that where $t \gg 1/\Gamma_{\text{ag}}$, and since the eigenvalues $\kappa \propto \Gamma_{\text{ag}}$, the exponential $e^{-\kappa_k t}$ may be approximated as zero. In the limit of long times the final expression for the light generation coefficients may be written

$$g_{\alpha\mathbf{q}\lambda}(t) \approx -iK_{\mathbf{q}\lambda} e^{-i(\omega_{\mathbf{q}\lambda} t - \mathbf{k}_L \cdot \mathbf{r}_\alpha)} \sum_{\gamma, k} e^{-i\mathbf{q} \cdot \mathbf{r}_\gamma} \frac{\chi_{\gamma k} \chi_{k\alpha}^{-1}}{i\omega_{\mathbf{q}\lambda} - \kappa_k}, \quad (2.40)$$

which may now be used to find the angular photon distribution.

2.6.4 The Angular Density Matrix of the Single Photon State

This section concerns the description of the angular distribution of the emitted photon when only a single atomic excitation is present in the system. Using the bosonic operators given in the last section, the atomic state containing a single

collective excitation may be written as

$$|\psi(0)\rangle = |\Psi\rangle_{\text{at}} |0\rangle_{\text{ph}} = \sum_{j=1}^N \psi_j \hat{c}_j^\dagger |0\rangle_{\text{at}} |0\rangle_{\text{ph}},$$

where the coefficient ψ_j describes the particular collective excitation. The corresponding photonic state resulting after a large enough time may then be written as

$$|\psi(t \gg \tau)\rangle = |0\rangle_{\text{at}} |\Phi\rangle_{\text{ph}} = \sum_{j, \mathbf{q}, \lambda} \psi_j g_{j\mathbf{q}\lambda}(t) \hat{a}_{\mathbf{q}\lambda}^\dagger |0\rangle_{\text{at}} |0\rangle_{\text{ph}}. \quad (2.41)$$

The angular distribution of the state of the emitted photon is governed by the angular density matrix per solid angle, which is defined as [91]

$$\rho(\Omega_{\hat{q}}) = \frac{V}{(2\pi)^3} \sum_{\nu} \int_0^{\infty} dq \langle \psi(t \gg \tau) | \hat{a}_{\mathbf{q}\nu}^\dagger \hat{a}_{\mathbf{q}\nu} | \psi(t \gg \tau) \rangle q^2, \quad (2.42)$$

where $|\mathbf{q}| = q = \omega_{\mathbf{q}\lambda}/c$, is the modulus of the wavevector of the emitted photonic state. The expectation value of the final photonic state $|0\rangle_{\text{at}} |\Phi\rangle_{\text{ph}}$ may be evaluated by insertion of its explicit expression (2.41) to yield

$$\begin{aligned} \langle \hat{a}_{\mathbf{q}\nu}^\dagger \hat{a}_{\mathbf{q}\nu} \rangle &= \sum_{j, \mathbf{k}, \lambda} \sum_{j', \mathbf{k}', \lambda'} \psi_j \psi_{j'}^* g_{j\mathbf{k}\lambda}(t) g_{j'\mathbf{k}'\lambda'}^*(t) \langle \psi(t \gg \tau) | \hat{a}_{\mathbf{k}'\lambda'}^\dagger \hat{a}_{\mathbf{q}\nu}^\dagger \hat{a}_{\mathbf{q}\nu} \hat{a}_{\mathbf{k}\lambda} | \psi(t \gg \tau) \rangle \\ &= \sum_{j, j'} \psi_j \psi_{j'}^* g_{j\mathbf{q}\nu}(t) g_{j'\mathbf{q}\nu}^*(t). \end{aligned}$$

Insertion of this expression for the expectation value and that of the photon creation coefficients (2.40) into the density matrix per solid angle allows it to be expressed as

$$\begin{aligned} \rho(\Omega_{\hat{q}}) &= \left(\frac{\Omega_L}{\Delta_L} \right)^2 \frac{1}{2\epsilon_0} \frac{d_{\text{ga}}^2}{(2\pi c)^3} \sum_{j, j'} e^{i\mathbf{k}_L \cdot (\mathbf{r}_j - \mathbf{r}_{j'})} \psi_j \psi_{j'}^* \sum_{\nu} \left(\hat{d}_{\text{ga}} \cdot \mathbf{e}_{\mathbf{q}\nu} \right)^2 \\ &\quad \times \sum_{\substack{\gamma m \\ \beta n}} \chi_{\gamma m} \chi_{m j}^{-1} (\chi_{\beta n})^* (\chi_{n j'})^{-1} \mathcal{I}_{\gamma n \beta m}(\Omega_{\hat{q}}), \end{aligned}$$

with

$$\mathcal{I}_{\gamma n \beta m}(\Omega_{\hat{q}}) = \int_0^\infty \frac{e^{-i\frac{\omega_{\mathbf{q}\nu}}{c}\hat{q}\cdot(\mathbf{r}_\gamma - \mathbf{r}_\beta)}}{(\kappa_n^* + i\omega_{\mathbf{q}\nu})(\kappa_m - i\omega_{\mathbf{q}\nu})} \omega_{\mathbf{q}\nu}^3 d\omega_{\mathbf{q}\nu} \quad (2.43)$$

where in these expressions the dipole matrix elements have been expanded as $\mathbf{d}_{\text{ga}} = d_{\text{ga}} \hat{d}_{\text{ga}}$ under the assumption that the laser is linearly polarised and the transition matrix element is real, such that \hat{d}_{ga} is the unit vector in the direction of the dipole transition.

The integral $\mathcal{I}_{\gamma n \beta m}(\Omega_{\hat{q}})$ (2.43) is evaluated in [91] and as explained within is justified in the limit where the time it takes for the collective excitation to decay is much shorter than the time taken for light to pass through the extent of the system. In [91], this condition is represented as $\Gamma_n/c \ll 1/L$, where Γ_n is the collective decay rate of the atomic state, c is the speed of light and L is the length of the system. The worst case for the collective decay rate for the small systems investigated here may be estimated from the descriptions given in this reference, where it can be seen to be comfortably valid. Note also that in this limit the dependence of the photon distribution on the wavelength of the atomic transition is removed. The integral thus takes the form

$$\mathcal{I}_{\gamma n \beta m}(\Omega_{\hat{q}}) = \frac{2\pi\omega_L^3}{\kappa_n^* + \kappa_m} e^{-i|\mathbf{k}_L|\hat{q}\cdot(\mathbf{r}_\gamma - \mathbf{r}_\beta)},$$

such that the full expression for the angular density matrix is found to be

$$\begin{aligned} \rho(\Omega_{\hat{q}}) &= \frac{3\Gamma_{\text{ag}}}{4\pi} \sum_{j,j'} e^{i\mathbf{k}_L\cdot(\mathbf{r}_j - \mathbf{r}_{j'})} \psi_j \psi_{j'}^* \sum_{\nu} \left(\hat{d}_{\text{ga}} \cdot \mathbf{e}_{\mathbf{q}\nu} \right)^2 \\ &\times \sum_{\substack{\gamma, m \\ \beta n}} e^{-i|\mathbf{k}_L|\hat{q}\cdot(\mathbf{r}_\gamma - \mathbf{r}_\beta)} \frac{\chi_{\gamma m} \chi_{m j}^{-1} \chi_{\beta n}^* (\chi_{n j'}^{-1})^*}{\kappa_n^* + \kappa_m}. \end{aligned} \quad (2.44)$$

This expression, though close to completion, may be further simplified by the

introduction of the matrix

$$\mathcal{B}_{mj}(\Omega_{\hat{q}}) = \chi_{mj}^{-1} \sum_{\gamma=1}^N e^{-i|\mathbf{k}_L| \hat{q} \cdot \mathbf{r}_\gamma} \chi_{\gamma m},$$

yielding

$$\rho(\Omega_{\hat{q}}) = \frac{3\Gamma_{\text{ag}}}{4\pi} \sum_{j,j'} e^{i\mathbf{k}_L \cdot (\mathbf{r}_j - \mathbf{r}_{j'})} \psi_j \psi_{j'}^* \sum_{\nu} \left(\hat{d}_{\text{ga}} \cdot \mathbf{e}_{\mathbf{q}\nu} \right)^2 \sum_{m,n} \frac{\mathcal{B}_{mj}(\Omega_{\hat{q}}) \mathcal{B}_{nj'}^*(\Omega_{\hat{q}})}{\kappa_n^* + \kappa_m}.$$

Converting this into matrix form simplifies the notation somewhat

$$\begin{aligned} \rho(\Omega_{\hat{q}}) &= \frac{3\Gamma_{\text{ag}}}{4\pi} \sum_{\nu} \left(\hat{d}_{\text{ga}} \cdot \mathbf{e}_{\mathbf{q}\nu} \right)^2 \sum_{j,j'} \tilde{\psi}_{j'}^\dagger [\mathcal{B}^\dagger(\Omega_{\hat{q}}) \mathcal{A} \mathcal{B}(\Omega_{\hat{q}})]_{j'j} \tilde{\psi}_j \\ &= \frac{3\Gamma_{\text{ag}}}{4\pi} \sum_{\nu} \left(\hat{d}_{\text{ga}} \cdot \mathbf{e}_{\mathbf{q}\nu} \right)^2 \tilde{\psi}^\dagger \mathcal{B}^\dagger(\Omega_{\hat{q}}) \mathcal{A} \mathcal{B}(\Omega_{\hat{q}}) \tilde{\psi}, \end{aligned} \quad (2.45)$$

where $\tilde{\psi}_j = e^{i\mathbf{k}_L \cdot \mathbf{r}_j} \psi_j$ and the elements of the matrix \mathcal{A} are defined as

$$\mathcal{A}_{nm} = \frac{1}{\kappa_n^* + \kappa_m}.$$

Finally, using the fact that the unit vector in the direction of the transition dipole moment can be composed into three directions defined by the polarisation and propagation vectors of the emitted photon ($\mathbf{e}_{\mathbf{q}1}$, $\mathbf{e}_{\mathbf{q}2}$ and \hat{q}) as

$$\left(\hat{d}_{\text{ga}} \cdot \mathbf{e}_{\mathbf{q}1} \right)^2 + \left(\hat{d}_{\text{ga}} \cdot \mathbf{e}_{\mathbf{q}2} \right)^2 + \left(\hat{d}_{\text{ga}} \cdot \hat{q} \right)^2 = 1,$$

the sum over the polarisation may be found as

$$\sum_{\nu} \left(\hat{d}_{\text{ga}} \cdot \mathbf{e}_{\mathbf{q}\nu} \right)^2 \equiv \left[1 - \left(\hat{d}_{\text{ga}} \cdot \hat{q} \right)^2 \right].$$

Substitution of this representation of the sum yields the final expression for the

angular density matrix per solid angle as

$$\rho(\Omega_{\hat{q}}) = \frac{3\Gamma_{\text{ag}}}{4\pi} \left[1 - \left(\hat{\mathbf{d}}_{\text{ga}} \cdot \hat{\mathbf{q}} \right)^2 \right] \tilde{\psi}^\dagger \mathcal{B}^\dagger(\Omega_{\hat{q}}) \mathcal{A} \mathcal{B}(\Omega_{\hat{q}}) \tilde{\psi}, \quad (2.46)$$

which describes the probability of the photon being emitted into each direction around the atomic ensemble and will be used in the following sections to calculate the spatial distribution of the emitted photons.

2.7 The Emitted Photons

This section gives details of the single photon states that are produced from the collective atomic excitations using the mapping described in the previous section. The results for all three geometries are presented in this section, where the systems have been set up such that there are many common features. Firstly, it is considered that the lattices are in the xy -plane, with the atoms fixed perfectly at the centre of each lattice site. Secondly, as can be ensured by appropriate choice of the atomic levels, the dipoles of the atomic transition $|g\rangle_i \rightarrow |a\rangle_i$ are aligned and perpendicular to the plane of the lattice, $\hat{\mathbf{d}}_{\text{ga}} \parallel \hat{\mathbf{z}}$. The third and final parameter to be set is that of the laser momentum \mathbf{k}_L , which is also set perpendicular to the plane of the lattice, $\mathbf{k}_L \parallel \hat{\mathbf{z}}$. The fixing of these parameters leaves the form of the photon distribution resting purely on the ratio between the lattice spacing a and the laser wavelength λ_L . The following sections detail the photonic distributions from each of the three lattice geometries when the collective atomic excitation present is that with the highest transition intensity.

2.7.1 Square Lattice Emission

This section describes the angular photon distribution for four different ratios a/λ_L . The initial atomic state and the resulting photonic states for an $L_{\text{sq}} = 7$

square lattice are illustrated in Fig. 2.16, which shows that the ratio a/λ_L has

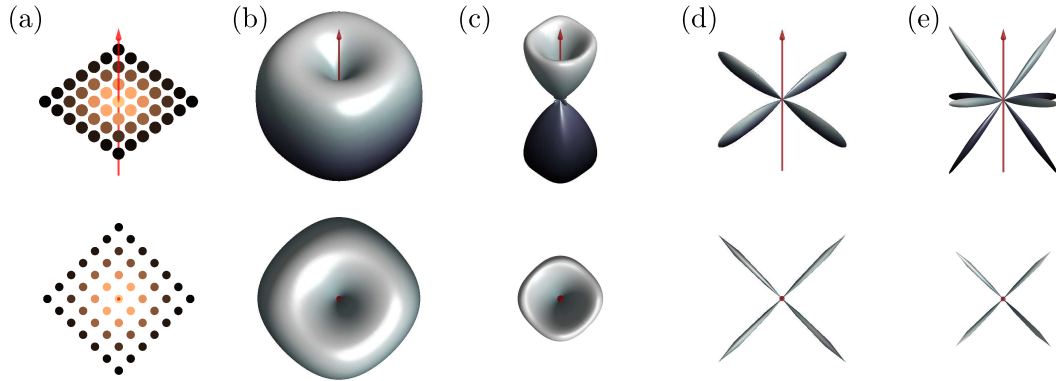


Figure 2.16: (a) Bosonic position expectation for the state $|1_N\rangle$. (b-e) The angular photon distributions for $L_{\text{sq}} = 7$ square lattices with: (b) $a/\lambda_L = 0.1$, (c) $a/\lambda_L = 0.25$, (d) $a/\lambda_L = 0.95$, (e) $a/\lambda_L = 1.2$. The red arrow represents the direction of the photon mapping laser, which is perpendicular to the lattice plane in the top row and out of the page in the bottom row.

a dramatic impact on the photonic state produced. The smallest illustrated ratio $a/\lambda_L = 0.1$, shown in 2.16(a), produces a slightly perturbed dipole emission pattern. This is due to the fact that the atoms couple to the field as almost a single degree of freedom, as indeed the whole lattice will actually fit within a single wavelength of the laser. However, the ratio and size of the lattice are clearly sufficient to alter the dipole emission pattern such that the lattice geometry leaves its mark, making the distribution square in appearance. When the ratio is reduced to $a/\lambda_L = 0.05$ a standard circular dipole emission pattern is seen, therefore the lattice geometry has no effect. Increasing the ratio of interparticle spacing to wavelength to $a/\lambda_L = 0.25$, the distribution for which is seen in Fig. 2.16(c), changes the photon emission profile into that where the photon is emitted into a superposition of directions that form two cone-shaped beams. Here the information about the geometry of the lattice is mapped into the shape of the two conical distributions, which, upon closer inspection, have square bases. There is a relatively large gap in the ratio a/λ_L to the next distribution shown,

$a/\lambda_L = 0.95$. This choice was made as the majority of the intermediate ratios merely show a crossover between the two regimes, the low ratio cones gradually reducing in intensity while the four perpendicular beams seen in 2.16(d) gain in prominence. The result shown in Fig. 2.16(d) once again shows that the lattice geometry is imprinted on the photonic state, with the four beams emitted perpendicular to the sides of the lattice. Furthermore, the beams are also perpendicular to the incident photon mapping laser, which will avoid problems with noise in the photon detection process. The final panel of the figure, Fig. 2.16(e), shows the photonic angular distribution when the minimum interparticle separation is greater than the mapping laser wavelength. This shows a similar distribution to that where $a/\lambda_L = 0.95$, though the four emitted beams are now split in two. In this case, the distribution will be given by the interference of the emission from a regular array of dipoles, which are coupled independently to the laser.

This section has detailed the results for photon emission from a square lattice with the highest energy collective bosonic excitation initially present. The following section details how the features seen here are also present in the triangular lattice case.

2.7.2 Triangular Lattice Emission

The angular photon distributions for the $L_{\text{tri}} = 7$ triangular lattice with four different ratios a/λ_L are shown in Fig. 2.17, along with the bosonic excitation position expectation value of the initial atomic state, which has been chosen to be that with the highest transition intensity, $|1_{N_{\text{tri}}}\rangle$. The result for the smallest ratio of interparticle spacing to mapping laser wavelength, $a/\lambda_L = 0.1$, shown in Fig. 2.17(b), shows once again a slightly altered dipole emission pattern. In this triangular case, the shape of this near-dipole emission pattern includes features related to both the external geometry of the system and the shaped formed by

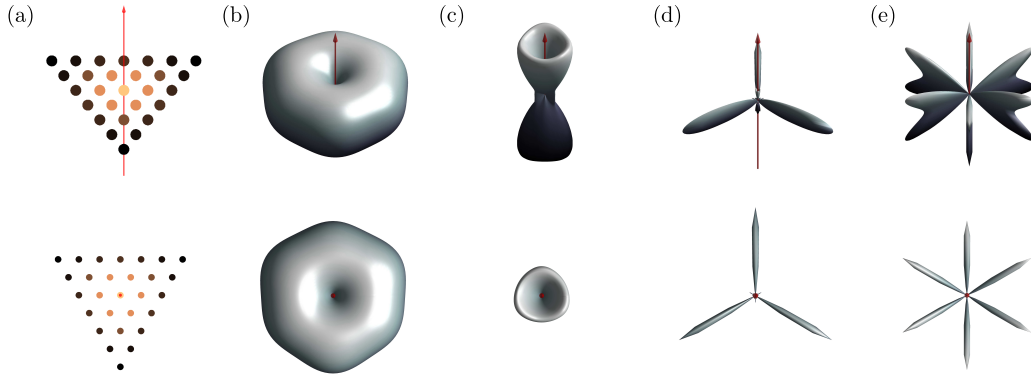


Figure 2.17: (a) Bosonic position expectation for the state $|1_{N_{\text{tri}}}\rangle$. (b-e) The angular photon distributions for $L_{\text{tri}} = 7$ triangular lattices with: (b) $a/\lambda_L = 0.1$, (c) $a/\lambda_L = 0.4$, (d) $a/\lambda_L = 0.9$, (e) $a/\lambda_L = 1.25$. The red arrow represents the direction of the photon mapping laser, which is perpendicular to the lattice plane in the top row and out of the page in the bottom row.

its neighbouring atoms. The internal triangular geometry of the system means that the central sites have six neighbours, thus being surrounded by a regular hexagon, as may be seen in 2.17(a). The emission pattern is an irregular hexagon with three symmetry axes, which are oriented in line with those of the lattice from which it is produced. An increase of the interparticle spacing to wavelength ratio to $a/\lambda_L = 0.4$, as shown in Fig. 2.17(c), yields the emission pattern of two pyramidal shaped beams which have a triangular base. As with the square lattice, information about the geometry of the system is mapped into the emitted photon. For ratios $0.4 < a/\lambda_L < 0.95$, the emission pattern shows a mixture of those shown in Fig. 2.17(c) and (d), with the two cones gradually decreasing in amplitude while the three beams gain intensity. As seen in 2.17(d), there are very small remnants of the conical beams visible, but the distribution is dominated by three beams emitted perpendicular to both the sides of the lattice and the mapping laser itself. What is also clear in this emission pattern is the emergence of three further beams, which, although at this point are much lower in intensity than the three main beams, appear to be emitted from the corners of the lattice.

Indeed, in between $a/\lambda_L = 0.95$ and that seen in the final subfigure, 2.17(e), these secondary peaks grow to an intensity equal to that of those which are emitted from the sides of the lattice. Increasing the ratio to $a/\lambda_L = 1.25$ the peaks begin to split in the z -direction. Further increase of the a/λ_L ratio (not shown) sees the beams in Fig. 2.17(e) split into two separate beams that eventually become perpendicular to each other, one 45° above the lattice plane and one 45° below it. This final image suggests that the emission pattern becomes dominated by the interference of individual dipole emissions arranged in a triangular lattice.

This section has shown that the emission patterns for the triangular lattice rely on both its external geometry and how the atoms are arranged within. This was not apparent in the square case as the central lattice sites always have neighbours arranged in a geometry which is the same as the overall lattice shape. This interplay is further highlighted in the following section, which details the emission from the lattice with the external geometry of a rhombus and a honeycomb internal structure.

2.7.3 Hexagonal Lattice Emission

The final set of photon distributions presented are those from the hexagonal lattice. The results for an $L_{\text{hex}} = 11$ hexagonal lattice are shown in Fig. 2.18, where the first subfigure is the bosonic position expectation value of the single excitation state with the highest energy. Once again, for very small ratios of the interparticle spacing to the mapping laser wavelength, an emission pattern closely resembling that of a single dipole is found. In this case it is the external geometry of the lattice which dominates, such that the dipole emission pattern is distorted to the shape of a rhombus. Increasing the interparticle separation in the hexagonal lattice case does not yield the emission pattern of two cones that was seen in both the previous cases. Instead, Fig. 2.18(c) shows four clearly defined

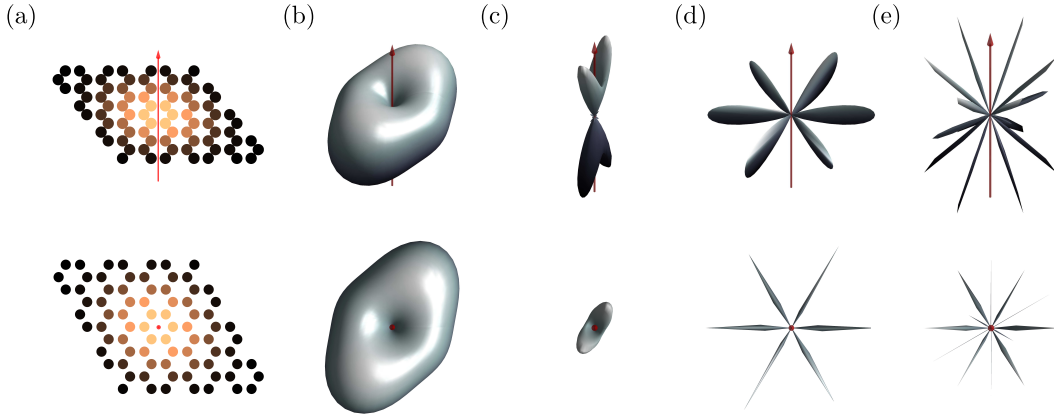


Figure 2.18: (a) Bosonic position expectation for the state $|1_{N_{\text{hex}}}\rangle$. (b-e) The angular photon distributions for $L_{\text{hex}} = 11$ hexagonal lattices with: (b) $a/\lambda_L = 0.05$, (c) $a/\lambda_L = 0.3$, (d) $a/\lambda_L = 0.65$, (e) $a/\lambda_L = 1.05$. The red arrow represents the direction of the photon mapping laser, which is perpendicular to the lattice plane in the top row and out of the page in the bottom row.

peaks, two from each face of the lattice. Further increase of the interparticle spacing relative to the mapping laser wavelength such that $a/\lambda_L = 0.65$ produces another interesting result, as seen in Fig. 2.18(d). In this case, there are six highly focused beams emitted perpendicular to the mapping laser, each one in a direction parallel to those along which nearest-neighbours of each lattice site lie. This is in contrary to the beams previously seen emitted perpendicular to the sides of the lattice, and is likely a result of the interplay between internal and external geometries. The final subfigure, Fig. 2.18(e), shows a transition to where the distribution appears as a number of interacting dipole emission patterns, as was seen for the previous lattice geometries, and occurs when the atoms in the lattice couple to the laser independently.

This section in particular has highlighted the complicated nature of the interplay between the internal and external geometries of the lattice when the collective excitations are used to generate single photons. It should be noted that these emission patterns are the same as those that can be calculated for arrays

of classical dipoles with the corresponding dimensions. Thus, there is nothing inherently quantum about the emission patterns themselves, although the singly occupied lattice system with a very small number of collective excitations present is a quantum system and may be mapped onto quantum states of the light field.

2.7.4 Uncertainty in Atomic Position

Unfortunately, due to the finite strength of the atomic confinement and finite temperature of any experiment, it is inevitable that perfect lattices are impossible to achieve in practice. This section shows how taking into account the uncertainty in the atomic positions affects the photonic state produced. To perform this calculation, the atoms are randomly distributed around the centres of the lattice sites with a finite isotropic standard deviation, $\sigma \neq 0$. As a result, the initial assumption that the width of the external atomic wavefunction was negligible compared to the interparticle separation, $\sigma/a \rightarrow 0$, breaks down. Examples of the results obtained when the atoms are randomly distributed about the centres of an $L_{\text{sq}} = 7$ square lattice of $a/\lambda_L = 0.95$ can be seen in Fig. 2.19, which shows the possible differences to those of the perfect trapping case seen in Fig. 2.16(b). The lowest standard deviation of the atoms about the centre of the lattice sites, seen in Fig. 2.19(a), shows that the atomic state is very close to that of the perfect trapping case (2.16(b)) and therefore the photonic state varies very little. In the second figure, 2.19(b), the standard deviation of the distribution is doubled to $\sigma/a = 0.05$, and is seen to greatly affect the collective excitation state. However, the photonic state produced by this distribution retains the qualitative features of the perfect distribution in that it still shows four perpendicular emitted beams. The examples of atomic distributions provided in 2.19(c) and (d), showing $\sigma/a = 0.075$ and $\sigma/a = 0.1$ respectively, show that the distribution of the emitted photonic state steadily diverges from that of the perfect trapping

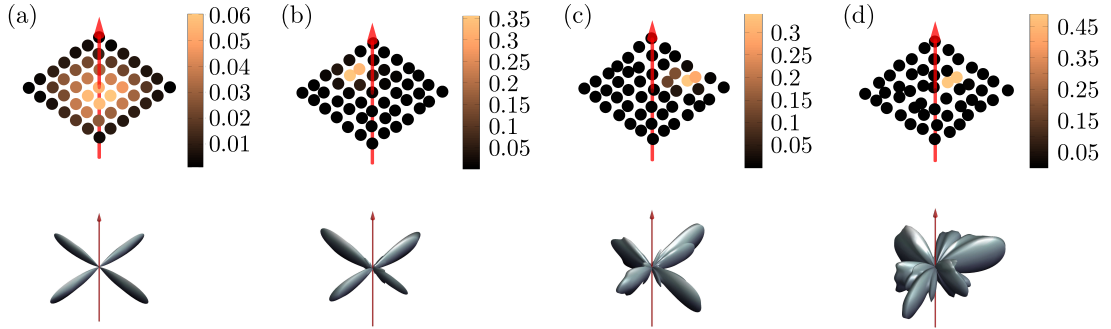


Figure 2.19: Examples of the atomic distributions and resulting photonic states when the atoms are randomly distributed about the centre of the sites of an $L_{\text{sq}} = 7$ square lattice with $a/\lambda_L = 0.95$ and (a) $\sigma/a = 0.025$ (b) $\sigma/a = 0.05$ (c) $\sigma/a = 0.075$ and (d) $\sigma/a = 0.1$. The red arrow represents the direction of the photon mapping laser, which is perpendicular to the lattice plane.

case. Whilst the perpendicular beams are retained up to this level of uncertainty, they become increasingly noisy and asymmetric, which is to be expected.

The results for the square lattice are qualitatively representative of the other lattices that have been considered, both of which retain their qualitative features over this range of σ/a , but with increasing noise. Therefore this final section shows a degree of robustness of the photonic states when certain elements of the experimental uncertainty are introduced. It should be noted that the emission pattern is expected to retain its qualitative features in the case where a small number of lattice sites are completely unoccupied, though this case has not been investigated.

2.8 Summary and Outlook

This chapter has shown how quantum states of light may be produced from collective excitations stored in an atomic ensemble. Focus was at first placed upon the situation where the laser driving is the dominant energy scale of the system. Such a regime allows the atomic operators to be converted to bosonic operators

via application of the Holstein-Primakoff approximation, such that the system has a coarse energy spectrum formed of quasi-degenerate manifolds defined by the number of bosonic excitations present. Following a description of how these manifolds may be coupled by the application of an oscillating laser detuning, it is shown that the excitation spectra are governed by conservation of the symmetry properties of the initial state, which is in turn dependent on the lattice geometry. The validity of the solutions obtained in the strong laser driving regime are then evaluated using a numerical exact diagonalisation technique, the derivation of which is detailed. This shows that the two methods clearly converge when the laser driving becomes dominant in the numerical approach, such that the reliability of the results is confirmed. Attention then turns to the generation of non-classical states of light from the obtainable collective excitation states, where, after an extensive derivation, the angular photonic distributions are illustrated for each of the three lattice geometries. A common theme to these distributions is that the lattice geometry is essentially mapped into the photonic angular distribution. Furthermore, for certain parameter regimes the photonic distributions are seen to be in directions strictly perpendicular to the lasers applied to the system.

This work has shown that it is possible to map an atomic ensemble in a collective excitation state onto the state of a single photon, thus creating a deterministic source of single photons. One example where this ability to convert between atomic and photonic states is a quantum network where the atomic states act as quantum memories with photons transferring information between them [141]. Especially, this is a possible method to achieve one of the three requirements for a distributed quantum computer networks outlined in [48], namely the retrieval of a quantum state from an atomic memory.

There are a number of conceivable ways in which the work detailed here

may be extended or taken in a different direction. Section 2.7 was concerned only with the case where both the incident laser and the atomic dipoles are aligned in a direction perpendicular to the lattice. Simple extensions to this case may be envisaged as having the dipoles all aligned in one direction, but not necessarily aligned with the readout laser and either or both not aligned perpendicular to the lattice plane. These situations are all accounted for in the equations given in section 2.6, but have not been considered here. One obvious extension is to further increase the dimensions of the system to atoms trapped in a three dimensional lattice, where the Holstein-Primakoff transformation allowing solution of the Hamiltonian will still be valid. A completely separate extension to this work would be the case of a lattice small enough such that only a single site may be in the Rydberg state at any one time due to the Rydberg blockade [74]. This situation may guarantee that only a single collective excitation is present in the lattice, though the relevant energy scales still require investigation.

Chapter 3

Rydberg State Control using Electrons

3.1 Introduction and Background

The relentless drive to understand quantum many-body systems continually stimulates research aiming to increase the accuracy and diversity of quantum state control. One particular area where this is apparent is in those many-body systems made possible by high accuracy trapping and manipulation of ultracold atoms [1]. Aiming to utilise these high degrees of control, ultracold atoms in optical lattices [22] have formed the basis for a number of quantum computing proposals [41–44]. These require two internal states of the atom being used to form a quantum bit, which is the basis for storage, retrieval and processing of quantum information [142]. Such proposals place stringent demands upon ones ability to create and manipulate the quantum state of the system, this fact being one of the driving forces behind the study of interfacing quantum systems with solid state devices [79–83].

Atoms in Rydberg states [66] are frequently proposed as suitable candidates

for quantum computation [69,85,143–145] and have proved exceptionally useful in the study of the complex dynamics of many-body systems [74,87,96–98]. This is down to the techniques that have been developed to precisely control the internal state of the atom. The extreme sensitivity of these atoms to electromagnetic fields is well documented [76–78] and their typical level spacings allow microwave fields to be used to induce transitions between neighbouring Rydberg states [146,147].

While the use of microwave fields to alter the state of Rydberg atoms is a very powerful technique, it has also been recognised that collisions between the atom and various other particles may change the atomic state. A very detailed report on theoretical descriptions of collisions between Rydberg atoms and both charged and neutral particles may be found in [99]. Part of this report expands upon previous work [100] detailing how collisions between Rydberg atoms and low energy electrons may lead to changes in the orbital angular momentum state of the atom. Whilst the problem of collisions between Rydberg atoms and electrons has long been treated using classical Monte Carlo methods [148–150], with some of the earlier results being used to produce analytic formulae for ionisation and populations rates [151], it has not been until relatively recently that they have been treated quantum mechanically [152]. Further to these theoretical descriptions, Rydberg state changes have been observed experimentally in cold Rydberg gases [153–155] where they are attributed to collisions with electrons which have been released when a small proportion of the atoms ionise. This mechanism for the formation of such an ultracold plasma is explained in the first of these three references, [153]. The route which will be explored here is closely related to these collisional ideas, but aims to actively control the state of the Rydberg atom. This chapter thus describes how this control may be achieved using the interaction of the Rydberg atom with a passing guided electron [156]. It will be shown that this relatively simple technique may be used to excite the atom to a quantum

state which has a permanent electric dipole, and that the required parameters are achievable using current technology.

This chapter is structured as follows. Section 3.2 introduces the system and the full form of its Hamiltonian. Section 3.3 gives a detailed description of a preliminary investigation of the interaction inherent in the system, which is based upon perturbation theory. This method is then superseded in section 3.4 by two analytic techniques which, under certain assumptions, are capable of describing the changing state of the atom with the passage of the electron. This section concludes with an analysis of the results from these two methods. Inevitably with such a complex system, a numerical analysis is required and this is described in section 3.5, where a comprehensive analysis of the results for both rubidium and lithium is provided. The final aspect of this research is found in section 3.6, which describes how the analysis may be extended to a system of multiple trapped and interacting Rydberg atoms, and concludes with the results for a two atom system. The chapter concludes with a brief summary of the research presented, along with a small number of possible extensions. This may be found in section 3.7.

3.2 System and Hamiltonian

The system considered here, shown in Fig. 3.1, is composed of two elements and will serve as the basis for all the methods described in this chapter, with any variations being described when necessary. The first element is an electron confined to move in a single dimension, which defines the x -axis of the system. The quantum state of such an electron can be written as a linear combination of either the continuum of states in the position basis $|x\rangle$ or the continuum (when the wire is considered infinite in length) of states in the momentum basis $|k\rangle$. The second element of the system is an alkali atom trapped at a perpendicular distance Y from the wire and initially in a $|ns\rangle$ Rydberg state ($n \gg 1$) [66],

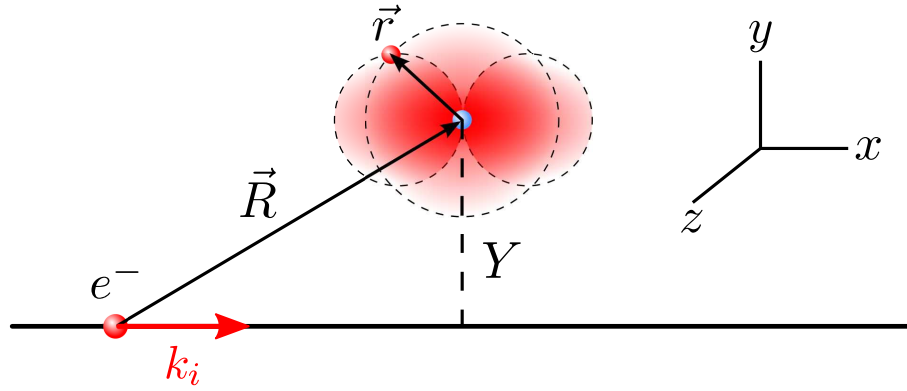


Figure 3.1: A schematic of the system considered. A Rydberg atom is trapped a distance Y from a quantum wire which directs a single electron moving with momentum k_i . This depiction of the atom represents the fact that the atom may change state on the passage of the atom, as detailed throughout this chapter.

where n is the principal quantum number of the state and s represents that the orbital angular momentum quantum number $l = 0$. Introducing also the magnetic quantum number, m , with the quantisation in the z -direction, the set of atomic states will be written as

$$|\alpha\rangle = |nlm\rangle = \mathcal{R}_{nl}(r)Y_l^m(\theta, \varphi)$$

where \mathcal{R}_{nl} are the radial wavefunctions specific to the atomic species in question and Y_l^m are the spherical harmonic functions. Note that in writing the atomic states in this form, the fine structure splitting brought about by the spin orbit interaction [157] has been neglected, which is justified towards the end of section 3.3.2. In writing the atomic states in this hydrogenic form a simplified model of the Rydberg atom is assumed, where it consists of a single valence electron and a positive core formed by the atomic nucleus and the other bound electrons. The distance between the free electron and the centre of mass of the atom is $\vec{R} = (x, Y, 0)$ and the relative coordinate of the valence electron and the nucleus is $\vec{r} = (x_a, y_a, z_a)$.

The Hamiltonian of the system has three terms,

$$H = H_E + H_A + H_{\text{int}}, \quad (3.1)$$

and it should be noted that atomic units are to be used throughout this section, the definitions of which can be seen in appendix A. In the momentum basis, the Hamiltonian describing the one-dimensionally confined electron is written as

$$H_E = \int dk \frac{k^2}{2} |k\rangle \langle k| \otimes \mathbb{I}_A, \quad (3.2)$$

where $k^2/2$ is the kinetic energy of the electron and $\mathbb{I}_A = \sum_{\alpha} |\alpha\rangle \langle \alpha|$ is the identity operator on the atomic Hilbert space. The Hamiltonian of the atom can be written as

$$H_A = \mathbb{I}_E \otimes \sum_{\alpha} \mathcal{E}_{\alpha} |\alpha\rangle \langle \alpha|, \quad (3.3)$$

where $\mathbb{I}_E = (L/2\pi) \int dk |k\rangle \langle k|$ is the identity operator represented in the continuum of 1D electron momentum states, L is the length of the wire within which the electron is confined and \mathcal{E}_{α} is the energy of the atomic state $|\alpha\rangle$. The eigenstates of the composite system before the interaction is introduced are written as $|k, \alpha\rangle = |k\rangle \otimes |\alpha\rangle$ and have an associated energy $E_{k,\alpha} = \mathcal{E}_{\alpha} + \frac{k^2}{2}$. The Hamiltonian describing the interaction between the two elements of the system is a Coulomb potential, written as

$$H_{\text{int}} = \frac{1}{|\vec{r} - \vec{R}|} - \frac{1}{|\vec{R}|}. \quad (3.4)$$

This contains both the repulsive interaction between the electron in the wire and the valence electron (first term) and the attractive interaction between the electron in the wire and the atomic core (second term).

It is considered that the atomic trapping distance Y be on the order of micrometres. Thus, when considering that the orbital radius of the valence electron

may be estimated as $\langle r \rangle \approx 3/2 \times n^2$ [66], it can be approximated that for the experimentally accessible Rydberg states ($n = 90$ demonstrated in [74]), $Y \gg |\vec{r}|$ and a Taylor expansion of the interaction about $|\vec{r}| = 0$ may be performed. The zeroth order term in the Taylor expansion of the first term in H_{int} (3.4) can be shown to be $1/|\vec{R}|$, and therefore to zeroth order $H_{\text{int}} \approx 0$. Therefore the first order expansion is performed and found to be

$$H_{\text{int}} \approx \frac{\hat{x}\hat{x}_a + Y\hat{y}_a}{(\hat{x}^2 + Y^2)^{\frac{3}{2}}} = \frac{1}{2} \left[(\hat{x}_a + i\hat{y}_a) \frac{\hat{x} - iY}{(\hat{x}^2 + Y^2)^{\frac{3}{2}}} + (\hat{x}_a - i\hat{y}_a) \frac{\hat{x} + iY}{(\hat{x}^2 + Y^2)^{\frac{3}{2}}} \right], \quad (3.5)$$

which approximately describes the interaction between the two systems. In this expression, \hat{x} is the position operator of the one-dimensionally confined electron with \hat{x}_a and \hat{y}_a being the position operators of the valence electron relative to the nucleus. The final form separates the wire electron position operators from those of the valence electron and allows this interaction to be written in the atomic basis,

$$H_{\text{int}} = \frac{1}{2(\hat{x}^2 + Y^2)^{\frac{3}{2}}} \sum_{\alpha\alpha'} \left[\mu_{\alpha\alpha'} (\hat{x} - iY) |\alpha\rangle \langle\alpha'| + \mu_{\alpha'\alpha}^* (\hat{x} + iY) |\alpha'\rangle \langle\alpha| \right], \quad (3.6)$$

where

$$\mu_{\alpha\alpha'} = \langle\alpha|\hat{x}_a + i\hat{y}_a|\alpha'\rangle$$

are the dipole matrix elements of the transition $|\alpha\rangle \rightarrow |\alpha'\rangle$.

3.3 Preliminary Investigation

The investigation of this system begins under the assumption that the energy scale of the interaction is much less than the energy scales of the individual systems. This section details how perturbation theory [158] can be used to assess how the energy levels of the system are changed with the introduction of the interaction.

The first order corrections to the energy levels of the system are defined as

$$E_{k,\alpha}^{(1)} = \langle k, \alpha | H_{\text{int}} | k, \alpha \rangle,$$

where H_{int} is defined in (3.6). These first order corrections may be shown to be zero using the form of the dipole matrix elements provided in appendix E, which show that in order for a dipole matrix element to be non-zero both the orbital angular momentum and magnetic quantum numbers of the states involved must be different by ± 1 . Obviously this cannot be the case for the diagonal elements seen in the first order correction expression.

The second order corrections to the energy levels are worked out using

$$E_{k,\alpha}^{(2)} = \sum_{\substack{k' \neq k \\ \alpha' \neq \alpha}} \frac{|\langle k', \alpha' | H_{\text{int}} | k, \alpha \rangle|^2}{E_{k,\alpha} - E_{k',\alpha'}},$$

where, given that the interaction can indeed be taken as a perturbation, we are interested only in the shift of the state $|ns\rangle$, in which the atom is initially prepared. Therefore, the only states $|\alpha'\rangle$ which contribute to this energy shift are those where a transition from $|ns\rangle$ is allowed by H_{int} . As the interaction Hamiltonian only allows dipole transitions, it may be written in the basis containing only the initial atomic state, $|ns\rangle$, and the two p -states, $|n'p_+\rangle$ ($m = +1$) and $|n'p_-\rangle$ ($m = -1$), to which dipole transitions are allowed. There are no selection rules to govern a change in principal quantum number, n . Taking this into account, the interaction Hamiltonian may be written using the basis $\{|n's\rangle, |n'p_+\rangle, |n'p_-\rangle\} \forall n'$ as

$$H_{\text{int}}^{(2)} = \frac{1}{2(\hat{x}^2 + Y^2)^{\frac{3}{2}}} \sum_{n', n''} \mu_{n'n''} \left[(\hat{x} - iY) (|n's\rangle \langle n''p_-| - |n''p_+\rangle \langle n's|) \right. \\ \left. (\hat{x} + iY) (|n''p_-\rangle \langle n's| - |n's\rangle \langle n''p_+|) \right], \quad (3.7)$$

where

$$\mu_{n'n''} = \pm \langle n's | x_a \pm iy_a | n''p_{\mp} \rangle = \pm \langle n''p_{\mp} | x_a \mp iy_a | n's \rangle$$

are the transition dipole matrix elements between the $|n's\rangle$ and $|n''p\rangle$ states.

The electron is assumed to be confined to a wire of length L , such that the states which it may occupy are written as

$$\langle x | k \rangle = \frac{1}{\sqrt{L}} e^{ikx}, \quad \text{with} \quad k = \frac{2\pi j}{L}$$

and j an integer. Taking the limit $L \rightarrow \infty$ means that the possible values of momentum which the electron may take become a continuum, therefore the difference between them $dk = 2\pi/L \rightarrow 0$, and the sum over k' may be turned into an integral $\sum_{k'} \rightarrow L/2\pi \int dk'$ [159]. In this limit, the expression for the second order correction to the energy levels is written as

$$E_{k,\alpha}^{(2)} = \frac{L}{2\pi} \sum_{\alpha' \neq \alpha} \int_{-\infty}^{\infty} dk' \frac{\left| \langle k', \alpha' | H_{\text{int}}^{(2)} | k, \alpha \rangle \right|^2}{E_{k,\alpha} - E_{k',\alpha'}}. \quad (3.8)$$

Expressions for the matrix elements $\langle k', \alpha' | H_{\text{int}}^{(2)} | k, \alpha \rangle$ may also be found analytically

$$\begin{aligned} \langle k', n'p_+ | H_{\text{int}}^{(2)} | k, ns \rangle &= -\frac{\mu_{nn'}}{2L} \int_{-\infty}^{\infty} dx e^{i(k-k')x} \frac{x - iY}{(x^2 + Y^2)^{\frac{3}{2}}} = -\frac{i\mu_{nn'}}{L} \mathcal{F}(k - k') \\ \langle k', n'p_- | H_{\text{int}}^{(2)} | k, ns \rangle &= \frac{\mu_{nn'}}{2L} \int_{-\infty}^{\infty} dx e^{i(k-k')x} \frac{x + iY}{(x^2 + Y^2)^{\frac{3}{2}}} = \frac{i\mu_{nn'}}{L} \mathcal{G}(k - k'), \end{aligned}$$

where

$$\mathcal{F}(k - k') = (k - k')K_0(Y |k - k'|) - |k - k'| K_1(Y |k - k'|) \quad (3.9)$$

$$\mathcal{G}(k - k') = (k - k')K_0(Y |k - k'|) + |k - k'| K_1(Y |k - k'|) \quad (3.10)$$

and K_n is the n^{th} modified Bessel function of the second kind. The functions $\mathcal{F}(k - k')$ and $\mathcal{G}(k - k')$ are momentum space coupling functions between the two states of the system, as the integral amounts to a Fourier transform of the position space coupling found in H_{int} .

These expressions highlight a problem with such a perturbative approach. There is the possibility that the second order correction (3.8) could diverge at the point where $E_{k,p} = E_{k',s}$ provided that the momentum space coupling functions \mathcal{F} and \mathcal{G} are non-zero for these momentum differences. This amounts to the kinetic energy difference between the states of the electron being equal to the energy difference between the atomic states which are coupled by the interaction. Therefore, the validity of such a perturbative approach is questionable. However, before abandoning this method, an investigation is carried out which limits the kinetic energy to being much lower than the atomic energy level differences. This is detailed in the following section.

3.3.1 The Born Oppenheimer Approximation

In this section the Born Oppenheimer approximation [160] is applied to the system. In this context, it is assumed that the electron is travelling slowly enough that the atomic energy shifts may be calculated as if it was fixed in position. Therefore the energy shifts found are Stark shifts dependent upon the strength of the electric field experienced by the atom due to the electron. Quantifying this, the kinetic energy of the electron is restricted to being much less than the energy gap between the initial state $|ns\rangle$ and any of the possible $|n'p\rangle$ states, $|\Delta\mathcal{E}_{n'p}| = |\mathcal{E}_{n'p} - \mathcal{E}_{ns}|$, which avoids the points at which the second order perturbation predicts a divergence. The position of the electron x is thus a quasi-static variable which parameterises the effective interaction between the confined electron and the atom. The validity of this approximation rests on the assumption

that the kinetic energy of the electron in the wire can be completely neglected. To enforce this, H_E is neglected from the Hamiltonian, resulting in an effective Hamiltonian written as $H_{\text{BO}} = H_{\text{int}}^{(2)}(x) + H_A$, where $H_{\text{int}}^{(2)}(x) = H_{\text{int}}^{(2)}$ with the operator status of \hat{x} removed. The system then remains limited to the s - and p -state subspace.

Assuming the atom is initially prepared in the state $|ns\rangle$, the second order correction to its energy level may be written in the Born Oppenheimer approximation as

$$E_{ns}^{(2)}(x) = \sum_{n',v=\pm} \frac{\left| \langle n'p_v | H_{\text{int}}^{(2)}(x) | ns \rangle \right|^2}{\mathcal{E}_{ns} - \mathcal{E}_{n'p}}.$$

The number of states that need to be included in the summation in order to reach convergence depends upon the choice of atomic species. Rubidium is taken here, the spectrum and transition dipole moments of which can be seen in Fig. 3.2. The

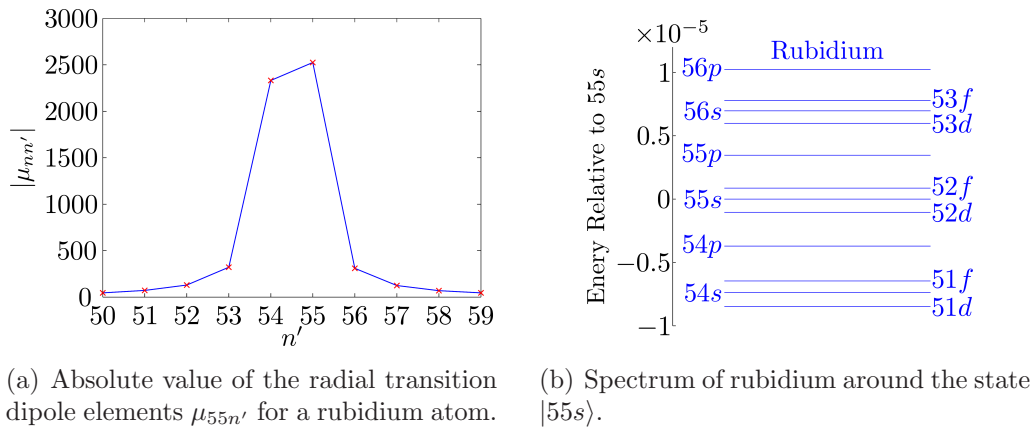


Figure 3.2: Radial transition dipole elements $|\mu_{55n'}|$ and energy spectrum for rubidium.

plot of the transition dipole moments, Fig. 3.2(a), is dominated by μ_{55} ($\mu_{nn} \equiv \mu_n$) and $\mu_{55,54}$, which combined with the spectrum, Fig. 3.2(b), shows that only the states $|55p_{\pm}\rangle$ and $|54p_{\pm}\rangle$ are going to contribute significantly to the shift of the energy of $|55s\rangle$. Having also verified that the spectrum and form of the transition dipole elements maintain a similar form for a wide range of principal quantum

numbers (omitted), the important principal quantum number manifolds in these energy shifts will be those of the initial n along with those of $n-1$. The expression is then written as

$$E_{ns}^{(2)}(x) \approx \frac{1}{2(x^2 + Y^2)^2} \left(\frac{\mu_n^2}{\mathcal{E}_{ns} - \mathcal{E}_{np}} + \frac{\mu_{n,(n-1)}^2}{\mathcal{E}_{ns} - \mathcal{E}_{(n-1)p}} \right),$$

the maximum magnitude of which will clearly be found when $x = 0$, and will be written as

$$E_{\max} = \frac{1}{2Y^4} \left(\frac{\mu_n^2}{\mathcal{E}_{ns} - \mathcal{E}_{np}} + \frac{\mu_{n,(n-1)}^2}{\mathcal{E}_{ns} - \mathcal{E}_{(n-1)p}} \right), \quad (3.11)$$

the sign of this being evaluated in the following paragraph.

Turning once more to the properties shown in Fig. 3.2, it is clear that $\mu_n > \mu_{n,n-1}$ and $|\mathcal{E}_{np}| > |\mathcal{E}_{n-1p}|$, with $\mathcal{E}_{np} > 0$ and $\mathcal{E}_{n-1p} < 0$ when offset such that $\mathcal{E}_{ns} = 0$. This means E_{\max} is actually a minimum when the atom is prepared in the state $|ns\rangle$, which opens up the possibility of bound states of the atom and electron system forming. Expanding about the minimum of $E_{ns}^{(2)}$ to second order we may write

$$E_{ns}^{(2)} \approx \frac{1}{2}\omega^2 x^2; \quad \omega = \frac{\sqrt{2}}{Y^3} \left(\frac{\mu_n^2}{\mathcal{E}_{ns} - \mathcal{E}_{np}} + \frac{\mu_{n,(n-1)}^2}{\mathcal{E}_{ns} - \mathcal{E}_{(n-1)p}} \right)^{\frac{1}{2}}$$

and assume that the lowest energy bound states are roughly one-dimensional harmonic oscillator states with energy $E_{n_{\text{HO}}} = (n_{\text{HO}} + 1/2)\omega$ [161]. Using quantum defect calculations [162] and numerically generated rubidium wavefunctions, the scalings of the quantities in the large brackets are estimated as follows; $\mu_n \approx 0.9n^2$, $\mu_{n,(n-1)} \approx 0.8n^2$, $\Delta\mathcal{E}_{np} = \mathcal{E}_{np} - \mathcal{E}_{ns} \approx 0.5n^{-3}$ and $\Delta\mathcal{E}_{(n-1)p} = \mathcal{E}_{(n-1)p} - \mathcal{E}_{ns} \approx -0.6n^{-3}$. These allow the maximum value of the energy shift, E_{\max} (3.11), to be estimated as

$$E_{\max} \approx -\frac{4}{15} \frac{n^7}{Y^4}.$$

An estimate of the harmonic trapping frequency ω can thus be found in the same way, yielding

$$\omega \approx \frac{4}{\sqrt{15}} \frac{n^{\frac{7}{2}}}{Y^3},$$

which allows a rough estimate of the number of bound states possible as

$$n_{\text{bound}} \approx \frac{|E_{\text{max}}|}{\omega} - \frac{1}{2} \approx \frac{n^{\frac{7}{2}}}{\sqrt{15}Y^3} - \frac{1}{2}.$$

Using this approximation with principal quantum number $n = 55$ and $Y = 2.5\mu\text{m}$ the number of bound states may be estimated as $n_{\text{bound}} \approx 6$. Although this is a low number, it acts only as an order estimate as the harmonic approximation assumes the spectrum of bound states to be linear. These bound states can be seen using numerical diagonalisation of the full problem when the electron kinetic energy is very small. This simulation of the system shows 12 bound states, double that predicted by the analytics. The six lowest energy numerically calculated bound states along the x -direction, $\psi_n(x)$, can be seen in Fig. 3.3. Also included in this figure are the energy levels for a harmonic potential (dashed lines) of the same depth, calculated using the energy difference between the two lowest energy numerical bound states as the harmonic frequency ω . This shows why more bound states are found than are predicted. The harmonic spectrum is linear in its energy spacing, which gives the six equally spaced predicted bound states seen in the figure. As the harmonic approximation breaks down, the bound state energies become closer together and therefore more are possible.

The harmonic approximation appears to be valid for the low energy bound states, which allows an estimate to be made for the characteristic timescale of the trapped electron as

$$\tau_{\text{E}} = \frac{2\pi}{\omega}.$$

For the electron and atom to form a bound state this timescale must be much

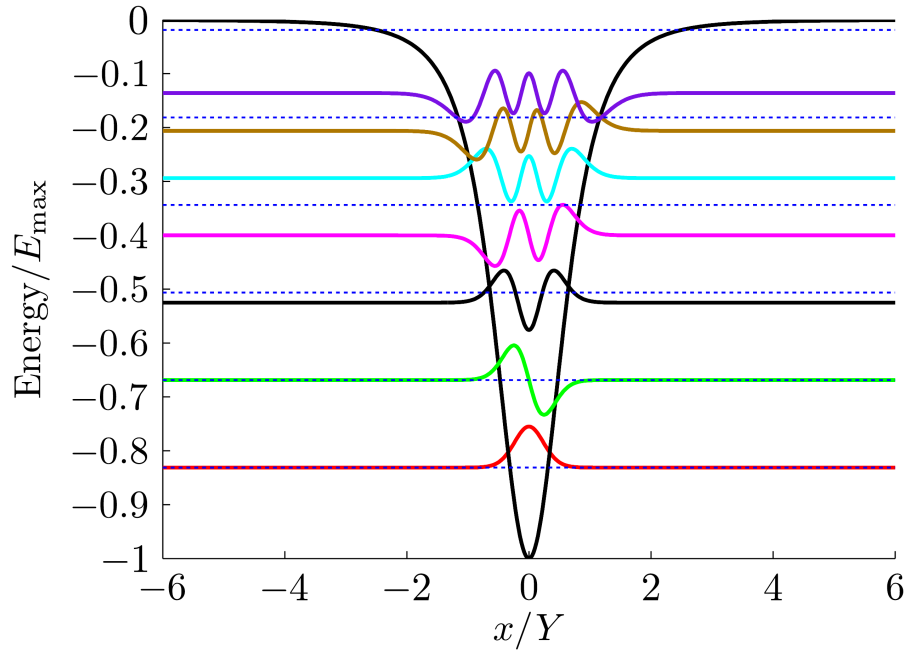


Figure 3.3: The six lowest energy bound states possible, $\psi_n(x)$, and the potential for a $|55s\rangle$ rubidium atom trapped $Y = 2.5\mu\text{m}$ from the electron wire. Dashed lines represent the energies for a harmonic potential of this depth.

shorter than the lifetime of the Rydberg atom. An electron trapped by a $|55s\rangle$ rubidium atom at $Y = 2.5\mu\text{m}$ has a characteristic timescale of $\tau_E \approx 25\text{ns}$, very short considering that the lifetime of this atomic state is $191\mu\text{s}$ at zero temperature [163].

Having shown that it is possible to gain some understanding of the system in the limit where the electron momentum is very small, the following section details an analysis aimed at going beyond this approximation.

3.3.2 Beyond Perturbation Theory

It is expected that the passage of the electron could change the internal state of the atom if its momentum were to change in order to conserve energy. In this case, the kinetic energy of the electron cannot be neglected as it is a process of this type which could cause the divergence in the second order perturbative

energy correction. This section describes the solution of the time-independent Schrödinger equation using the full system Hamiltonian, H (3.1), an approach that has recently been used to determine the fraction of atoms transferred to higher angular momentum states in an interacting cold Rydberg gas [155]. The state of the system will be written as

$$|\Psi\rangle = \sum_{n',\alpha} \int_{-\infty}^{\infty} dx \psi_{n'\alpha}(x) |x, n'\alpha\rangle,$$

where the position basis $|x\rangle$ is chosen as a convenient basis in which to express the interaction and $\psi_{n\alpha}(x)$ is a continuous function describing the coefficients of the component states $|x, n\alpha\rangle$. The Schrödinger equation for such a state is written as

$$E \sum_{n',\alpha} \int_{-\infty}^{\infty} dx \psi_{n'\alpha}(x) |x, n'\alpha\rangle = \sum_{n',\alpha} \int_{-\infty}^{\infty} dx \psi_{n'\alpha}(x) H |x, n'\alpha\rangle,$$

where the eigen-equations for the coefficients may be obtained by multiplying from the left by $\langle x', n''\alpha' |$. The assumption is made that the atom is allowed to make only a single transition from its initial state, $|ns\rangle$, thus limiting the basis to only this initial state and the $|n'p_{\pm}\rangle$ states. The eigenvalue equations are then written as

$$\begin{aligned} E \sum_{n',\alpha} \int dx \psi_{n'\alpha}(x) \langle x' | x \rangle \langle n''p_+ | n'\alpha \rangle &= \sum_{n',\alpha} \int dx \psi_{n'\alpha}(x) \langle x', n''p_+ | H | x, n'\alpha \rangle \\ E \sum_{n',\alpha} \int dx \psi_{n'\alpha}(x) \langle x' | x \rangle \langle n''p_- | n'\alpha \rangle &= \sum_{n',\alpha} \int dx \psi_{n'\alpha}(x) \langle x', n''p_- | H | x, n'\alpha \rangle \\ E \sum_{n',\alpha} \int dx \psi_{n'\alpha}(x) \langle x' | x \rangle \langle ns | n'\alpha \rangle &= \sum_{n',\alpha} \int dx \psi_{n'\alpha}(x) \langle x', ns | H | x, n'\alpha \rangle, \end{aligned}$$

where the integrals are over all x and in the third equation the fact that the only possible s -state is the initial state ($|ns\rangle$) has been used. With knowledge of the truncated basis interaction Hamiltonian provided previously (3.7), these three

equations may now be written

$$\begin{aligned}
E\psi_{n''p_+}(x) &= \left(-\frac{\partial_x^2}{2} + \Delta\mathcal{E}_{n''p}\right)\psi_{n''p_+}(x) - \sum_{n'} \frac{\mu_{n'n''}}{2} A^*(x)\psi_{n's}(x) \\
E\psi_{n''p_-}(x) &= \left(-\frac{\partial_x^2}{2} + \Delta\mathcal{E}_{n''p}\right)\psi_{n''p_-}(x) + \sum_{n'} \frac{\mu_{n'n''}}{2} A(x)\psi_{n's}(x) \\
E\psi_{ns}(x) &= -\frac{\partial_x^2}{2}\psi_{ns}(x) + \sum_{n'} \frac{\mu_{nn'}}{2} \left(A^*(x)\psi_{n'p_-}(x) - A(x)\psi_{n'p_+}(x)\right),
\end{aligned}$$

where the initial state $|ns\rangle$ has been taken to have energy zero and $A(x)$ represents the position space coupling function

$$A(x) = \frac{x + iY}{(x^2 + Y^2)^{\frac{3}{2}}}.$$

The first two equations may be simplified using the fact that the only s -state in the basis is that with principal quantum number n when using the single transition approximation. Therefore, n' in the first two equations may be replaced with n . Converting to the basis $|k, n'\alpha\rangle$, which diagonalises $H_A + H_E$, corresponds to making the substitution

$$\psi_{n'\alpha}(x) = \sum_k C_{k,n'\alpha} \frac{e^{ikx}}{\sqrt{L}}$$

of discrete coefficients in the momentum space plane wave basis, yielding

$$\begin{aligned}
E \sum_k C_{k,n'p_+} \frac{e^{ikx}}{\sqrt{L}} &= \left(-\frac{\partial_x^2}{2} + \Delta\mathcal{E}_{n'p}\right) \sum_k C_{k,n'p_+} \frac{e^{ikx}}{\sqrt{L}} - \frac{\mu_{nn'}}{2} A^*(x) \sum_k C_{k,ns} \frac{e^{ikx}}{\sqrt{L}} \\
E \sum_k C_{k,n'p_-} \frac{e^{ikx}}{\sqrt{L}} &= \left(-\frac{\partial_x^2}{2} + \Delta\mathcal{E}_{n'p}\right) \sum_k C_{k,n'p_-} \frac{e^{ikx}}{\sqrt{L}} + \frac{\mu_{nn'}}{2} A(x) \sum_k C_{k,ns} \frac{e^{ikx}}{\sqrt{L}} \\
E \sum_k C_{k,ns} \frac{e^{ikx}}{\sqrt{L}} &= -\frac{\partial_x^2}{2} \sum_k C_{k,ns} \frac{e^{ikx}}{\sqrt{L}} + \sum_{n',k} \frac{\mu_{nn'}}{2} \left(A^*(x)C_{k,n'p_-} - A(x)C_{k,n'p_+}\right) \frac{e^{ikx}}{\sqrt{L}},
\end{aligned}$$

where n'' has been replaced by n' as the principal quantum number associated with the p -states. Multiplying these equations by $\int_{-L/2}^{L/2} dx e^{-ik'x}/\sqrt{L}$ and converting the sum over k into an integral (as explained in the introduction part of section 3.3) transforms these equations to

$$\begin{aligned} EC_{n'p_+}(k') &= \left(\frac{k'^2}{2} + \Delta\mathcal{E}_{n'p} \right) C_{n'p_+}(k') - \frac{\mu_{nn'}}{4\pi} \int dk \int dx A^*(x) e^{i(k-k')x} C_{ns}(k) \\ EC_{n'p_-}(k') &= \left(\frac{k'^2}{2} + \Delta\mathcal{E}_{n'p} \right) C_{n'p_-}(k') + \frac{\mu_{nn'}}{4\pi} \int dk \int dx A(x) e^{i(k-k')x} C_{ns}(k) \\ EC_{ns}(k') &= \frac{k'^2}{2} C_{ns}(k') + \frac{\mu_{nn'}}{4\pi} \int dk \int dx (A^*(x) C_{n'p_-}(k) - A(x) C_{n'p_+}(k)), \end{aligned}$$

where the wire has been taken to be infinite in length and so the momentum space coefficients have become continuous functions, and all integrals are over all space or momentum. The integrals over x are now carried out to finally yield

$$\begin{aligned} EC_{n'p_+}(k') &= \left(\frac{k'^2}{2} + \Delta\mathcal{E}_{n'p} \right) C_{n'p_+}(k') - \frac{i\mu_{nn'}}{2\pi} \int dk \mathcal{F}(k - k') C_{ns}(k) \\ EC_{n'p_-}(k') &= \left(\frac{k'^2}{2} + \Delta\mathcal{E}_{n'p} \right) C_{n'p_-}(k') + \frac{i\mu_{nn'}}{2\pi} \int dk \mathcal{G}(k - k') C_{ns}(k) \\ EC_{ns}(k') &= \frac{k'^2}{2} C_{ns}(k') + \frac{i\mu_{nn'}}{2\pi} \int dk \left(\mathcal{F}(k - k') C_{n'p_-}(k) - \mathcal{G}(k - k') C_{n'p_+}(k) \right), \end{aligned}$$

where the definitions of \mathcal{F} and \mathcal{G} are given in equations (3.9) and (3.10), respectively.

In order to find an analytic solution to these equations, it is important to know the form of the momentum space coupling functions \mathcal{F} and \mathcal{G} . These can be seen in Fig. 3.4, where it is clear that the peak value of $\mathcal{F}(k - k')$ is found at $(k - k') = -\delta_{\mathcal{F}\mathcal{G}}$ whereas that of $\mathcal{G}(k - k')$ is found at $(k - k') = \delta_{\mathcal{F}\mathcal{G}}$. It has not been possible to find an analytic expression for $\delta_{\mathcal{F}\mathcal{G}}$, though it is clear that it changes with the value of Y . The assumption is now made that the coefficients $C_{ns}(k')$, $C_{n'p_+}(k')$ and $C_{n'p_-}(k')$ vary very slowly over the width of

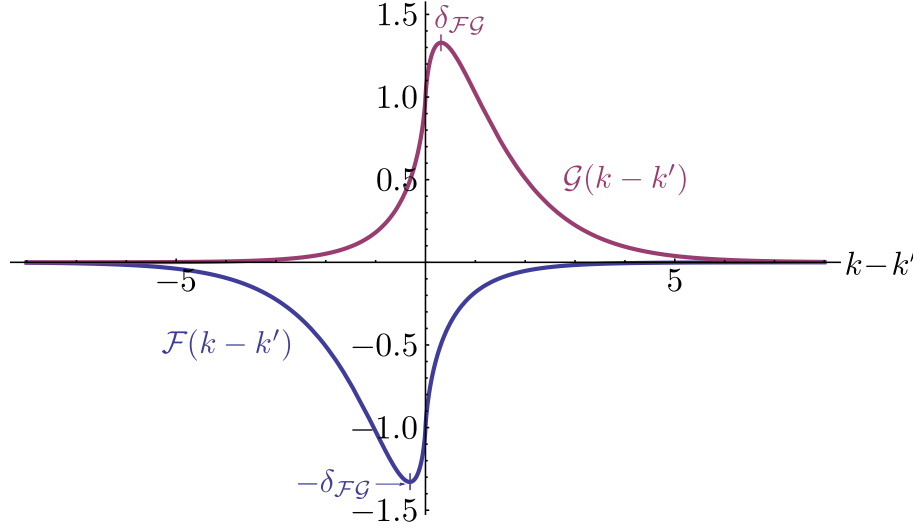


Figure 3.4: A plot showing the form of $\mathcal{F}(k - k')$ and $\mathcal{G}(k - k')$ whose peak values both occur at $|k - k'| = |\delta_{\mathcal{F}\mathcal{G}}|$. $Y = 1$ here for a clear scale. Atomic units are used here.

$\mathcal{F}(k - k')$ and $\mathcal{G}(k - k')$. The interpretation of such an approximation is that the $|k, ns\rangle$ state is only coupled to those states where the atom is in a p -state and the electron momentum varies by exactly $\pm\delta_{\mathcal{F}\mathcal{G}}$. The coupling functions are thus approximated as the value of their integral in momentum space multiplied by a delta function, written as

$$\begin{aligned}\mathcal{F}(k - k') &\approx -\frac{\pi}{Y^2}\delta[k - (k' - \delta_{\mathcal{F}\mathcal{G}})] \\ \mathcal{G}(k - k') &\approx \frac{\pi}{Y^2}\delta[k - (k' + \delta_{\mathcal{F}\mathcal{G}})]\end{aligned}$$

where $\delta[k]$ is the Dirac delta function. This leads to

$$\begin{aligned}EC_{n'p_+}(k' + \delta_{\mathcal{F}\mathcal{G}}) &\approx \left(\frac{(k' + \delta_{\mathcal{F}\mathcal{G}})^2}{2} + \Delta\mathcal{E}_{n'p}\right) C_{n'p_+}(k' + \delta_{\mathcal{F}\mathcal{G}}) + \frac{i\mu_{nn'}}{2Y^2}C_{ns}(k') \\ EC_{n'p_-}(k' - \delta_{\mathcal{F}\mathcal{G}}) &\approx \left(\frac{(k' - \delta_{\mathcal{F}\mathcal{G}})^2}{2} + \Delta\mathcal{E}_{n'p}\right) C_{n'p_-}(k' - \delta_{\mathcal{F}\mathcal{G}}) + \frac{i\mu_{nn'}}{2Y^2}C_{ns}(k') \\ EC_{ns}(k') &\approx \frac{k'^2}{2}C_{ns}(k') - \frac{i\mu_{nn'}}{2Y^2}\left(C_{n'p_-}(k' - \delta_{\mathcal{F}\mathcal{G}}) + C_{n'p_+}(k' + \delta_{\mathcal{F}\mathcal{G}})\right)\end{aligned}$$

where the momentum has been shifted from the previous equation such that C_{ns}

is always described as having the momentum k' . Final simplifications to be made to this equation are the introduction of an effective detuning

$$\Delta_{k\pm} = \Delta\mathcal{E}_{n'p} + \frac{1}{2} [(k \pm \delta_{\mathcal{FG}})^2 - k^2]$$

and an effective coupling $\Omega_{\text{eff}} = \mu_{nn'}/(2Y^2)$, which allows the final form to be found as

$$\begin{aligned} EC_{n'p_+}(k' + \delta_{\mathcal{FG}}) &\approx \left(\Delta_{k_+} + \frac{k'^2}{2} \right) C_{n'p_+}(k' + \delta_{\mathcal{FG}}) + i\Omega_{\text{eff}}C_{ns}(k') \\ EC_{n'p_-}(k' - \delta_{\mathcal{FG}}) &\approx \left(\Delta_{k_-} + \frac{k'^2}{2} \right) C_{n'p_-}(k' - \delta_{\mathcal{FG}}) + i\Omega_{\text{eff}}C_{ns}(k') \\ EC_{ns}(k') &\approx \frac{k'^2}{2}C_{ns}(k') - i\Omega_{\text{eff}}\left(C_{n'p_-}(k' - \delta_{\mathcal{FG}}) + C_{n'p_+}(k' + \delta_{\mathcal{FG}}) \right). \end{aligned}$$

The points at which each detuning goes to zero ($\Delta_{k\pm} \rightarrow 0$) signify the points at which the coupling to the respective state is expected to be maximum. The results are intriguing, as the solution for the coupling to the state $|n'p_+\rangle$, k_+ , is found to be

$$k_+ = -\frac{\delta_{\mathcal{FG}}^2 + 2\Delta\mathcal{E}_{n'p}}{2\delta_{\mathcal{FG}}}$$

whereas that for the state $|n'p_-\rangle$, k_- , is

$$k_- = \frac{\delta_{\mathcal{FG}}^2 + 2\Delta\mathcal{E}_{n'p}}{2\delta_{\mathcal{FG}}}.$$

This shows that the incident direction of the electron effectively selects which magnetic sublevel is most likely populated.

This system of equations may be solved analytically to find the eigenenergies and eigenstates of the system. This is done using *Mathematica* and so the expressions are not easily presentable and are omitted here. A plot of how the eigenenergies vary with the momentum of the electron can be seen in Fig. 3.5,

where the basis has been limited to those states with the initial principal quantum

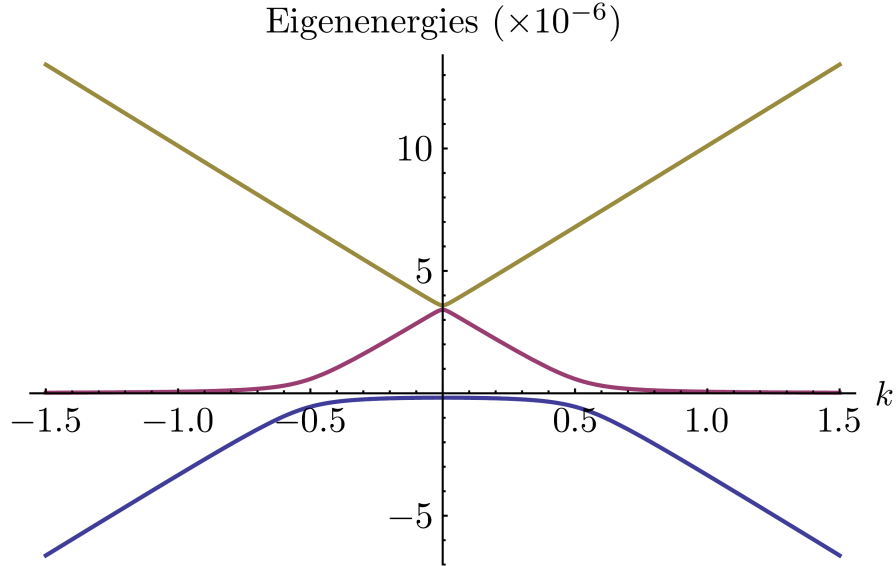


Figure 3.5: A plot showing how the energy eigenvalues of the system vary with the electron momentum k . The quadratic dispersion has been removed such that the avoided crossings are clearly seen. This is for a $|55s\rangle$ rubidium atom trapped $Y = 2.5\mu\text{m}$ from the electron wire. Both the momentum and energies are in atomic units.

number and the quadratic dispersion relation of the electron removed. The plot shows avoided crossings (rather than divergences) around k_{\pm} plus a third one at $k = 0$. This indicates that atomic state mixing occurs around these points. The third avoided crossing at $k = 0$ is also easily accounted for as both the p -states have the same energy. Another point which can be gained from this analysis is a measure of the strength of the coupling, which is calculated as the separation of the energy levels at their closest point. For this system the strength of the coupling is found to be $2\Omega_{\text{eff}} = \mu_{nn'}/Y^2$.

So far, it has been assumed that the fine structure splitting of the p -states may be neglected as the electron couples the two fine structure states equally. This figure for the coupling strength may be used to evaluate this approximation. Clearly a real atom has fine structuring of its atomic levels brought about by

spin-orbit coupling. The spin-orbit interaction leads to an increase in the energy level of the p -states if the spin of the valence electron is $m_s = 1/2$, whereas it leads to a reduction in their energy if the valence electron has spin $m_s = -1/2$. The energies of each p -state shift by the same amount for a given spin of the valence electron, which is due to the coupling of the electron spin coupling to the orbital angular momentum l .

In order for the fine structure of the atom to be neglected, i.e. the coupling is to that of the two fine structure states equally, it must be the case that the coupling must be large compared to the energy spacing between the states. As previously shown, the coupling between the s - and p -states is approximately $2\Omega_{\text{eff}}$. The fine structure splitting is found using the *corrected* result quoted in [164],

$$\nu_{\text{fs}} = (86935.7(7)(n^*)^{-3} - 233.5(5)(n^*)^{-5}) \text{ GHz}$$

which reproduces the results given in [165]. Here n^* is the *effective* principal quantum number, defined as $n^* = n - \delta_{n,l,j}$, where $\delta_{n,l,j}$ is the quantum defect of the atomic species. The simple inequality which governs when the fine structure may be neglected is thus given as $2\Omega_{\text{eff}} \gg \nu_{\text{fs}}$. Using the expression previously quoted for Ω_{eff} , the condition upon the initial principal quantum number for rubidium may be shown to be $n \gtrsim 33$.

This analysis has shown that there are specific values of electron momentum for which the coupling to the atom changes its dispersion relation. Qualitatively this signifies that at these points the electron and atom form a composite quantum system, where a measurement of electron momentum could allow the state of the atom to be inferred. Unfortunately, a numerical approach of the same form of that which was successful for the bound states fails in the case of unbounded states. Such a problem was encountered in a similar approach detailed in [166], and is due to the fact that there are a continuum of possible states into which the system

may be scattered. It is therefore troublesome to evaluate the approximation that the coupling function is narrow compared to the scale on which the state coefficients change. At this point this analysis is abandoned in favour of two further analytical techniques, both of which are capable of predicting the final state of the atom for a given momentum of the electron. What will become clear is that both of the following procedures corroborate the prediction that incident direction selects the preferred atomic magnetic sublevel.

3.4 Analytic Analysis

The aim of this work is to calculate how an electron travelling with a given initial momentum k_i can change the internal state of the atom. This section provides the details of two analytical approaches, solution of the time-dependent Schrödinger equation and a solution of the Lippmann-Schwinger scattering equation, which are aimed at achieving this goal in the weak coupling limit. It will become clear that the results of these two methods support each other, while both confirming properties predicted in the preliminary investigation.

3.4.1 Time-Dependent Schrödinger Equation

The first approach detailed is not only analytically solvable under certain conditions but will go on to form the basis of a numerical exploration of the system, detailed in section 3.5. Here the solution of the time dependent Schrödinger equation is detailed, the implications of which are represented once the result is confirmed by the Lippmann-Schwinger scattering method. Taking the full Hamiltonian of the system H , the Schrödinger equation governing the dynamics of the

system may be written as

$$i\partial_t\psi(x, t) = H\psi(x, t),$$

where $\psi(x, t)$ represents the composite wavefunction of the system. This function can be written as

$$\psi(x, t) = f(x, t)e^{ikx},$$

where $f(x, t)$ is a spinor containing the envelope function corresponding to each atomic state for the plane wave with momentum k . Upon application of the system Hamiltonian, the Schrödinger equation becomes

$$i\partial_t f(x, t) = -\frac{1}{2}\partial_x^2 f(x, t) - ik\partial_x f(x, t) + \left[V(x) + \frac{k^2}{2} \right] f(x, t),$$

in which the plane wave is a common factor to both sides, so has been removed, and $V(x) = H_A + H_{\text{int}}$ with H_{int} as given in (3.6), such that the approximation $Y \gg |\vec{r}|$ is taken. The appearance of $k^2/2$ in the final term of the expression may be neglected as it merely describes a universal shift of the system energies, not depending on either x or t . The first term describes the dispersion of the electron wavepacket, which may be neglected under certain conditions. Assuming that the envelope function varies slowly with x , i.e. $|\partial_x^2 f| \ll |k\partial_x f|$, the highest order derivative in the previous expression may be neglected. This is the slowly varying envelope approximation [167]. With the spreading term thus neglected, the equation is finally written as

$$i\partial_t f(x, t) = -ik\partial_x f(x, t) + V(x)f(x, t). \quad (3.12)$$

It is now possible to move to a frame of reference where the electron is at rest, which is achieved by means of the unitary transformation $U = e^{-kt\partial_x}$. Upon

application of this transformation, the Schrödinger equation becomes

$$i\partial_t g(x, t) = U^\dagger V(x) U g(x, t),$$

where $g(x, t) = U^\dagger f(x, t)$. Using the fact that $\partial_x^\dagger = -\partial_x$, the Baker-Campbell-Hausdorff formula [168] is used to work out how $V(x)$ is written in this frame.

The result is

$$U^\dagger V(x) U = V(x) + kt\partial_x V(x) + \frac{1}{2}k^2 t^2 \partial_x^2 V(x) + \dots$$

which one recognises a Taylor expansion of the potential $V(x + kt)$. The problem has thus been reduced to that of a stationary electron subject to a time dependent potential,

$$i\partial_t g(x, t) = V(x + kt)g(x, t). \quad (3.13)$$

To further simplify this problem, contrary to the Lippmann-Schwinger approach (to be detailed in section 3.4.2), the assumption is made that the state change of the atom does not change the momentum distribution of the electron. This is equivalent to stating that the energy equivalent of the variance in momentum space of the electron wavepacket is much greater than the atomic state energy difference $\Delta\mathcal{E}_{n'n} = \mathcal{E}_{n'} - \mathcal{E}_n$. Thus the electron is insensitive to momentum changes $\sim \sqrt{2\mathcal{E}_{n'n}}$ and so there is no back-action caused by the changes it induces in the atomic state. This condition means that the state of the electron is the same regardless of the state of the atom, allowing the separation

$$g(x, t) = \vartheta(x)\varphi(t)$$

to be made, where $\vartheta(x)$ describes the time-independent shape of the electron wavepacket and $\varphi(t)$ describes the position-independent state of the atom. The

electronic degree of freedom may now be traced out, leaving an equation for the time evolution of the atomic state. This is performed as a multiplication by $\vartheta^*(x)$ and an integral over position, yielding

$$i\partial_t\varphi(t) = \int dx \rho(x)V(x+kt)\varphi(t),$$

where $\rho(x) = |\vartheta(x)|^2$ such that $\int dx \rho(x) = 1$ for any normalised electronic wavepacket. A final simplification to this equation is the assumption that the trapping distance, Y , is much greater than the spatial width of the wavepacket, Δx . This allows the electron to be treated as a point charge and the substitution $\rho(x) \approx \delta[x]$ to be made, where the atom is assumed to be trapped at $x = 0$. The equation governing the dynamics of the atomic part of the system may thus be written as

$$i\partial_t\varphi(t) = V(kt)\varphi(t), \quad (3.14)$$

and forms the basis of an analytical expression for the first order transition amplitudes in the weak coupling limit, explained in the following subsection.

The Weak Coupling Regime

The weak coupling regime is that where it can be assumed that the atom will only undergo a single state transition. Once again, this means that the only possible final states of the atom are $|ns\rangle$ and $|n'p_{\pm}\rangle$. The interaction Hamiltonian (3.7), where kt takes the place of x , therefore replaces $V(kt)$ in (3.14). The atomic spinor may be written for the coupling to a single n' manifold as

$$\varphi(t) = \begin{pmatrix} C_{n'p_+}(t) \\ C_{n'p_-}(t) \\ C_{ns}(t) \end{pmatrix},$$

with $C_{n'p_+}(t)$, $C_{n'p_-}(t)$ and $C_{ns}(t)$ representing the coefficients of the atomic states $|n'p_+\rangle$, $|n'p_-\rangle$ and $|ns\rangle$ at time t , respectively. This allows the Schrödinger equation for an electron travelling with momentum k_i to be written as

$$i\partial_t\varphi(t) = \begin{pmatrix} \Delta\mathcal{E}_{n'p} & 0 & -\frac{\mu_{nn'}}{2Y^2} \frac{k_it/Y-i}{[(k_it/Y)^2+1]^{\frac{3}{2}}} \\ 0 & \Delta\mathcal{E}_{n'p} & +\frac{\mu_{nn'}}{2Y^2} \frac{k_it/Y+i}{[(k_it/Y)^2+1]^{\frac{3}{2}}} \\ -\frac{\mu_{nn'}}{2Y^2} \frac{k_it/Y+i}{[(k_it/Y)^2+1]^{\frac{3}{2}}} & +\frac{\mu_{nn'}}{2Y^2} \frac{k_it/Y-i}{[(k_it/Y)^2+1]^{\frac{3}{2}}} & 0 \end{pmatrix} \varphi(t),$$

where a common factor of Y has been extracted from the position space coupling functions. This equation is now written in terms of the unitless momentum $\kappa = k_i/(Y|\Delta\mathcal{E}_{n'p}|)$ and time $\tau = |\Delta\mathcal{E}_{n'p}|t$,

$$i\partial_\tau\varphi(\tau) = \begin{pmatrix} \lambda_{n'} & 0 & -\eta_{nn'}\mathfrak{F}(\tau) \\ 0 & \lambda_{n'} & +\eta_{nn'}\mathfrak{F}^*(\tau) \\ -\eta_{nn'}\mathfrak{F}^*(\tau) & +\eta_{nn'}\mathfrak{F}(\tau) & 0 \end{pmatrix} \varphi(\tau), \quad (3.15)$$

where

$$\mathfrak{F}(\tau) = \frac{\kappa\tau - i}{[(\kappa\tau)^2 + 1]^{\frac{3}{2}}}$$

is the position space coupling function,

$$\eta_{nn'} = \frac{\mu_{nn'}}{2Y^2|\Delta\mathcal{E}_{n'p}|}$$

is a measure of the coupling strength and

$$\lambda_{n'} = \Delta\mathcal{E}_{n'p}/|\Delta\mathcal{E}_{n'p}|$$

is the sign of $\Delta\mathcal{E}_{n'p}$. The weak coupling regime is now clearly defined as the region where $\eta_{nn'} \ll 1$.

A set of coupled differential equations may be formed from (3.15),

$$\begin{aligned} i\dot{C}_{n'p_+} &= \lambda_{n'}C_{n'p_+}(\tau) - \eta_{nn'}\mathfrak{F}(\tau)C_{ns}(\tau) \\ i\dot{C}_{n'p_-} &= \lambda_{n'}C_{n'p_-}(\tau) + \eta_{nn'}\mathfrak{F}^*(\tau)C_{ns}(\tau) \\ i\dot{C}_{ns} &= \eta_{nn'}\mathfrak{F}(\tau)C_{n'p_-}(\tau) - \eta_{nn'}\mathfrak{F}^*(\tau)C_{n'p_+}(\tau), \end{aligned}$$

which may be solved approximately in the weak coupling limit using the knowledge that the atom is initially in the state $|ns\rangle$ and most likely remains there. This is equivalent to the assumption $C_{ns}(\tau) = 1$ such that the first two of the previous equations may be approximated as

$$\begin{aligned} i\dot{C}_{n'p_+} &= \lambda_{n'}C_{n'p_+}(\tau) - \eta_{nn'}\mathfrak{F}(\tau) \\ i\dot{C}_{n'p_-} &= \lambda_{n'}C_{n'p_-}(\tau) + \eta_{nn'}\mathfrak{F}^*(\tau). \end{aligned}$$

Using the knowledge that $C_{n'p_{\pm}}(-\infty) = 0$, the solutions of these equations are

$$\begin{aligned} C_{n'p_+}(\tau) &= i\eta_{nn'}e^{i\lambda_{n'}\tau} \int_{-\infty}^{\tau} \mathfrak{F}(\tau')e^{i\lambda_{n'}\tau'} \\ C_{n'p_-}(\tau) &= -i\eta_{nn'}e^{i\lambda_{n'}\tau} \int_{-\infty}^{\tau} \mathfrak{F}^*(\tau')e^{i\lambda_{n'}\tau'} \end{aligned}$$

respectively. The transition amplitude is found by taking the absolute value squared of these coefficients when $\tau \rightarrow \infty$, the result of which yields

$$\sigma_{n'p_{\pm}} = |C_{n'p_{\pm}}(\infty)|^2 = 4 \left| \frac{\eta_{nn'}}{\kappa^2} \right|^2 \left| \lambda_{n'} \frac{\kappa}{|\kappa|} K_0 \left(\frac{1}{|\kappa|} \right) \mp K_1 \left(\frac{1}{|\kappa|} \right) \right|^2. \quad (3.16)$$

Before detailing the implications of this result, a different derivation of it will be performed as a confirmation, which uses the Lippmann-Schwinger scattering equation and is detailed in the following section.

3.4.2 Scattering Solution

The second of the two approaches treats the changing state of the system as a scattering problem. As described in this section, this applies the Lippmann-Schwinger equation [169], which will be shown to replicate the expression for the transition amplitude (3.16) gained in the Schrödinger equation analysis. Due to conservation of energy, on the event that the atomic state changes it is expected that the kinetic energy of the electron changes accordingly, a situation which this method treats very well (demonstrated in [170]). This method therefore treats this as a scattering problem where the state of the scattering centre is changed during the interaction.

First of all a general overview of this powerful approach is provided, such that the reader has a template for the specific case to which it is subsequently applied. It is required that both the non-interacting and interacting systems share a continuous spectrum of eigenvalues, thus being written as

$$\hat{H}_0 |\phi\rangle = E |\phi\rangle \quad \text{and} \quad (\hat{H}_0 + \hat{V}) |\psi\rangle = E |\psi\rangle,$$

respectively. Assuming that this condition on the eigenvalues is satisfied, it must also be ensured that the eigenstates of the interacting system $|\psi\rangle$ reduce to those of the non-interacting system $|\phi\rangle$ as the interaction strength V is reduced to zero. The solution of this problem may be written

$$|\psi\rangle = |\phi\rangle + \frac{1}{E - \hat{H}_0} \hat{V} |\psi\rangle, \quad (3.17)$$

where an infinitesimal imaginary quantity may be added to the denominator of the second term in order to avoid divergences when operating on eigenstates of \hat{H}_0 . With this inclusion, this solution is the Lippmann-Schwinger equation and

may be written as

$$|\psi\rangle = |\phi\rangle + \hat{G}_0 \hat{V} |\psi\rangle, \quad (3.18)$$

where

$$\hat{G}_0 = \lim_{\varepsilon \rightarrow 0} \frac{1}{E - \hat{H}_0 + i\varepsilon}$$

is the Green's function or single particle propagator, which ensures that the scattered particle propagates away from the scattering centre [171]. Equation (3.18) is solved approximately using an iterative method to yield the Born series. The zeroth order approximation of this series is $|\psi\rangle = |\phi\rangle$, the first order approximation subsequently obtained when this is inserted into the right hand side of (3.18). Inserting the result of the previous iteration as $|\psi\rangle$ in (3.18) an infinite number of times yields the Born series

$$|\psi\rangle = \sum_{n=0}^{\infty} (\hat{G}_0 \hat{V})^n |\phi\rangle.$$

The *Born approximation* truncates this series at $n = 1$, yielding

$$|\psi\rangle = |\phi\rangle + \hat{G}_0 \hat{V} |\phi\rangle \quad (3.19)$$

and is valid when k is very large and/or the scattering is very weak, such that the scattered wave can be considered a plane wave. Using the Born approximation describes only first order scattering events, application of the next term in the Born series allows the description of second order scattering and so on. This current analysis focuses only on results gained using the Born approximation. The result found when truncating the series at $n = 2$ for this system is given in appendix F, where interpretations of each resulting term are provided.

This Lippmann-Schwinger scattering approach subject to the Born approximation may now be applied to the current system. For this to be valid it is

assumed that the channel which confines the electron is infinite in length, meaning that both the non-interacting and interacting systems will have the same eigenvalue spectrum provided by the continuum of possible electron kinetic energies. The non-interacting Hamiltonian in the general case may be identified here as $H_0 = H_A + H_E$ and thus the interaction $V = H_{\text{int}}$. The normalised initial state of the system, where the electron is far from the atom is

$$|\phi\rangle = \sqrt{\frac{L}{2\pi}} |k_i, n_s\rangle,$$

where L is the length of the confining electron wire and the identity in momentum space is as previously defined (Section 3.2). In order to find the wavefunction of the final state of the system $|\psi\rangle$ in the position basis, the Lippmann-Schwinger equation (3.19) is multiplied from the left by $\langle x|$ such that it may be written as

$$\langle x|\psi\rangle = \langle x|\phi\rangle + \langle x|G_0 H_{\text{int}}|\phi\rangle.$$

Evaluation of this expression requires inserting both the position basis electron Hilbert space identity, $\mathbb{I}_E = \int_{-\infty}^{\infty} dx |x\rangle \langle x|$, and a decomposed version of the atomic Hilbert space identity, $\mathbb{I}_A = \sum_{n,\beta} |n\beta\rangle \langle n\beta|$, twice. The result of this is written

$$\begin{aligned} \langle x|\psi\rangle = \langle x|\phi\rangle + \sum_{\substack{n',n'' \\ \beta',\beta''}} \int_{-\infty}^{\infty} dx' \int_{-\infty}^{\infty} dx'' \langle x|G_0|x',n'\beta'\rangle \\ \times \langle x',n'\beta'|H_{\text{int}}|x'',n''\beta''\rangle \langle x'',n''\beta''|\phi\rangle, \end{aligned} \quad (3.20)$$

where the Born approximation now provides a means to reduce the size of the Hilbert space. The first step towards such a reduction is the calculation of the overlap $\langle x'',n''\beta''|\phi\rangle$ using both the orthogonality of the atomic states and

$\langle x | k \rangle = \sqrt{1/L} e^{ikx}$. This reveals

$$\langle x'', n'' \beta'' | \phi \rangle = \frac{1}{\sqrt{2\pi}} e^{ik_i x''} \delta_{n'', n} \delta_{\beta'', s},$$

which allows the removal of the sums over β'' and n'' from (3.20), leaving

$$\langle x | \psi \rangle = \langle x | \phi \rangle + \sum_{n', \beta'} \int_{-\infty}^{\infty} dx' \int_{-\infty}^{\infty} dx'' \langle x | G_0 | x', n' \beta' \rangle \langle x', n' \beta' | H_{\text{int}} | x'', ns \rangle e^{ik_i x''}. \quad (3.21)$$

It has already been shown that only dipole transitions are allowed under the action of H_{int} and therefore once again the interaction Hamiltonian in the basis of only s and p states may be used (3.7).

Evaluation of the interaction Hamiltonian matrix element seen in (3.21) is now carried out, where $\hat{x} | x'' \rangle = x'' | x'' \rangle$ and $\langle x | x' \rangle = \delta[x - x']$ are used to reduce the full form of the Lippmann-Schwinger equation to

$$\begin{aligned} \langle x | \psi \rangle &= \langle x | \phi \rangle + \frac{1}{2\sqrt{2\pi}} \sum_{n', \beta'} \mu_{nn'} \int_{-\infty}^{\infty} dx' \langle x | G_0 | x', n' \beta' \rangle \\ &\times \left[\delta_{\beta', p-} \frac{x' + iY}{(x'^2 + Y^2)^{\frac{3}{2}}} - \delta_{\beta', p+} \frac{x' - iY}{(x'^2 + Y^2)^{\frac{3}{2}}} \right] e^{ik_i x'}, \end{aligned}$$

where the integral over x'' has also been evaluated. Here the procedure outlined in [172] for calculating matrix elements of the Green's function is detailed for the case of the system concerned. Applying a plane wave expansion the element instantly becomes

$$\langle x | G_0 | x', n' \beta' \rangle = \frac{L}{(2\pi)^2} \int_{-\infty}^{\infty} dk' \int_{-\infty}^{\infty} dk'' \langle k' | \frac{e^{i(k'x - k''x')}}{E_i - H_0 + i\varepsilon} | k'', n' \beta' \rangle,$$

where E_i has been inserted to signify the energy of the initial state. The fact that $|k'', n' \beta' \rangle$ is an eigenstate of H_0 with eigenenergy $E_{k'', n' \beta'} = \mathcal{E}_{n' \beta'} + k''^2/2$ can now be used along with the overlap of the momentum eigenstates, $\langle k | k' \rangle =$

$(2\pi)/L \times \delta[k - k']$, to reduce this expression to

$$\langle x | G_0 | x', n'\beta \rangle = \frac{1}{2\pi} \int_{-\infty}^{\infty} dk' \frac{e^{ik'(x-x')}}{E_i - \frac{k'^2}{2} - \mathcal{E}_{n'\beta'} + i\varepsilon} |n'\beta'\rangle.$$

The final form of this matrix element must therefore be found using contour integration, which starts by identifying the points at which the integrand diverges, $k' = \pm\gamma$, where in this case $\gamma = \sqrt{2E_i - 2\mathcal{E}_{n'\beta'} + 2i\varepsilon}$. The matrix element is thus re-written as

$$\langle x | G_0 | x', n'\beta \rangle = -\frac{1}{\pi} \int_{-\infty}^{\infty} dk' \frac{e^{ik'(x-x')}}{(k' - \gamma)(k' + \gamma)} |n'\beta'\rangle. \quad (3.22)$$

By definition, ε is an infinitesimal quantity, therefore a Taylor expansion of γ using this fact yields

$$\gamma = \sqrt{2E_i - 2\mathcal{E}_\beta + 2i\varepsilon} \approx \sqrt{2E_i - 2\mathcal{E}_\beta} + \frac{i\varepsilon}{\sqrt{2E_i - 2\mathcal{E}_\beta}} \approx \sqrt{2E_i - 2\mathcal{E}_\beta} + i\varepsilon,$$

within which the second step is a renormalisation of ε . Extension of k' into the complex plane, $k' = k'_R + ik'_I$, means that the exponential in the numerator of the matrix element becomes $e^{ik'_R(x-x')} e^{k'_I(x'-x)}$ allowing the contours to be identified. The probability of a scattering event occurring must approach zero as $|k'| \rightarrow \infty$, as in this limit the time for such an event becomes infinitesimal. Such a condition can be seen to rest on the imaginary part of k' . Considering $x > x'$ ($x < x'$), then $\langle x | G_0 | x', n'\beta \rangle \rightarrow 0$ for $k_I \rightarrow \infty$ ($k_I \rightarrow -\infty$) and thus we must close the contour on the upper (lower) half plane of the Argand diagram, thus encircling only the pole at $k' = \sqrt{2E_i - 2\varepsilon E_{n'\beta'}} + i\varepsilon$ ($k' = -\sqrt{2E_i - 2\varepsilon E_{n'\beta'}} - i\varepsilon$). The real part of the integral must be in the positive direction, and so for $x > x'$ ($x < x'$) this is achieved by an anti-clockwise (clockwise) contour. This integral may be evaluated using Cauchy's integral formula [173] and the Residue theorem [174],

which are combined to form

$$\oint_{\zeta} f(z) dz = 2\pi i \sum_{k=1}^N I(\zeta, a_k) \lim_{z \rightarrow a_k} (z - a_k) f(z),$$

where a_k is the k^{th} pole of the function $f(z)$, ζ is the contour to be integrated over and $I(\zeta, a_k)$ is the winding number of the contour about the pole, where the anti-clockwise contours are defined positive. Application of this theorem to the integral defined in (3.22) yields

$$\langle x | G_0^+ | x', n' \beta \rangle = - \frac{i e^{i \sqrt{2E_i - 2\mathcal{E}_{n'\beta'}}(x-x')}}{\sqrt{2E_i - 2\mathcal{E}_{n'\beta}}} |n' \beta'\rangle$$

and

$$\langle x | G_0^- | x', n' \beta \rangle = - \frac{i e^{-i \sqrt{2E_i - 2\mathcal{E}_{n'\beta'}}(x-x')}}{\sqrt{2E_i - 2\mathcal{E}_{n'\beta}}} |n' \beta'\rangle$$

for the positive and negative poles respectively. Knowing the regions where these two solutions are valid, $x > x'$ ($x < x'$) for the positive (negative) poles, a single expression for the matrix element may be expressed as

$$\langle x | G_0 | x', n' \beta \rangle = - \frac{i e^{i \sqrt{2E_i - 2\mathcal{E}_{n'\beta'}}|x-x'|}}{\sqrt{2E_i - 2\mathcal{E}_{n'\beta}}} |n' \beta'\rangle, \quad (3.23)$$

which ensures that the propagation of the particle after the scattering event is from x' to x , as is required for a physically viable result.

With the realisation that in (3.23), the condition $x > x'$ ($x < x'$) amounts to an electron scattered in the positive (negative) x -direction, it is important to note the direction in which it is initially travelling. With this in mind, the modification is made that the initial momentum is written as $\lambda |k_i|$, where $\lambda = \text{sign}(k_i)$ and $\lambda = +1(-1)$ signifies an electron initially moving in the positive (negative) x -direction. This makes it necessary that the reflection (transmission)

of the electron be included in the expression using the index $\sigma = -1$ ($\sigma = +1$). With these inclusions, the full expression of the Lippmann-Schwinger equation may be written

$$\begin{aligned} \langle x | \psi \rangle &= \langle x | \phi \rangle - \frac{i}{2\sqrt{2\pi}} \sum_{n', \beta'} \frac{\mu_{nn'} e^{i\lambda\sigma k_f x}}{k_f} \int_{-\infty}^{\infty} dx' e^{i\lambda(|k_i| - \sigma k_f)x'} \\ &\times \left[\delta_{\beta', p-} \frac{x' + iY}{(x'^2 + Y^2)^{\frac{3}{2}}} - \delta_{\beta', p+} \frac{x' - iY}{(x'^2 + Y^2)^{\frac{3}{2}}} \right], \end{aligned}$$

where $k_f = \sqrt{2E_i - 2\mathcal{E}_{n'\beta'}}$, whose physical interpretation will be explained shortly. The integral over x' thus amounts to a Fourier transform of the coupling in real space, leading to its momentum space equivalent. Such integrals have already been carried out in section 3.3, the change here being the argument of the exponential has changed to $i\lambda(|k_i| - \sigma k_f)x'$. These integrals just yield the twice the imaginary unit multiplied by the familiar \mathcal{F} and \mathcal{G} functions ((3.9) and (3.10)) with the argument $(k - k')$ replaced by $(\lambda(|k_i| - \sigma k_f))$. This completes the derivation of the scattered part of the equation.

The unscattered part of the equation (the simple $\langle x | \phi \rangle$) now using $|\phi\rangle = \sqrt{L/2\pi} |\lambda |k_i|, ns\rangle$ is straightforward to evaluate, yielding

$$\langle x | \phi \rangle = \frac{1}{\sqrt{2\pi}} \sum_{n', \beta'} e^{i\lambda|k_i|x} \delta_{n', n} \delta_{\beta', s} |n' \beta'\rangle,$$

which confirms that both the momentum of the electron and state of the atom remain unchanged. The final state of the system may thus be written as

$$\begin{aligned} \langle x | \psi \rangle &= \frac{1}{\sqrt{2\pi}} \sum_{\substack{n', \beta' \\ \lambda, \sigma = \pm 1}} \left[e^{i\lambda|k_i|x} \delta_{n', n} \delta_{\beta', s} + \mu_{nn'} \frac{e^{i(\lambda\sigma k_f)x}}{k_f} \left\{ \delta_{\beta', p-} \mathcal{G}(\lambda(|k_i| - \sigma k_f)) \right. \right. \\ &\quad \left. \left. - \delta_{\beta', p+} \mathcal{F}(\lambda(|k_i| - \sigma k_f)) \right\} \right] |n' \beta'\rangle, \end{aligned} \quad (3.24)$$

where the scattered part shows that the electron is left with momentum k_f if the state of the atom is changed as it passes by, which is easily shown to conserve energy. Using this equation, it is possible to find the probability that the atom will make a transition from the initial state to one of the p -states. This *transition amplitude* is calculated as the square of the scattering amplitude, which is the amplitude of the outgoing wave relative to the ingoing wave. The transition amplitude to any state $|n'p\rangle$ is thus written as

$$\sigma_{n'p} = \left| \frac{\langle x, n'p | \psi \rangle}{\langle x, ns | \phi \rangle} \right|^2.$$

Calculating the transition amplitudes to the p_+ - and p_- -states of the atom yields

$$\begin{aligned} \sigma_{n'p_{\pm}} = & \left| \frac{\mu_{nn'}}{k_f} \right|^2 \left| (\lambda(|k_i| - \sigma k_f)) K_0 [Y |\lambda(|k_i| - \sigma k_f)|] \right. \\ & \left. \mp |\lambda(|k_i| - \sigma k_f)| K_1 [Y |\lambda(|k_i| - \sigma k_f)|] \right|^2, \end{aligned} \quad (3.25)$$

where it is clear that the only difference between the amplitudes to the different magnetic states is the sign of one of the Bessel functions.

First of all, it is prudent to note that upon investigation of this result, the probability for a an electron to be reflected upon its interaction with the atom is nothing more than infinitesimal. This is most likely due to the fact that the Lippmann-Schwinger equation deals only with situations in which the momentum of the scattered particle is high, such that the potential is smooth on the scale of its associated wavelength. The index representing transmission and reflection, σ , is hereafter set such that the reflection is neglected.

There is one final approximation that can be made to (3.25), which will make it more general. The assumption $\Delta \mathcal{E}_{n'p} = \mathcal{E}_{n'p} - \mathcal{E}_{ns} \ll k_i^2$ is made such that a Taylor expansion of k_f yields $k_f \approx |k_i| - \Delta \mathcal{E}_{n'p} / |k_i|$ to first order. This is a clearly valid assumption, as when considering a $|55s\rangle$ rubidium atom the energy

gap $\Delta E_{55p} \approx 3.415 \times 10^{-6} E_h$ equates to an electron kinetic energy of a mere 0.09meV. Typical energies of the guided electrons described in [156] are 1 to 10 eV, but the authors describe a goal of reducing the lower limit of this range. Then using $\kappa = k_i/(Y\Delta|\mathcal{E}_{n'p}|)$ the expression can be written

$$\sigma_{n'p_{\pm}} \approx \left| \frac{\mu_{nn'}}{Y^2 \Delta \mathcal{E}_{n'p} \kappa^2} \right|^2 \left| \frac{\kappa}{|\kappa|} \frac{\Delta \mathcal{E}_{n'p}}{|\Delta \mathcal{E}_{n'p}|} K_0 \left(\frac{1}{|\kappa|} \right) \mp K_1 \left(\frac{1}{|\kappa|} \right) \right|^2, \quad (3.26)$$

which takes into account the two possible incident directions along with the fact that $\Delta \mathcal{E}_{n'p}$ can change sign for changing n' . This result then describes the final population of the $|n'p_{\pm}\rangle$ states. The prefactor is recognised as $4 \times \eta_{nn'}^2 \times 1/|\kappa|^4$, which remarkably makes the result exactly the same as that found using the Schrödinger equation method (3.16). The analytic results of these two very different yet complementary methods are briefly analysed in the following section.

3.4.3 Interpretation of the Transition Amplitude Result

This section briefly describes the results of the two analytic solutions of the system, which predicted the same result for the transition amplitude (3.26). This result predicts a decrease in transition amplitude with an increase in either the trapping distance or the energy difference between the states concerned. The expression also makes possible an estimate of the maximum transition amplitude, which is $\sim 5 \times \eta_{nn'}^2$ and occurs at $\kappa \approx \pm 0.7$. Taking the example of a $|55s\rangle$ rubidium atom trapped $2.5\mu\text{m}$ from the wire this will equate to an electron kinetic energy of $E_{\text{kin}} \approx 0.172\text{eV}$.

The results of this analysis are profound, as seen in Fig. 3.6 for the case of a $|55s\rangle$ rubidium atom. First the situation where the principal quantum number is conserved is considered, which can be seen in Fig. 3.6(a). The first point to note is that the direction of incidence of the free electron selects which of

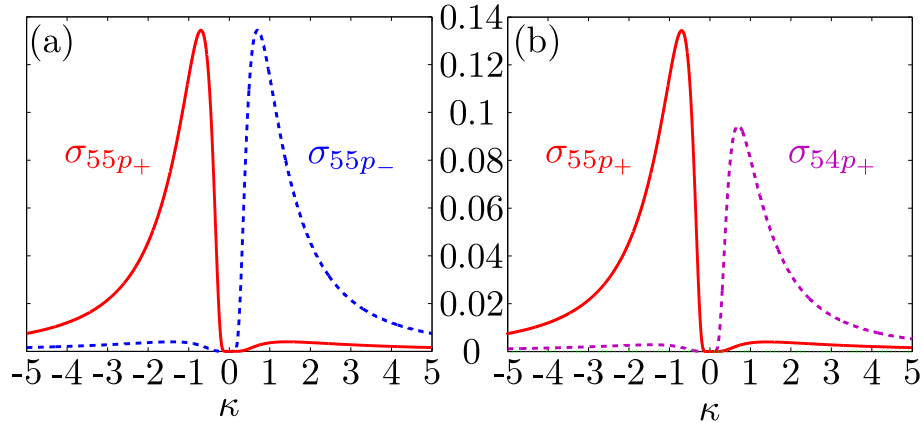


Figure 3.6: (a): Transition amplitudes for transitions from $|55s\rangle$ to both $|55p_+\rangle$ and $|55p_-\rangle$ as a function of the scaled momentum κ of the electron for a rubidium atom trapped $Y = 2.5\mu\text{m}$ from the electron wire. (b): Transition amplitudes for transitions $|55s\rangle$ to $|55p_+\rangle$ (solid/red), $|54p_+\rangle$ (dashed/purple) and $|56p_+\rangle$ (dotted/green).

the two magnetic sublevels are populated with higher probability. This remains qualitatively the same for other values of the initial principal quantum number and trapping distance Y . These results predict the possibility of selecting the magnetic state of the atom using only the direction of the incident electron, as was seen in the preliminary investigation in section 3.3.

The situation is not so clear when a change of principal quantum number of the atom is considered, which is illustrated in Fig. 3.6(b). Here, the results are given for a rubidium atom initially in the $|55s\rangle$ state for transitions to $|n'p_+\rangle$ states with $n' = n - 1$, n and $n + 1$. It then becomes clear that a change in principal quantum number defines the incident electron direction that makes the corresponding transition amplitude largest. The explanation of this phenomenon becomes clearer when investigating the form of the transition amplitude (3.26). In this expression, the sign of the K_0 component depends clearly on the sign of both the initial momentum and the sign of the energy difference between the two states. As this particular subset of Bessel functions are positive for all positive arguments, it is therefore the case that the transition amplitudes will be maximum

when the two Bessel functions included are of the same sign. For the p_+ -state illustrated in Fig. 3.6(b), this is therefore the case when k and $\Delta\mathcal{E}_{n'p}$ are of the opposite sign. Conversely, for the p_- -state, the maximum transition amplitude occurs when k and $\Delta\mathcal{E}_{n'p}$ are of the same sign.

It is clear that the shape of the transition amplitude is consistent whether considering a change of principal quantum number or not, and there appear to be three distinct regions. The first is the very low $|\kappa|$ region, where the transition probability remains zero. The reason for this is likely the fact that the interaction changes the atomic energy levels adiabatically, thus after the electron has passed there is very little chance of the atom having changed state. The intermediate region is that range of $|\kappa|$ around which the transition amplitude is maximum, which is the result of the energy levels being changed quickly enough that state changes may occur, but also for long enough that they actually have time to do so. The third region is the tail off of the transition amplitude occurring at high $|\kappa|$, which may be reasoned as the states being changed quickly enough to allow population changes, but the change of the levels happens for an increasingly short time as the momentum increases. Note that $\kappa = 0$ is not a case considered here and, whilst not clear in the figure, transition amplitudes for this zero momentum case are not given.

A final parameter which may be of interest experimentally is the total transition amplitude, which is calculated as the sum of all the possible single state transition amplitudes and is thus a measure of the probability that the atom undergoes a transition at all. The total transition amplitude is expressed as

$$\varsigma = 8 \sum_{n'} \eta_{nn'}^2 \left[K_0^2 \left(\frac{1}{|\kappa|} \right) + K_1^2 \left(\frac{1}{|\kappa|} \right) \right].$$

This shows that for momenta of the same magnitude but different direction, the total probability of a transition occurring is the same, but as previously shown the

magnetic sublevels contributing to the probability are different for the different directions.

The results presented here are only valid in the weak coupling limit, thus the following section details a numerical simulation of the system, which is capable of going beyond this limit.

3.5 Numerical Analysis

It is clear that to investigate beyond the weak coupling limit a numerical simulation of the system is required. A numerical simulation of the dynamics given by (3.14) for a real, multi-level atom is therefore carried out, with the electron treated as a point charge as previously described. These simulations use numerically generated wavefunctions for the atomic species and energy levels calculated using quantum defect theory. The aim of the simulation is to determine the state of the atom after the electron has reached a point where the interaction between the two systems has become negligible. This section will present a comprehensive analysis of the results for two different atomic species, rubidium and lithium, which have considerably different spectra (Fig. 3.7), and will then go on to present a brief comparison of the species.

In the following sections, the simulations are carried out using the details for atoms initially in the $|55s\rangle$ state, but in such a way that the results can be generalised to other initial principal quantum numbers. The scaled momentum $\kappa = k_i/(Y|\Delta\mathcal{E}_{np}|)$ is used such that for any value of n the species scalings of μ_n and $\Delta\mathcal{E}_{np}$ may be used to calculate the trapping distance Y required to generate $\eta_n \equiv \eta_{nn}$, which defines the coupling strength of the simulation.

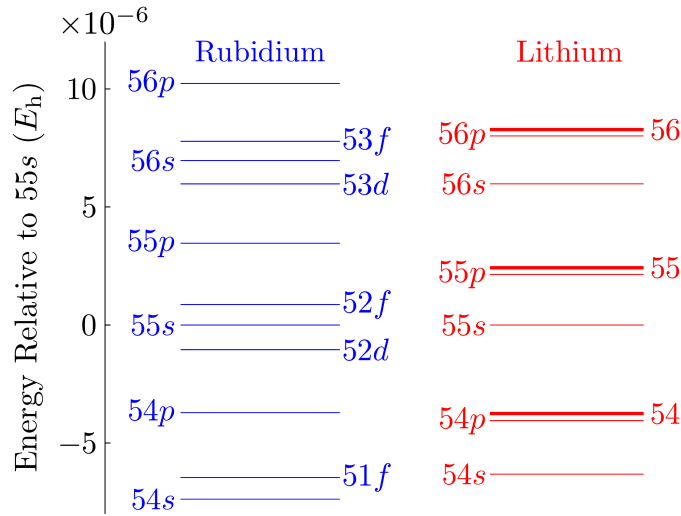


Figure 3.7: Comparison of the spectra of rubidium (blue) and lithium (red) around the $|55s\rangle$ state. The thick lines for lithium represent the energies of the states with $l > 2$, where those of $l > 3$ are degenerate.

3.5.1 Rubidium

Previously, the assumption was made that Y must be large enough that the electron may be considered a point like particle. Therefore, the value of η_n when the atom is trapped at a distance $Y = 10\langle r \rangle$ from the electron wire will be referred to as its *reference* value. Thus for a rubidium atom in the state $|55s\rangle$ trapped at this distance, the reference coupling value $\eta_{55}^{\text{Rb}} \approx 0.18$. An estimate of the highest attainable coupling strength at such a trapping distance is found to be $\eta_{125}^{\text{Rb}} \approx 0.5$, thus this will be the limit on the coupling strength set in the simulations.

In these simulations the electron will always travel to the right, starting at a distance of $15Y$ to the left of the atom where the results are presented once it has reached $40Y$ to the right of it. The extended region to the right accounts for the fact that the atom will have reached a higher angular momentum state during the interaction, and these more highly excited states are more easily coupled to each other.

Shown in Fig. 3.8 are the probabilities for the atom to remain in the initial state and undergo transitions of first, second or greater than second order, where

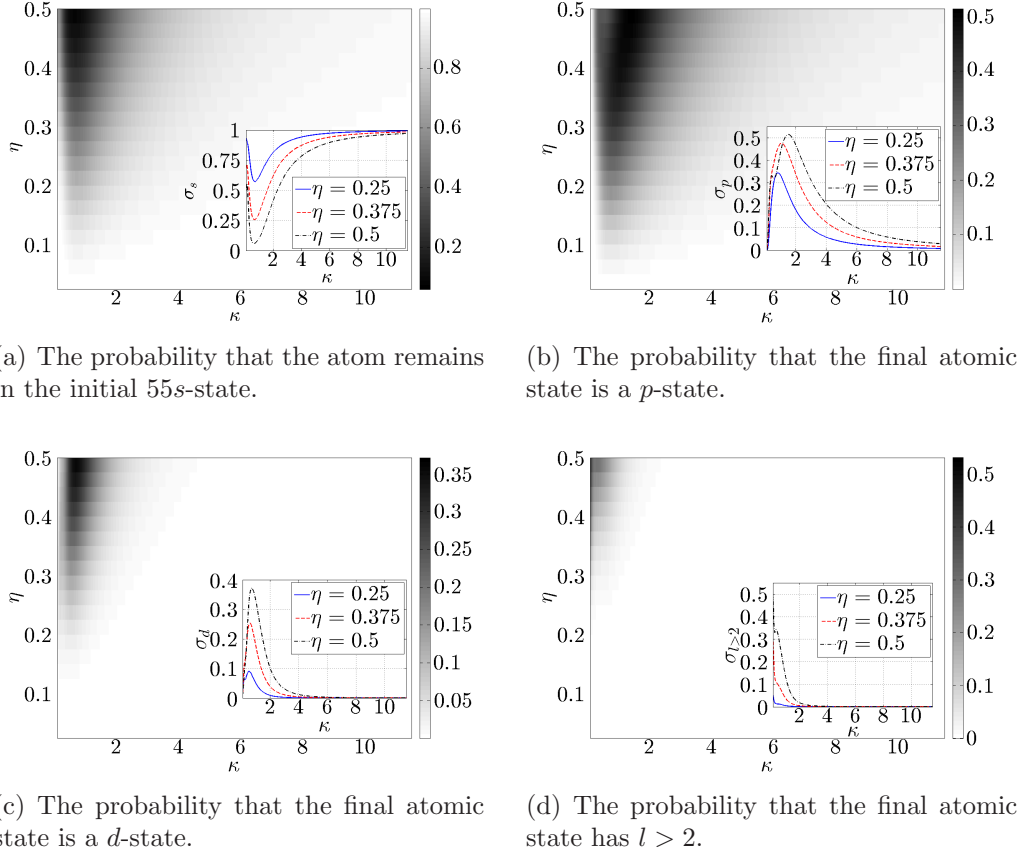


Figure 3.8: How the probabilities of the various states of the rubidium atom vary with η and κ . The insets show cross sections of $\eta = 0.25$, $\eta = 0.375$ and $\eta = 0.5$.

the insets show cross sections for fixed η and varying κ , with $\sigma_l = \sum_{n'} \sigma_{n'l}$. The first subfigure shows the probability of the atom remaining in the initial state, and shows the electron has to be moving very slowly and the system has to be set up such that $\eta > 0.1$ for there to be any significant population transfer. The second subfigure, Fig. 3.8(b), shows the probability that the atom has made a transition to any of the p -states in the system, thus meaning it has undergone a first order transition. The shape appears to mimic that of the void of initial state probability in Fig. 3.8(a), although the maximum transition amplitude here is only $\sigma_p \approx 0.5$, where the initial state probability actually falls to near zero.

The probability of the atom to be in any d -state is shown in Fig. 3.8(c), where the shape of the probability distribution for the d -states is very similar to that for the p -states but is restricted to higher η and lower κ , which is expected as more time is required for this second order transition and a higher coupling will make the transition faster. The overlap of these two regions thus suggests that the atom is likely to be found in a superposition state composed mostly of p - and d -states for a large proportion of the region where it is very unlikely to be found in its initial state. Shown in the final subfigure, Fig. 3.8(d), is the probability that the atom is found in some state other than an s -, p - or d -state. The region where these higher order transitions have occurred is quite clearly limited to the region where $\kappa < 2$ and $\eta > 0.3$ for reasons outlined previously. The maximum transition amplitude here is $\sigma_{l>d} \approx 0.5$, which shows that using a low momentum electron and choosing a setup to yield a high η value may create an atom whose valence electron is in a high angular momentum state.

It is possible to calculate the expectation values of the orbital angular momentum and magnetic quantum numbers of the final state of the atom. How far from their initial values of zero these expectation values are found to be may be taken as a measure of how effective the setup is at achieving atomic state manipulation. These expectation values are calculated from the final state of the atom using $\langle \psi_f | \hat{L}^2 | \psi_f \rangle = \langle L^2 \rangle = \langle l(l+1) \rangle$ and $\langle \psi_f | \hat{L}_z | \psi_f \rangle = \langle m \rangle$, where $|\psi_f\rangle$ is the final state of the atom which is a superposition of the free space atomic states. The expectation value of the orbital angular momentum quantum number will therefore be estimated as $\sqrt{\langle L^2 \rangle}$. These expectation values can be seen in Fig. 3.9, which is another way of illustrating that a higher coupling strength aids the transition from the initial s -state. The expectation value of the orbital angular momentum quantum number seen in Fig. 3.9(a), is clearly greater than zero for all values of κ for each of the three values of η illustrated. It also shows that

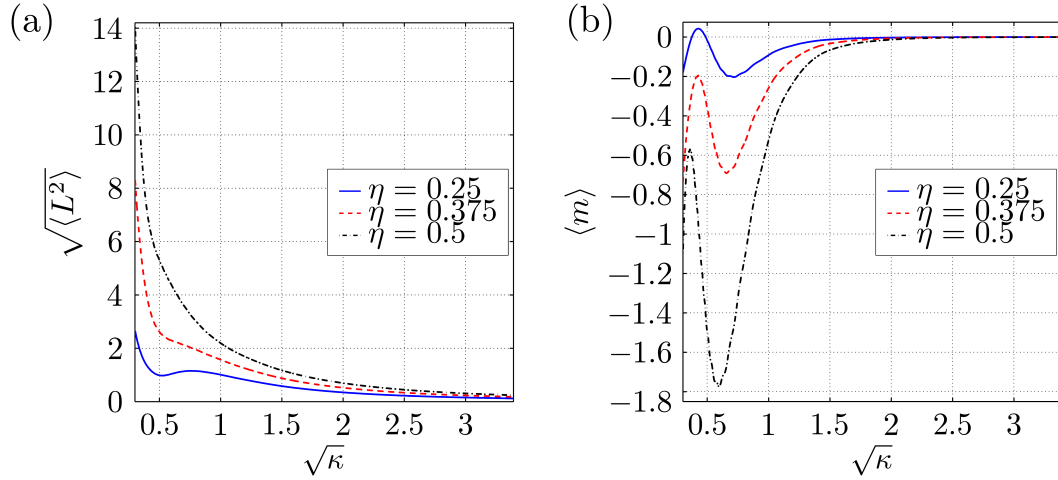


Figure 3.9: Plots showing the variation with κ of the expectation values of (a) the orbital angular momentum quantum number $\langle l \rangle \approx \sqrt{\langle L^2 \rangle}$ and (b) the magnetic quantum number $\langle m \rangle$ for three values of η .

the highest attainable values are found when $\kappa < 2$, with the value approaching zero as κ increases. Moving to Fig. 3.9(b), it is clear that $\langle m \rangle < 0$ for the majority of the κ range, which was expected from the analytics as the transition amplitude to the state $|np_- \rangle$, σ_{np_-} , tends to be the largest for this electron direction. The small region where $\langle m \rangle > 0$ is likely due to complicated dynamics where in the final state $n' > n$, such that the preferred transition is to a state whose average magnetic quantum number is positive. This figure also confirms that the preferred final state is the initial one as κ increases, as both $\sqrt{\langle L^2 \rangle}$ and $\langle m \rangle$ approach zero.

The polarisation of the atom after the passage of the electron may also be calculated, which will be a measure of whether the passage of the electron *switches* on a state of the atom which may act as a *permanent* dipole (for the lifetime of the final atomic state). The x - and y -direction polarisations of the atom will be quantified as $\langle x \rangle$ and $\langle y \rangle$ respectively. No polarisation is seen in the z -direction as there is no component of the electron-atom interaction Hamiltonian in this direction for this system geometry. Also, the magnetic quantum number is a measure

of the projection of the angular momentum of the valence electron onto the quantisation axis, which in this case is the z -axis, as shown in Fig. 3.1. Therefore, a relationship between the polarisations $\langle x \rangle$ and $\langle y \rangle$ and the expectation value $\langle m \rangle$ shown in Fig. 3.9 is not easily visualised. Shown in Fig. 3.10 are the direction and magnitude of the polarisation for selected values of κ when $\eta = 0.5$, where

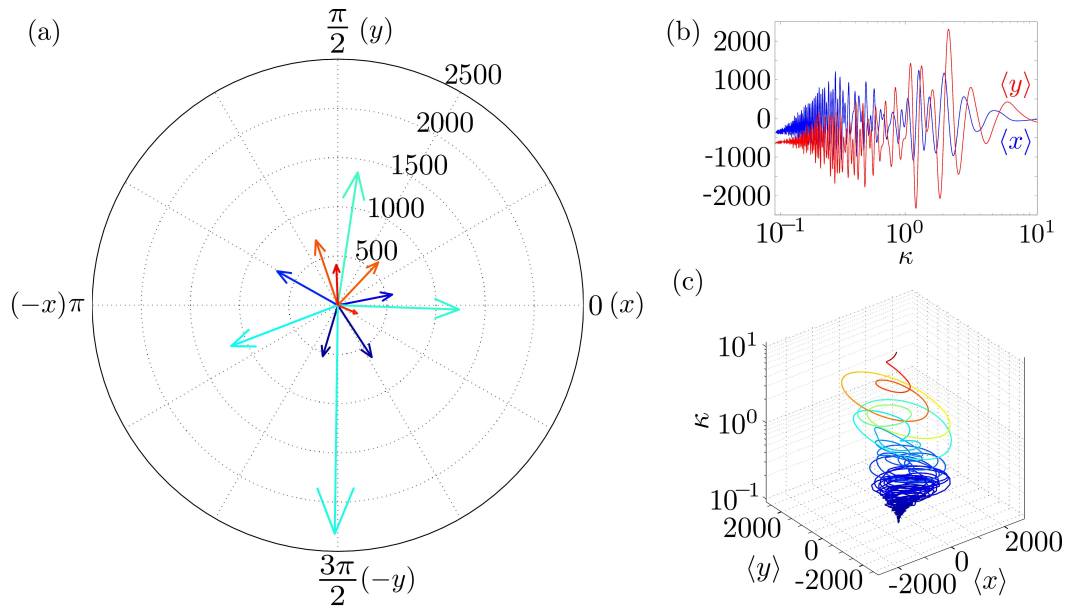


Figure 3.10: (a) Diagram showing the magnitude and direction of the polarisation for twelve selected κ values for $\eta = 0.5$. (b) Full profile of the same polarisation in $\langle x \rangle$ and $\langle y \rangle$ and (c) Three dimensional plot of the same data with a colour code corresponding to the values seen in (a).

an intriguing result is observed. Despite the atom being most likely found in a state with high angular and magnetic quantum numbers at low values of κ (see Fig. 3.9), the highest values of the polarisation are actually seen around $\kappa \approx 1$. This maximum polarisation is of the order of μ_n . What is also clear is that at their maximum values $\langle y \rangle > \langle x \rangle$, which accounts for the elliptical spiral seen in the inset showing the three-dimensional plot of how polarisation varies with κ .

This section has shown that the passage of an electron may be used to alter the state of a rubidium atom such that it is left with some degree of polarisation. The following section details a similar analysis applied to a lithium atom. This section

is followed by one which compares the two species and explores results found using parameters which may be realised with currently available experimental techniques.

3.5.2 Lithium

Referring once again to the reference value of the coupling as that where the atom is trapped at a distance $Y = 10 \langle r \rangle$ from the electron wire, it may be shown to be $\eta_{55}^{\text{Li}} \approx 0.36$ for a lithium atom initially in the state $|55s\rangle$. This reference limit may be increased to $\eta_{150}^{\text{Li}} \approx 1$ when the atom is initially in the state $|150s\rangle$, thus this will be the limit set in these calculations.

The orbital angular momentum states of lithium become degenerate when $l > 3$ [175] and are thus subject to the linear Stark effect [176]. Thus what appear to be well separated principal quantum number manifolds in the bare energy spectrum (Fig. 3.7) may become much closer when subject to an electric field [177]. This is useful when assessing how many principal quantum number manifolds need to be included in the simulation such that it converges. As the quantum defects of the degenerate states are zero, it is possible to analyse the effect of the electric field due to the electron by using the effect of an electric field on the states of a hydrogen atom [66]. In hydrogen, adjacent principal quantum number manifold energy levels cross at the Inglis-Teller limit of the electric field [178], which is given as $E_{\text{IT}} \approx 1/(3n^5)$. The strongest electric field experienced by the atom due to the electron is when they are closest to each other, i.e. when $x = 0$, and at this point is calculated as $1/Y^2$. Taking the reference value η_{55}^{Li} , the maximum experienced field for this set up is $E_{\text{el}} = 4.7 \times 10^{-10}$, which is slightly smaller than the Inglis-Teller field $E_{\text{IT}} = 6.6 \times 10^{-10}$, where both are in atomic units. Thus in the following analysis, which uses values for a lithium $|55s\rangle$ state, two lower and one higher principal quantum number manifolds were

taken, such that the problem converged.

Once again the simulations always describe an electron travelling to the right, where this time the electron travels the extended distance of $80Y$ to the right of the atom. This choice is made as an attempt to counteract the fact that lithium has many degenerate energy levels that will be coupled by any magnitude of electric field, and tests of the numerics showed that for the smallest value of Y chosen, the change of atomic levels at this extended distance is negligible. Shown in Fig. 3.11 are the probabilities for the lithium atom to remain in its initial state and undergo transitions of first, second and higher than second orders. The first

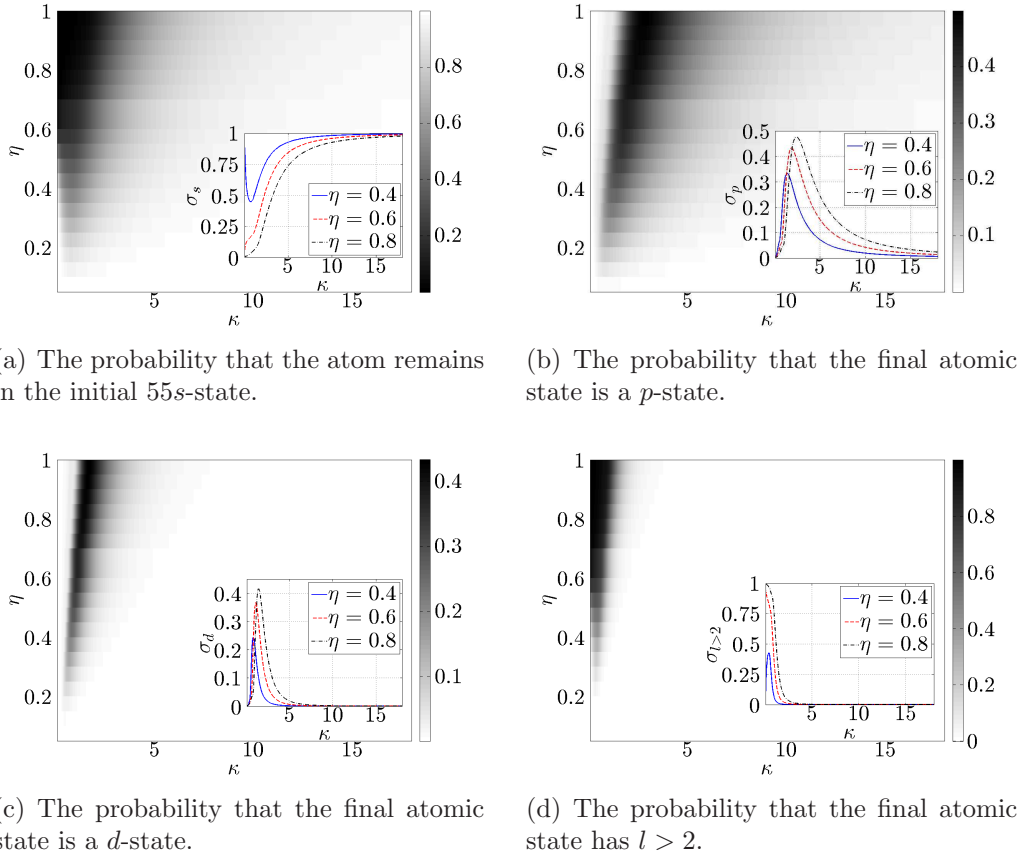


Figure 3.11: How the probabilities of the various states of the lithium atom vary with η and κ . The insets show cross sections of $\eta = 0.4$, $\eta = 0.6$ and $\eta = 0.8$.

subfigure, Fig. 3.11(a), shows the same trends as for the rubidium atom, where it appears that $\eta > 0.15$ before any transition is expected and then for high

values of the coupling the probability of finding the atom in the initial state may fall to zero. Looking at the very small κ region, subfigure 3.11(b) shows that for all η the smallest value of κ when p -states will be populated is consistently higher than in the case of rubidium. This is likely due to the fact that the $|np\rangle$ and $|nd\rangle$ states are considerably closer together in energy in lithium than they are in rubidium and thus the time required for a second order transition is much shorter. Therefore, in the case of lithium, the higher order transitions may occur at higher electron momentum. This trend is again the case for the transition amplitudes of the d -states, due to the fact that the f -state quantum defect in lithium is extremely small such that the d - and f -states are almost degenerate. The higher order transition times between these states are therefore very small. These observations are confirmed by what is seen in Fig. 3.11(d), where the transitions to states with $l > 2$ are limited to the region where $\kappa < 2$ and $\eta > 0.25$. Once again, it is high η setups and low momentum electrons which will yield the highest order transitions.

It is also informative to calculate the expectation values of orbital angular momentum and magnetic quantum numbers of the final state of the lithium atom, as was performed for rubidium. These are illustrated in Fig. 3.12, where it is clear that for certain setups it is possible to reach very highly excited states of the lithium atom. These states are populated by using a high coupling strength setup, as seen in Fig. 3.12(a), where even for relatively low coupling strength ($\eta = 0.4$) it is possible to achieve $\sqrt{\langle L^2 \rangle} > 5$ for low electron momentum. Once again the prediction that an electron travelling to the right will most likely populate states of the atom with $m < 0$ is confirmed in Fig. 3.12(b). Both figures combined confirm that as the electron momentum increases it is more likely that the atom does not change state.

The polarisation of the lithium atom after the passage of the atom has been

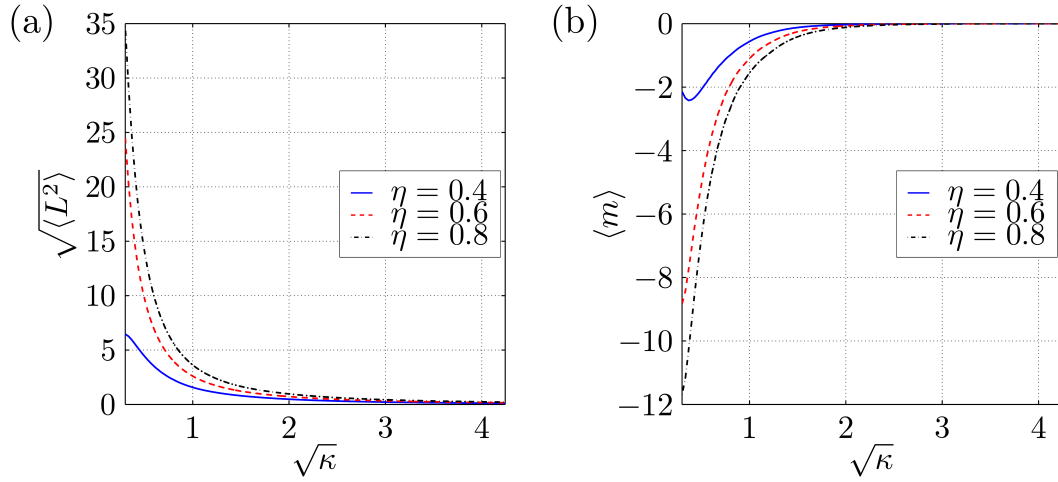


Figure 3.12: Plots showing the variation with κ of the expectation values of (a) the orbital angular momentum quantum number $\langle l \rangle \approx \sqrt{\langle L^2 \rangle}$ and (b) the magnetic quantum number $\langle m \rangle$ for three values of η .

calculated such that, as with rubidium, it is quantified using the expectation values $\langle x \rangle$ and $\langle y \rangle$ of the final atomic state. The polarisation for a setup where the coupling $\eta = 1$ can be seen in Fig. 3.13, where the arrows on the main part of the diagram show the magnitude and direction of the polarisation colour coded to coincide with the spiral representation of the full range inset. This result contrasts quite strikingly with that for rubidium in the fact that for low values of momentum the lithium atom shows clear positive x -polarisation and negative y -polarisation compared to the small negative x - and y -polarisations seen previously. The maximum values once again appear to be around the region $\kappa \approx 1$, beyond which they steadily approach zero, when the probability of the atomic state changing begins to become very small. Similar to the rubidium case, for the higher values of κ the polarisation takes an elliptical form as $\langle y \rangle > \langle x \rangle$, which is most likely due to the geometry of the system being the same in both cases.

This and the previous section have detailed how the numerical simulation was carried out for both lithium and rubidium, and it has been shown that

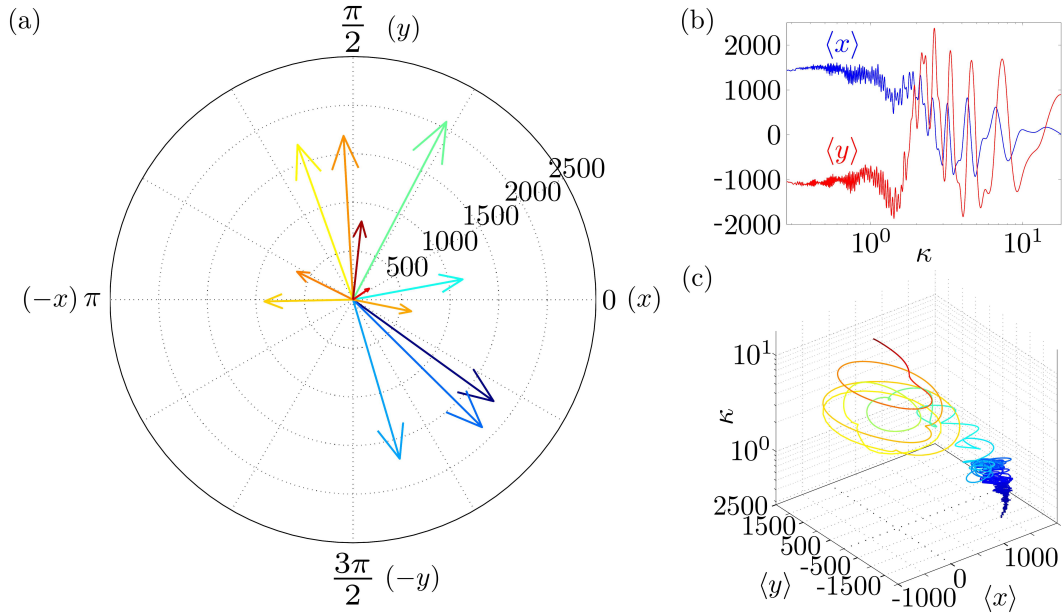


Figure 3.13: (a) Diagram showing the magnitude and direction of the polarisation for twelve selected κ values for $\eta = 1$. (b) Full profile of the same polarisation in $\langle x \rangle$ and $\langle y \rangle$ and (c) Three dimensional plot of the same data with a colour code corresponding to the values seen in (a).

the states which are most likely excited draw parallels to the analytics detailed in section 3.4. As previously noted, the results for both atomic species were achieved taking values of μ_n and $\Delta\mathcal{E}_{np}$ for an atom initially in the state $|55s\rangle$, varying the trapping distance to change η . Therefore, when values of η greater than the quoted reference values are used, the trapping distance $Y < 10 \langle r \rangle$ and the presented results should only be taken as a guide for using higher n atoms to achieve the same coupling. The following section directly compares results for rubidium and lithium with the trapping distance fixed at $Y = 10 \langle r \rangle$, and also compares the results directly with the low coupling regime analytics.

3.5.3 Species Comparison

This section focuses on the similarities and differences between the final states of the two atomic species, how the numerics compare to the analytics and the

implications these results have on experimental setups. Here, the atom will always be trapped at the distance $Y = 10 \langle r \rangle$ from the electron wire, and thus the coupling strengths will be those referred to as the reference values. The chosen initial states for rubidium are $|55s\rangle$, whose orbital radius $\langle r \rangle \approx 0.24\mu\text{m}$ gives the reference coupling value $\eta_{55} = 0.18$, and $|72s\rangle$, which has an orbital radius of $\langle r \rangle \approx 0.41\mu\text{m}$ and yields a reference coupling of $\eta_{72} = 0.25$. The chosen initial states for lithium are $|38s\rangle$, whose orbital radius $\langle r \rangle \approx 0.11\mu\text{m}$ gives the reference coupling value $\eta_{38} = 0.25$, and $|55s\rangle$ whose reference coupling is $\eta_{55} = 0.36$ (orbital radius being approximately the same as that for rubidium). The compositions of the final states for these chosen systems can be seen in Fig. 3.14, which clearly

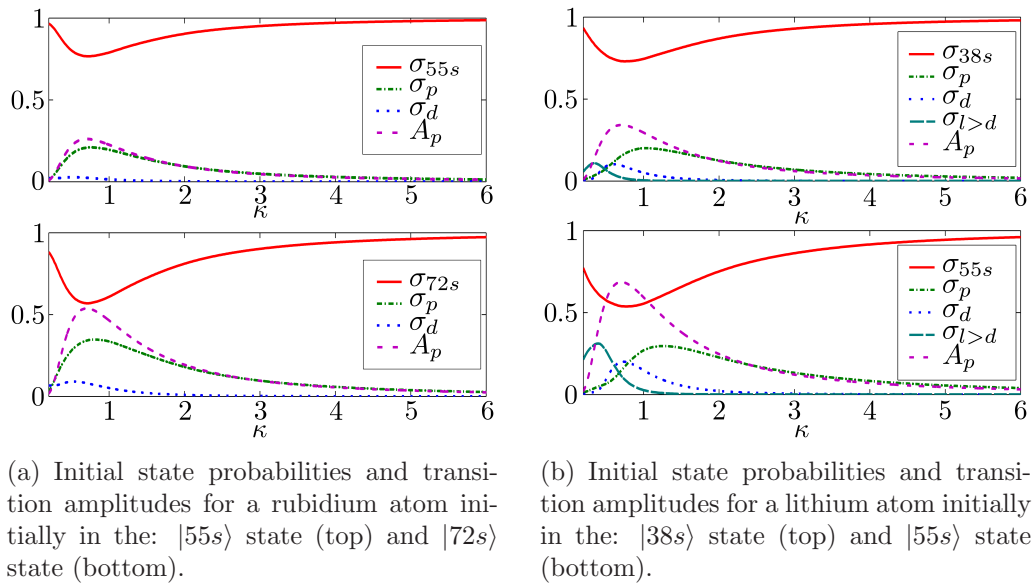


Figure 3.14: Initial state probabilities (σ_{ns}), transition amplitudes (σ_p , σ_d and $\sigma_{l>2}$) and analytic approximation of the p -state occupation (A_p) for two different states of: (a) A rubidium atom and (b) a lithium atom.

shows the results that have already been commented upon: the probability of the atom remaining in the initial state is lower for higher values of coupling and the lower values of κ are where the highest order transitions are likely to occur. These features are common to the four examples given here.

The result for rubidium, Fig. 3.14(a), shows good agreement with the analytic result (3.16) when the coupling is low and, as expected, breaks down when the coupling is increased. This is due to the fact that the analytic result only takes into account first order scattering events, not those of higher order that are present in the numerics, which also accounts for the fact that the analytics over-estimate σ_p in all cases. The numerical and analytic results do not show as strong an agreement in the case of lithium, seen in Fig. 3.14(b). It is clear in both cases that A_p is significantly greater than the numerical value, while the peak value occurs at a lower κ . To account for the varying success of the analytic approximation, one refers back to the differences between the atomic spectra of these two species, Fig. 3.7. The analytic results take into account only the initial s -state of the atom and the neighbouring p -states. The spectrum of rubidium shows that the smallest energy differences between the p - and d -states are of the order of those between the closest s - and p -states, thus this is a good approximation. In contrast, the principal quantum number manifolds of lithium are well separated, with the p -states being very close in energy to the higher l -states, which make higher order transitions in lithium much more likely than in rubidium, as can be seen in Fig. 3.14(b). Transitions higher than second order in rubidium are omitted from Fig. 3.14(a), as they have very small transition amplitudes.

Specific examples are now given of the transition probabilities for different values of the kinetic energy. In each set up, the minimum probability for the atom to be found in its initial state consistently occurs at a very low momentum. For example, a rubidium atom with initial state $|55s\rangle$ has a minimum initial state probability of $\sigma_{55s} = 0.73$ occurring at an electron kinetic energy of 0.18eV, the highest energy of the four configurations considered here. Taking this into consideration, provided here are kinetic energy values for each setup considered which fall within an achievable range with existing *electron waveguide* technology

[156] and yield $0.8 \leq \sigma_{ns} \leq 0.9$. For a $|55s\rangle$ rubidium atom this energy range is $0.39 \leq E_{\text{kin}} \leq 1.28\text{eV}$, which rises slightly to $0.65 \leq E_{\text{kin}} \leq 1.55\text{eV}$ for an initial $|72s\rangle$ state. The ranges and values are slightly greater when looking at the lithium atom cases: a $|38s\rangle$ initial state yields the kinetic energy range $0.54 \leq E_{\text{kin}} \leq 1.56\text{eV}$, which again rises slightly to $0.74 \leq E_{\text{kin}} \leq 1.56\text{eV}$ for an initial $|55s\rangle$ state. For all four cases the population in the p -state ranges from $\sigma_p \approx 0.18$ at the low end of this energy range to 0.1 at the high end.

In the previous sections it was shown that the atom will be left in a polarised state after the passage of the electron. A direct comparison of these four chosen setups is now given, illustrated in Fig. 3.15. In the case of rubidium, the po-

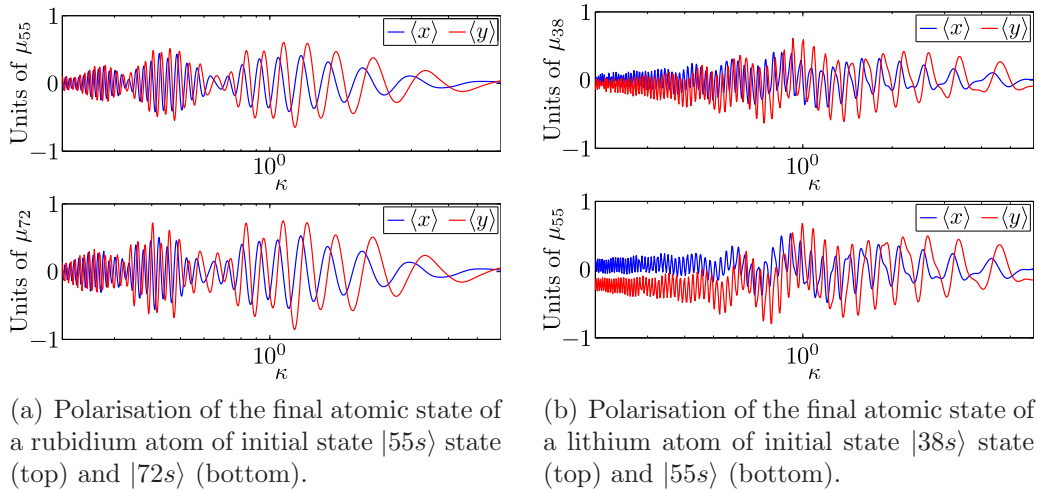


Figure 3.15: Polarisations of the final state of the atom for (a) rubidium and (b) lithium for varying κ .

larisation looks very similar for both initial states. For the entire range of κ it appears that both the $\langle x \rangle$ and $\langle y \rangle$ oscillations are centred around zero, having an overall envelope function determining their maximum value. The maximum value of $\langle x \rangle$ is approximately $2\mu_n^{\text{Rb}}/5$ and is first obtained at a value $\kappa \approx 0.45$, being obtained once more in the higher κ maximum of the envelope function. The case is slightly different for $\langle y \rangle$, whose maximum value is approximately $3\mu_n^{\text{Rb}}/5$ obtained at $\kappa \approx 1.1$. For the higher values of κ the polarisation approaches zero,

as the atomic state is very unlikely to change in the high momentum limit. The fact that these results are qualitatively the same for varying η_n implies that both chosen values are still in the weak coupling regime, which is not the case for those previously provided in Fig. 3.10.

Clearly the final polarisation of the lithium atom, 3.15(b), is different to that of the rubidium atom. In this case the distribution is also rapidly oscillating, though these oscillations show a smaller and more consistent amplitude than those for rubidium and the values around which they oscillate also vary as a function of κ . As was the case in rubidium, the rapid oscillations also reduce in frequency for increasing κ , but their amplitude increases very little in the intermediate κ region and is also slower in reducing to zero as κ increases further. For low κ , the mean value of the oscillations is small and positive for $\langle x \rangle$ and slightly larger but negative for $\langle y \rangle$. This separation increases with η_n as can be seen in Fig. 3.13, which is well outside the weak coupling regime, as is illustrated for the higher κ region.

3.5.4 Comparison with Previous Work

The unique feature of the work detailed here is the fact that the electron is confined to move along a set path where only its momentum is allowed to vary. Therefore it is very difficult to provide accurate comparisons with previous work. For instance, the work reviewed in [66] is concerned with the case where the free electron has an impact parameter smaller than the radius of the valence electron, such that the state of the atom may be changed along with both the momentum and direction of the electron. The quantum analysis considered in [152] presents results that are the most closely related to those detailed in the previous sections, as it considers only very low energy electrons. Although this study is concerned with direct collisions between the electron and a sodium atom, which

introduces the possibility of atomic ionisation, it also considers those collisions that change state of the atom. Though the results presented are for sodium, they are qualitatively similar to those given here in the fact that the final principal quantum number of the atom is most likely the initial one n along with $n - 1$, $n - 2$ or $n + 1$ with energy conservation also being observed. Hopefully the work presented here will stimulate further studies concerned with the electron having a fixed trajectory, which may be used to enhance these results.

This section has thoroughly detailed the numerical investigation of the system for both lithium and rubidium atoms trapped close to the electron wire. Before providing an analytic description of a multiple trapped atom system, a brief description is given which validates that the lifetime of the initial state is great enough that it will not decay during the passage of the electron.

3.5.5 Lifetime Considerations

It must be ensured that the internal atomic dynamics take place on a timescale much shorter than the lifetimes of the initial atomic state, such that the chance of an atomic state decaying during the interaction is negligible. The electron travels a distance of $d \times Y$ during the simulation, where $d = 55$ for rubidium and $d = 95$ for lithium, and the time it takes to traverse this distance is calculated as $t_E = dY/v_E$, where v_E is the speed of the electron. In atomic units $v_E \equiv k$ and thus $v_E = \kappa Y \Delta \mathcal{E}_{np}$ in the scaled units used here. The condition which must be satisfied is thus

$$\kappa \gg \frac{d}{\Delta \mathcal{E}_{np} t_A},$$

where t_A is the lifetime of the initial state, where values quoted are from [163].

Focusing first on rubidium, an analysis is given of the system that was used to give the results detailed in section 3.5.1, which used an atom initially in the state $|55s\rangle$ and varied Y to generate a wide range of η . Using $\Delta \mathcal{E}_{np}$ calculated

using quantum defect theory, $d_{\text{Rb}} = 55$ and $t_{\text{A}}^{\text{Rb}} \approx 191\mu\text{s}$, the inequality yields $\kappa \gg 2 \times 10^{-6}$, approximately four orders of magnitude smaller than that used in the simulation. It is thus the case that the atomic lifetime is much greater than the simulation time in the results presented for rubidium. Moving on to lithium, once again the results given for varying η , section 3.5.2, use the state $|55s\rangle$ and varying Y . These simulations use a slightly greater $d_{\text{Li}} = 95$, which when inserting the lifetime $t_{\text{A}}^{\text{Li}} = 133.6\mu\text{s}$ yields the slightly larger $\kappa \gg 8.1 \times 10^{-6}$, still approximately four order of magnitude smaller than any values used in the simulations.

The calculation detailed here may be performed for any setup being considered numerically or experimentally to test its feasibility, where d need only be the length of the region where the interaction is considered significant, as estimated here. Furthermore, this analysis may also come to use when considering the electron interacting with a chain of interacting Rydberg atoms, which is the case considered in the following section.

3.6 Extension to a Chain of Atoms

This section details how to use the Lippmann-Schwinger technique to describe the situation where there are multiple identical atoms trapped a distance Y from, and uniformly distributed along, a length of the electron wire. Two atoms labelled a and b will thus be separated by a distance $R_{ab} = ((a-b)R_s, 0, 0)$, as illustrated in Fig. 3.16, where R_s is the distance between neighbouring atoms. The interaction between the atoms is of the dipole-dipole form, written in general for two atoms as [179]

$$V_{\text{dd}} = \frac{\vec{r}_a \cdot \vec{r}_b}{|\vec{R}_{ab}|^3} - 3 \frac{(\vec{r}_a \cdot \vec{R}_{ab})(\vec{r}_b \cdot \vec{R}_{ab})}{|\vec{R}_{ab}|^5},$$

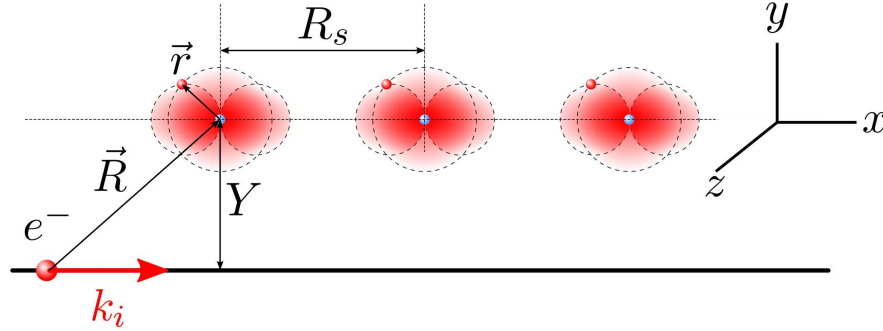


Figure 3.16: An illustration of the geometry and labels of the multiple atom system.

where \vec{r}_a and \vec{r}_b are the positions of the valence electrons of atoms a and b respectively. As here the atom separation only has a component in the x -direction, the dipole-dipole interaction of the many-atom system in question may be written explicitly as

$$V_{\text{dd}} = \frac{1}{R_s^3} \sum_{a \neq b}^N \frac{1}{|a-b|^3} (\vec{r}_a \cdot \vec{r}_b - 3x_a x_b), \quad (3.27)$$

where the sum accounts for the interaction between all the atoms in the system.

The focus of this investigation is how the passage of the electron affects the chain of interacting atoms, thus the interaction between the atoms themselves should be included in H_0 of the Lippmann-Schwinger equation (3.18). However, this is contrary to the fact that H_0 goes on to form the free-particle propagator in this approach, as the interaction between the atoms is not diagonal. In order to apply this approach, one must take the basis where V_{dd} is diagonal. The transformation which diagonalises V_{dd} will also be applied to the electron atom interaction, thus treating the atoms as an ensemble rather than individually. This diagonalisation of V_{dd} and transformation of the interaction will be detailed here before gaining an analytic scattering result using the Lippmann-Schwinger equation.

Once again, it is assumed that the atoms are trapped at a distance much fur-

ther from the electron wire then their valence electron orbital radii, $\langle r \rangle$. Taking the Born approximation, as in the single atom case, the transition amplitudes from the initial state (all atoms in the $|ns\rangle$ state) to those where one scattering event has taken place (one atom in the $|n'p\rangle$ state) will be calculated. As previously shown, the electron only couples the $|ns\rangle$ state to the $|n'p_+\rangle$ and $|n'p_-\rangle$ states, thus the $z_a z_b$ term of (3.27) may be eliminated as it only acts on atomic states where the p_0 -state is present. Also, as $V_{\text{dd}} \propto 1/R_{ab}^3$, only the nearest neighbour interaction will be considered. Defining the ensemble atomic excited state as $|n'p_\pm\rangle_u \equiv |ns^{(1)}, ns^{(2)}, \dots, n'p_\pm^{(u)}, \dots, ns^{(N)}\rangle$ such that the u^{th} atom in the chain is the one in the state $|n'p\rangle$, the dipole-dipole interaction may be written as

$$V_{\text{dd}}^{(\text{BA})} = \frac{\mu^2}{4R_s^3} \sum_{n', n''} \mu_{nn'} \mu_{nn''} \sum_{u=1}^N \left[3 |n''p_+\rangle_{u+1} \langle n'p_-| - |n''p_-\rangle_{u+1} \langle n'p_-| \right. \\ \left. - |n''p_+\rangle_{u+1} \langle n'p_+| + 3 |n''p_-\rangle_{u+1} \langle n'p_+| + \text{h.c.} \right].$$

The first step is to diagonalise the spin part of the dipole-dipole interaction, which allows a more compact version of it to be written down, as the atomic states present are then written as superpositions. The spin diagonalised basis is written as $|n'\chi\rangle_u$, where the excited (u^{th}) atom is now in the state $\chi = \pm$ with $+$ representing it being in the symmetric superposition state $|+\rangle = (|p_+\rangle + |p_-\rangle)/\sqrt{2}$ and $-$ representing it being in the anti-symmetric superposition state $|-\rangle = (|p_+\rangle - |p_-\rangle)/\sqrt{2}$. The dipole-dipole interaction is written in this new basis as

$$V_{\text{dd}}^{(\text{sd})} = \frac{1}{4R_s^3} \sum_{n', n''} \mu_{nn'} \mu_{nn''} \sum_{u=1}^N \left[2 \left(|n''+\rangle_{u+1} \langle n'+| + |n'+\rangle_u \langle n''+| \right) \right. \\ \left. - 4 \left(|n''-\rangle_{u+1} \langle n'-| + |n'-\rangle_u \langle n''-| \right) \right],$$

which is split into parts describing the atoms in either the $|+\rangle$ or $|-\rangle$ state, which

have different prefactors due to the diagonalisation. The position dependent part of this interaction, which may be separated as

$$H_{\text{pos}} = \sum_{u=1}^N \left[|u\rangle \langle u+1| + |u+1\rangle \langle u| \right],$$

needs now to be diagonalised. There are no periodic boundary conditions to this system, so the ansatz is made that the v^{th} positional eigenstate is of the form

$$|\psi_v, n'\chi\rangle = \sum_{u=1}^N \cos[\alpha uv + \beta] |n'\chi\rangle_u.$$

First ignoring the boundary terms, the eigenvalue problem for the bulk of the system,

$$\cos[\alpha(u+1)v + \beta] + \cos[\alpha(u-1)v + \beta] = \xi \cos[\alpha uv + \beta],$$

may be solved to find $\xi = 2 \cos[\alpha v]$. Turning now to the boundaries, $u = 1$ can be used to find

$$\cos[2\alpha v + \beta] = 2 \cos[\alpha v] \cos[\alpha v + \beta]$$

and obtain $\beta = -1/2$. Solving the equivalent equation for $u = N$ it is possible to find $\alpha = \pi/(N+1)$ such that the normalised eigenstates take the form

$$|\psi_v, n'\chi\rangle = \sqrt{\frac{2}{N+1}} \sum_{u=1}^N \sin \left[\frac{uv\pi}{N+1} \right] |n'\chi\rangle_u, \quad (3.28)$$

which have the energy eigenvalues

$$\mathcal{E}_{v, n'\chi} = \Delta \mathcal{E}_{n'p} - (1 \mp 3) \frac{\mu_{nn'}^2}{2R_s^3} \cos \left[\frac{v\pi}{N+1} \right]. \quad (3.29)$$

From the eigenstates, the unitary matrix that will diagonalise V_{dd} can be defined

as

$$U_{uv} = \sqrt{\frac{2}{N+1}} \sin \left[\frac{uv\pi}{N+1} \right], \quad (3.30)$$

where the next required step is to apply this unitary transformation to the electron-atom interaction matrix.

As an analogue to the single atom case, the initial state of the atomic system is chosen to be that where all the atoms are in the state $|ns\rangle$. In this many-body basis such a state will be written as $|\mathfrak{s}\rangle$. Thus referring back to the single atom calculation, only terms of the electron-atom interaction Hamiltonian concerning excitation from the state $|\mathfrak{s}\rangle$ are required. In the $|n'p_{\pm}\rangle_u$ basis, the electron-atomic ensemble interaction for excitation from the $|\mathfrak{s}\rangle$ state can be written as

$$H_{\text{int}} = \sum_{u=1}^N \sum_{n'} \frac{\mu_{nn'}}{2} \left[\frac{(\hat{x} - R_u) + iY}{[(\hat{x} - R_u)^2 + Y^2]^{\frac{3}{2}}} |n'p_{-}\rangle_u \langle \mathfrak{s}| \right. \\ \left. - \frac{(\hat{x} - R_u) - iY}{[(\hat{x} - R_u)^2 + Y^2]^{\frac{3}{2}}} |n'p_{+}\rangle_u \langle \mathfrak{s}| \right],$$

which is the part relevant to the Lippmann-Schwinger equation under the approximations taken here. To write this in the basis where V_{dd} is diagonal, $|\psi_v, n'\chi\rangle = \sum_{u=1}^N U_{uv} |n'\chi\rangle_u$, the coefficient of $|n'p_{-}\rangle_u \langle \mathfrak{s}|$ above is written as

$$A_u = \frac{(\hat{x} - R_u) + iY}{[(\hat{x} - R_u)^2 + Y^2]^{\frac{3}{2}}},$$

such that the matrix element for use in the Lippmann-Schwinger equation can be written as

$$\langle \psi_v, n'\chi | H_{\text{int}} | \mathfrak{s} \rangle = \mu_{nn'} \sum_{u=1}^N \frac{U_{vu}^*}{\sqrt{2}} (i\text{Im}(A_u)\delta_{\chi,+} - \text{Re}(A_u)\delta_{\chi,-}). \quad (3.31)$$

This matrix element may be used in the Lippmann-Schwinger equation written in the form given in (3.20), where now n' and n'' represent the many body eigenstate

label (v) and β' and β'' represent the spin degree of freedom (χ). Taking $|\phi\rangle = |k_i, \mathbf{s}\rangle$ and knowing the form of the interaction matrix elements (3.31), the Green's function matrix element can be gained from that in the single atom case (3.23), where once again n' may be replaced by the many-body eigenstate label and β' is taken to represent the spin degree of freedom. For the multiple atom system, the Lippmann-Schwinger equation is thus written as

$$\begin{aligned} \langle x | \Psi \rangle = & \langle x | \phi \rangle + \sum_{\substack{n', v, \chi \\ \sigma, \lambda}} \frac{\mu_{nn'}}{2} \left(-\frac{e^{i\lambda\sigma k_f x}}{k_f} \right) \int dx' \times e^{i\lambda(|k_i| - \sigma k_f)x'} \\ & \times \sum_u U_{vu}^* \left(i\text{Im}(A_u(x'))\delta_{\chi,+} - \text{Re}(A_u(x'))\delta_{\chi,-} \right) |n'\chi\rangle_u \end{aligned}$$

where $A_u(x)$ is the coefficient A_u with the operator status of x removed, $\sigma = +(-)$ represents a transmitted (reflected) electron and λ signifies the initial direction of travel. A final simplification to this expression is found by evaluation of the integral over x' , which can be shown to be

$$\begin{aligned} \int dx' e^{iax'} \text{Re}(A_j(x')) &= e^{iaR_j} 2iaK_0 [Y |a|] \\ \int dx' e^{iax'} \text{Im}(A_j(x')) &= e^{iaR_j} 2i |a| K_1 [Y |a|], \end{aligned}$$

and provide us with everything required to calculate the scattering amplitudes.

The transition amplitude $\sigma_{v,n'\chi}$ to the state $|\psi_v, n'\chi\rangle$ is found by taking the absolute value squared of the scattering amplitude from the Lippmann-Schwinger equation. This will be done here for the electron initially travelling in the positive direction and transmitted past the atom, as once again it can be shown that the transition amplitude for a reflected electron is effectively zero. The full expression

is given as

$$\sigma_{v,n'\chi} = \frac{2\mu_{nn'}^2}{k_f^2} \left[|k_i - k_f|^2 K_1^2(Y |k_i - k_f|) \delta_{\chi,+} + (k_i - k_f)^2 K_0^2(Y |k_i - k_f|) \delta_{\chi,-} \right] \\ \times \sum_{p,q=1}^N e^{ik_f(p-q)R_s} U_{vq}^* U_{pv}$$

where $k_f = \sqrt{k_i^2 - 2\mathcal{E}_{v,n'\chi}}$, with $\mathcal{E}_{v,n'\chi}$ the energy of the many-body eigenstate $|\psi_v, n'\chi\rangle$ as given in (3.29) and U_{pv} are the elements of the unitary matrix (3.30), which diagonalises V_{dd} . This may be cast into a much simpler form using knowledge of the variables in the system. First of all, μ^2/R_s^3 appears in $\mathcal{E}_{v,n'\chi}$, where in atomic units $\mu \sim 10^3$ and $R_s \sim 10^5$ for atoms trapped micrometres apart, thus $\mu^2/R_s^3 \ll \Delta\mathcal{E}_{n'p}$ and so $\mathcal{E}_{v,n'\chi} \approx \Delta\mathcal{E}_{n'p}$. The previously used assumption that the electron kinetic energy is much greater than the atomic energy level splitting ($\Delta\mathcal{E}_{n'p} \ll k^2$) is used, allowing the Taylor expansion of $\sqrt{k_i^2 - 2\Delta\mathcal{E}_{n'p}}$ about $\Delta\mathcal{E}_{n'p} = 0$. Introducing, as in the single atom case, the scaled momentum $\kappa = k_i/(Y\Delta|\mathcal{E}_{n'p}|)$ and coupling $\eta_{nn'} = \mu_{nn'}/(2Y^2|\Delta\mathcal{E}_{n'p}|)$, the transition amplitude may be written as

$$\sigma_{v,n'\chi} \approx \frac{8\eta_{nn'}^2}{\kappa^4} \left[K_1^2\left(\frac{1}{\kappa}\right) \delta_{\chi,+} + K_0^2\left(\frac{1}{\kappa}\right) \delta_{\chi,-} \right] \times \sum_{p,q=1}^N e^{ik_f(p-q)R_s} U_{vq}^* U_{pv}.$$

This may be simplified by performing the sum over the unitaries, which may be shown to be

$$\sum_{p,q=1}^N e^{ik_f(p-q)R_s} U_{vq}^* U_{pv} = \frac{1}{2(N+1)} \left(\frac{\sin(\alpha_v \frac{N}{2})}{\sin(\frac{\alpha_v}{2})} + (-1)^{n+1} \frac{\sin(\beta_v \frac{N}{2})}{\sin(\frac{\beta_v}{2})} \right)^2,$$

where

$$\alpha_v = \frac{v\pi}{N+1} + \frac{R_s}{\kappa Y} \quad \text{and} \quad \beta_v = \frac{v\pi}{N+1} - \frac{R_s}{\kappa Y}.$$

The transition amplitude is then finally written as

$$\begin{aligned} \sigma_{v,n'\chi} = & \frac{4}{N+1} \left(\frac{\eta_{nn'}}{\kappa^2} \right)^2 \left[K_1^2 \left(\frac{1}{\kappa} \right) \delta_{\chi,+} + K_0^2 \left(\frac{1}{\kappa} \right) \delta_{\chi,-} \right] \\ & \times \left(\frac{\sin(\alpha_v \frac{N}{2})}{\sin(\frac{\alpha_v}{2})} + (-1)^{n+1} \frac{\sin(\beta_v \frac{N}{2})}{\sin(\frac{\beta_v}{2})} \right)^2, \end{aligned} \quad (3.32)$$

whose magnitude depends on the coupling strength $\eta_{nn'}$ multiplied by a function whose form depends on the multi-atom state and the ratio of the atomic separation to the trapping distance. As in the single atom case, this result will only be valid in the weak coupling limit, where $\eta_{nn'} \ll 1$.

It is also possible to calculate the total transition amplitude, which may be taken as a measure of the probability that the atom undergoes any of the possible transitions. This is shown to be proportional to the number of atoms N , and is written as

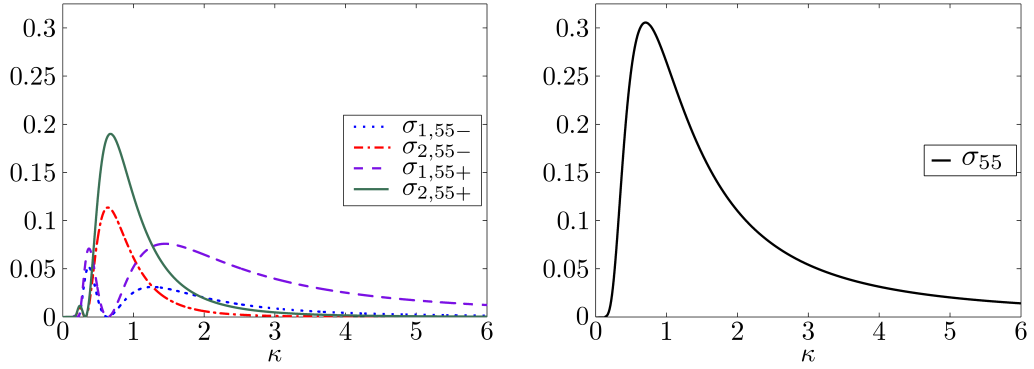
$$\sigma_{n'p} = 8N \left(\frac{\eta_{nn'}}{\kappa^2} \right)^2 \left[K_1^2 \left(\frac{1}{\kappa} \right) + K_0^2 \left(\frac{1}{\kappa} \right) \right].$$

Limiting the transitions to those where the principal quantum number remains the same, the previous analysis may be used to find the states of a two atom system and their energies (before approximations are made). The possible states of the system may be shown to be

$$\begin{aligned} |\psi_1, 55+\rangle &= \frac{1}{2} \left(|55p_+, 55s\rangle + |55p_-, 55s\rangle + |55s, 55p_+\rangle + |55s, 55p_-\rangle \right) \\ |\psi_1, 55-\rangle &= \frac{1}{2} \left(|55p_+, 55s\rangle - |55p_-, 55s\rangle + |55s, 55p_+\rangle - |55s, 55p_-\rangle \right) \\ |\psi_2, 55+\rangle &= \frac{1}{2} \left(|55p_+, 55s\rangle + |55p_-, 55s\rangle - |55s, 55p_+\rangle - |55s, 55p_-\rangle \right) \\ |\psi_2, 55-\rangle &= \frac{1}{2} \left(|55p_+, 55s\rangle - |55p_-, 55s\rangle - |55s, 55p_+\rangle + |55s, 55p_-\rangle \right), \end{aligned}$$

which have energies $\mathcal{E}_{1,55+} = \Delta\mathcal{E}_{55p} - \mu_{55}^2/2R_s^3$, $\mathcal{E}_{1,55-} = \Delta\mathcal{E}_{55p} + \mu_{55}^2/R_s^3$, $\mathcal{E}_{2,55+} = \Delta\mathcal{E}_{55p} + \mu_{55}^2/2R_s^3$ and $\mathcal{E}_{2,55-} = \Delta\mathcal{E}_{55p} - \mu_{55}^2/R_s^3$ respectively. Before showing the transition amplitudes associated with these states, it is important to note that

these states are entangled, as it is not possible to separate the state of the first atom from that of the second. The transition amplitudes for these four possible states of the system are shown in Fig. 3.17(a). It is clear that the form of the



(a) First order transition amplitudes for the four states of the double atom system.

(b) Total first order transition amplitude for the double atom system.

Figure 3.17: Single state (a) and total (b) transition amplitudes for the two atom case. The values are for a rubidium atom initially in the $|55s\rangle$ state with $Y = 2.5\mu\text{m}$ and $R_s = 2Y$.

amplitude for varying κ depends on the form of the entangled state, where those with $|\psi_2\rangle$ show one dominant peak with the $|\psi_1\rangle$ form showing two much smaller peaks. Fig. 3.17(b) shows that the total transition amplitude yields a result reminiscent of that for the single atom case. It has been shown that by interacting with a passing electron the atomic ensemble may undergo transitions to entangled states. Selecting the momentum of the atom will therefore allow one of the states to be produced, which will have applications in the fields of quantum information and computing.

This section has presented the general multi atom case and a brief analysis of the two atom system, which shows that the results are clearly related to those of the single atom case. The following section gives a description of two possible regimes for the multiple atom system, and evaluates their feasibility.

3.6.1 Interatomic Interaction Dominated and Electron-Atom Interaction Dominated Regimes

There will be two distinct regions to the multiple atom case: that where the atomic dipole-dipole interaction dominates and that where the electron-atom interaction dominates. This short section is dedicated to an analysis of whether these two regions are realistically achievable with this type of approach. In order to find an estimate of where the boundary between the two lies, the maximum strength of the electron-atom interaction (where the electron is closest to one of the atoms) is equated with the dipole-dipole interaction. Taking the form of the electron-atom interaction after the Taylor expansion (3.5) and inserting $x = 0$, its strength may be estimated using the expectation value $\langle y \rangle$ after the interaction as $\langle y \rangle / Y^2$. Using also the expectation values $\langle x \rangle$ and $\langle y \rangle$ from the appropriate single atom calculation in the numerator of the dipole-dipole interaction (3.27) and writing it as $D = \langle y_a \rangle \langle y_b \rangle - 2 \langle x_a \rangle \langle x_b \rangle$, the inequality which yields the boundary, R_s^0 , may be solved as

$$R_s^0 = \sqrt[3]{\frac{DY^2}{\langle y \rangle}}. \quad (3.33)$$

This does highlight a problem with using the dipole-dipole interaction to produce novel results in the multiple atom case: it is comparatively weak. For example, taking values which should be achievable for a $|55s\rangle$ rubidium atom and are expected to give a high polarisation, $\alpha = 0.225$ and $E_{\text{kin}} \approx 0.87\text{eV}$, the above equation gives that $R_s^0 \approx 0.35\mu\text{m}$, which is only slightly greater than the atomic orbital radius. Thus the dipole-dipole approximation will break down before the separation distance is small enough for it to become dominant. Obviously the atoms still interact strongly at shorter distances, but it becomes a much more difficult problem to treat. However, what has been shown analytically in this section is that even well into the region where the electron-atom interaction is dominant,

the dipole-dipole interaction still has an effect on the possibly achievable states, as seen in Fig. 3.17.

3.7 Summary and Outlook

The various sections in this chapter have shown how controlling the momentum of an electron may be used to manipulate the internal state of a Rydberg atom. An analytic approximation for the changing of the atomic state in the weak coupling limit was found via two different methods, which predicted that the incident direction of the electron selects which magnetic sublevel is most likely populated. The time-dependent Schrödinger equation was subsequently used as the basis of a numerical exploration of the system, allowing the validity of the analytics to be analysed for two different atomic species. It is shown that the analytics and numerics compare very well in the case of rubidium, and not so well in the case of lithium. This difference is attributed to the two species having distinctly different spectra. The number of dipole transitions the atom is likely to have made during the passage of the electron is quantified by the average orbital angular momentum and magnetic quantum numbers of the final state, and it is shown that the final state may be very far from the initial s -state. The final state of the atom was also used to calculate its final polarisation, which shows that it is possible to use the electron to create a *permanent* dipole moment of the atom, though this would only have the lifetime of the final atomic state itself. If the lifetime of these states is sufficiently long, this may allow proposals based around polar molecules [180,181] to be realised with these switchable atomic dipole moments. The final section detailed the extension of the analytic approach to a chain of N interacting atoms, and gives a brief description of the possible regimes achievable.

It is clear throughout this analysis that more exotic states of the atom are reached when the coupling strength η_n is high. There are two main reasons

why this coupling strength may not be made arbitrarily high. The first is the difficulty in reaching Rydberg states with high principal quantum numbers, where usually multi-photon resonances are required. The second is the requirement of a minimum distance between the electron and the atom. Such a minimum distance has already been used such that in the theoretical sense the electron may be treated as a point charge. An even clearer reason is apparent from the experimental side, where it must be ensured that the effects of the electron guiding field on the atom are minimal. One possible alternative which would allow the interaction strength to be increased would be to replace the electron by a highly charged ion. The description of such a system would be very similar to that given here, though the energy scales would be very different and could therefore yield further interesting results.

Appendices

Appendix A

Atomic Units

The following table provides the conversion factors between atomic and SI units.

Quantity	Atomic Units	SI Units (3.s.f)
Mass	$m_e = 1$	$9.11 \times 10^{-31} \text{kg}$
Charge	$ e = 1$	$1.60 \times 10^{-19} \text{C}$
Angular Momentum	$\hbar = 1$	$1.05 \times 10^{-34} \text{J.s}$
Coulomb Constant	$k_e = 1/(4\pi\epsilon_0) = 1$	$8.99 \times 10^9 \text{N.m}^2.\text{C}^{-2}$
Length	$a_0 = \hbar^2/(k_e m_e e^2) = 1$	$5.29 \times 10^{-11} \text{m}$
Energy	$E_h = k_e e^2/a_0 = 1$	27.2eV
Time	$\hbar^3/(k_e^2 m_e e^4) = 1$	$2.42 \times 10^{-17} \text{s}$
Electric Field	$k_e e/a_0^2 = 1$	$5.14 \times 10^{11} \text{V.m}^{-1}$

Table A.1: Table showing the definition of the atomic units and their values in SI units.

Appendix B

Interaction of a Two-Level Atom with a Classical Field

This appendix details the derivation of the interaction of a two-level atom with a classical laser field, which is included in the Hamiltonian of the lambda system (2.29). This forms part of the basis of the generation of quantum states of light from the collective bosonic excitations of the lattice system. The derivation presented here follows closely that presented in [182]. As a simple case here, which is also taken at a later point in the main derivation, the laser is assumed to be linearly polarised. In this example, such polarisation is along the x -axis, such that the electric field at position \mathbf{r} may be written as

$$\mathbf{E}(\mathbf{r}, t) = \mathcal{E}_L(\mathbf{r}, t) \cos(\mathbf{k}_L \cdot \mathbf{r} - \omega_L t),$$

where $\mathcal{E}_L(\mathbf{r}, t)$ is a slowly varying envelope function, with ω_L the optical frequency and \mathbf{k}_L the wavevector. The atom may be assumed to have only two levels if the transition is dipole allowed and far detuned from all other atomic transitions. Thus, in this case, the two levels involved are $|s\rangle$ and $|a\rangle$, whose transition frequency is ω_a (for simplicity setting $\omega_s = 0$). The envelope function may be

approximated as constant so long as it varies on a length scale much longer than the optical wavelength, $2\pi/|\mathbf{k}_L|$, and a timescale much slower than the optical frequency, ω_L . Under these conditions, the envelope function may be approximated as $\mathcal{E}_L(\mathbf{r}, t) \approx \mathcal{E}_L \hat{\mathbf{e}}_x$, where $\hat{\mathbf{e}}_x$ is the unit vector in the x -direction and \mathcal{E}_L is the (real) amplitude. Using the definition given in [47], the interaction between an atom and electric field is given by

$$H_{\text{int}} = -\hat{\mathbf{d}} \cdot \mathbf{E}(\mathbf{r}, t),$$

where $\hat{\mathbf{d}} = -e\hat{\mathbf{r}}$ is the dipole moment operator. Using the fact that the atom does not have a permanent electric dipole when in either the state $|a\rangle$ or $|s\rangle$ and the electric field is polarised in the x -direction, the dipole operator may be written as

$$\mathbf{d} = -(\mathbf{d}_{\text{as}} |a\rangle \langle s| + \mathbf{d}_{\text{as}}^* |s\rangle \langle a|),$$

where $\mathbf{d}_{\text{as}} = \mathbf{d}_{\text{as}}^* = \langle a | x | s \rangle \hat{\mathbf{e}}_x$ due to the choice of polarisation direction.

The Hamiltonian describing the interaction between the atom and classical electric field is thus given as

$$H_{\text{int}} = \Omega_L (e^{i(\mathbf{k}_L \cdot \mathbf{r} - \omega_L t)} + e^{-i(\mathbf{k}_L \cdot \mathbf{r} - \omega_L t)}) (|a\rangle \langle s| + |s\rangle \langle a|),$$

where the cosine term has been decomposed into exponentials and the Rabi frequency is thus written as $\Omega_L = d_{\text{as}} \mathcal{E}_L / 2$ with $\mathbf{d}_{\text{as}} = d_{\text{as}} \hat{\mathbf{e}}_x$. To simplify this Hamiltonian, it is first transformed to the interaction picture, such that rapidly oscillating terms may be identified and neglected when applying the rotating wave approximation [127]. To express the Hamiltonian in the interaction picture, a unitary transformation of the form

$$U_I = e^{iH_0 t}$$

is performed, where $H_0 = \omega_a |a\rangle \langle a|$. The matrix form of this operator can be shown to be $U_I = |s\rangle \langle s| + e^{i\omega_a t} |a\rangle \langle a|$, such that, in the interaction picture, the Hamiltonian is expressed as

$$H_{\text{int}}^{(1)} = U_I H_{\text{int}} U_I^\dagger = \Omega_L \left[\left(e^{i(\mathbf{k}_L \cdot \mathbf{r} + (\omega_a - \omega_L)t)} + e^{-i(\mathbf{k}_L \cdot \mathbf{r} - (\omega_L + \omega_a)t)} \right) |a\rangle \langle s| + \left(e^{i(\mathbf{k}_L \cdot \mathbf{r} - (\omega_L + \omega_a)t} + e^{-i(\mathbf{k}_L \cdot \mathbf{r} + (\omega_a - \omega_L)t)} \right) |s\rangle \langle a| \right]. \quad (\text{B.1})$$

The rotating wave approximation neglects the rapidly oscillating terms, which in this case are those of frequency $\omega_L + \omega_a$, and the Hamiltonian is thus approximated as

$$H_{\text{int}}^{(1)} \approx \Omega_L \left[e^{i(\mathbf{k}_L \cdot \mathbf{r} + (\omega_a - \omega_L)t)} |a\rangle \langle s| + e^{-i(\mathbf{k}_L \cdot \mathbf{r} + (\omega_a - \omega_L)t)} |s\rangle \langle a| \right].$$

Transforming back to the Schrödinger picture by the inverse of this transformation yields the interaction Hamiltonian in the rotating wave approximation, which is valid so long as the detuning $\Delta_L = \omega_L - \omega_a \ll \omega_L + \omega_a$. Omitting the intermediate steps, this inverse transformation yields

$$H_{\text{int}} = U_I^\dagger H_{\text{int}}^{(1)} U_I = \Omega_L \left[e^{i(\mathbf{k}_L \cdot \mathbf{r} - \omega_L t)} |a\rangle \langle s| + e^{-i(\mathbf{k}_L \cdot \mathbf{r} - \omega_L t)} |s\rangle \langle a| \right],$$

which describes the interaction of the atom with a linearly polarised electric field in the rotating wave approximation. This transformation can be easily shown to leave the atomic part of the Hamiltonian unaffected.

Appendix C

Transformation to a Rotating Frame

In sections 2.4.1 and 2.6.2 the relevant Hamiltonian is transformed such that it describes the system in a rotating frame. This brief appendix details how such a unitary rotation is performed. Such a transformation allows the time dependence to be removed from the Hamiltonian when the rotating wave approximation is applied. Introducing the general unitary rotation matrix \mathcal{U} , an effective Hamiltonian must be defined which acts on the rotated states of the system and obeys the time-dependent Schrödinger equation. With the original Hamiltonian represented as H , this process is carried out as

$$i\hbar\partial_t |\psi\rangle = H |\psi\rangle$$

$$i\hbar\mathcal{U}\partial_t\mathcal{U}^\dagger |\psi\rangle = \mathcal{U}H\mathcal{U}^\dagger |\psi\rangle$$

$$i\hbar\mathcal{U}\partial_t\mathcal{U}^\dagger |\phi\rangle = \mathcal{U}H\mathcal{U}^\dagger |\phi\rangle$$

$$i\hbar\mathcal{U}\mathcal{U}^\dagger + i\hbar\mathcal{U}\partial_t (\mathcal{U}^\dagger |\phi\rangle) = \mathcal{U}H\mathcal{U}^\dagger |\phi\rangle$$

$$i\hbar\partial_t |\phi\rangle = (\mathcal{U}H\mathcal{U}^\dagger - i\hbar\mathcal{U}\partial_t\mathcal{U}^\dagger) |\phi\rangle,$$

where $|\phi\rangle = \mathcal{U}^\dagger |\psi\rangle$ is the state of the system in the rotating frame. The final line of the derivation defines the effective Hamiltonian in the rotating frame as

$$H' = \mathcal{U}H\mathcal{U}^\dagger - i\hbar\mathcal{U}\partial_t\mathcal{U}^\dagger,$$

as this line is the time-dependent Schrödinger equation for the state in the rotating frame. Note here that \hbar has been included to make the Schrödinger equation easier to identify, where atomic units are more commonly used in the rest of this text.

The main body of text refers to altering the energy of one of the atomic states by a certain frequency using a transformation of this type. Taking the simple case of a two level atom of Rabi frequency 2Ω and electric field frequency ω_L , the Hamiltonian may be written as

$$\mathcal{H} = \begin{pmatrix} \omega_a & 0 \\ 0 & 0 \end{pmatrix} + 2\Omega \begin{pmatrix} 0 & 1 \\ 1 & 0 \end{pmatrix} \cos(\omega_L t),$$

where ω_a is the energy difference between the two states, and atomic units are used. The matrix used to move to a frame rotating with the frequency of the laser may be written as

$$\mathcal{U} = \begin{pmatrix} e^{i\omega_L t} & 0 \\ 0 & 1 \end{pmatrix},$$

which can easily be shown to be unitary. Upon application of the process to transform to a rotating frame, the effective Hamiltonian may be shown to be

$$\mathcal{H}' = \begin{pmatrix} \omega_a - \omega_L & 0 \\ 0 & 0 \end{pmatrix} + \Omega \begin{pmatrix} 0 & 1 + e^{2i\omega_L t} \\ 1 + e^{-2i\omega_L t} & 0 \end{pmatrix},$$

where the cosine term describing the oscillating electric field has been split into exponentials. This clearly shows that the energy of the excited state has been

reduced in energy by the frequency of the laser. It is also the point at which the rotating wave approximation [127] may be applied to remove the rapidly oscillating terms in each off-diagonal element, which is valid when the laser is near resonant with the atomic transition, $\omega_L \approx \omega_a$. As is also encountered in the text, it is sometimes necessary to increase the energy of one of the states of the system. This may be done by changing the sign of the exponential in \mathcal{U} and applying the same procedure.

Appendix D

Adiabatic Elimination of the Auxiliary State

The effective Hamiltonian of the lambda system where the energy of the auxiliary state $|s\rangle$ has been reduced by an amount ω_L (2.30) may be simplified under the assumption that the laser detuning is far from resonant. This assumption leads to the approximation that the population of the auxiliary state is approximately constant. This appendix details how this approximation may be used to adiabatically eliminate the auxiliary level from the lambda system. Using the time dependent Schrödinger equation, $i\partial_t |\psi\rangle = H' |\psi\rangle$, with the effective Hamiltonian (2.30) and each of the three atomic levels of the system yields the three coupled differential equations

$$\begin{aligned}i\dot{a} &= H' |a\rangle = (\omega_a - \omega_L) |a\rangle + e^{-i\mathbf{k}_L \cdot \mathbf{r}} |s\rangle + (\Omega_{\text{em}} + \Omega_{\text{em}}^*) e^{-i\omega_L t} |g\rangle \\i\dot{s} &= H' |s\rangle = \omega_s |s\rangle + e^{i\mathbf{k}_L \cdot \mathbf{r}} |a\rangle \\i\dot{g} &= H' |g\rangle = \omega_g |g\rangle + (\Omega_{\text{em}} + \Omega_{\text{em}}^*) e^{i\omega_L t} |a\rangle,\end{aligned}$$

where the dot represents the first temporal derivative. The assumptions previously mentioned amount to the statement $\dot{a} \approx 0$, which allows an expression for

the state $|a\rangle$ in terms of the other two states to be gained from the first of these equations, yielding

$$|a\rangle \approx -\frac{\Omega_L}{\Delta_L} e^{-i\mathbf{k}_L \cdot \mathbf{r}} |s\rangle - \frac{\Omega_{\text{em}} + \Omega_{\text{em}}^*}{\Delta_L} e^{-i\omega_L t} |g\rangle$$

where $\Delta_L = \omega_a - \omega_L$. Inserting this expression and that of its Hermitian conjugate into the Hamiltonian (2.30) allows the removal of the auxiliary state, such that it may be simplified to

$$\begin{aligned} H' \approx & \left(\omega_s - \frac{\Omega_L^2}{\Delta_L} \right) |s\rangle \langle s| + \left(\omega_g - \frac{(\Omega_{\text{em}} + \Omega_{\text{em}}^*)^2}{\Delta_L} \right) |g\rangle \langle g| + \sum_{\mathbf{q}\lambda} \omega_{\mathbf{q}\lambda} \hat{a}_{\mathbf{q}\lambda}^\dagger \hat{a}_{\mathbf{q}\lambda} \\ & - \frac{\Omega_L(\Omega_{\text{em}} + \Omega_{\text{em}}^*)}{\Delta_L} \left(e^{-i(\mathbf{k}_L \cdot \mathbf{r} - \omega_L t)} |s\rangle \langle g| + e^{i(\mathbf{k}_L \cdot \mathbf{r} - \omega_L t)} |g\rangle \langle s| \right). \end{aligned} \quad (\text{D.1})$$

This completes the adiabatic elimination of the auxiliary state, a final step being to neglect the corrections to the ground state energies, which yields the Hamiltonian given in the main body of the text as equation (2.31).

Appendix E

Atomic Transition Dipole Elements

Using the spherical harmonics, the atomic transition dipole matrix elements can be shown to be

$$\begin{aligned} \langle \psi_{nlm} | \hat{x}_a + i\hat{y}_a | \psi_{n'l'm'} \rangle = & \left(\sqrt{\frac{(l-m+2)(l-m+1)}{(2l+1)(2l+3)}} \delta_{l',l+1} \right. \\ & \left. - \sqrt{\frac{(l+m-1)(l+m)}{(2l+1)(2l-1)}} \delta_{l',l-1} \right) \delta_{m',m-1} \mathfrak{R}_{nl,n'l'} \end{aligned}$$

and

$$\begin{aligned} \langle \psi_{nlm} | \hat{x}_a - i\hat{y}_a | \psi_{n'l'm'} \rangle = & \left(\sqrt{\frac{(l-m)(l-m-1)}{(2l-1)(2l+1)}} \delta_{l',l-1} \right. \\ & \left. - \sqrt{\frac{(l+m+1)(l+m+2)}{(2l+1)(2l+3)}} \delta_{l',l+1} \right) \delta_{m',m+1} \mathfrak{R}_{nl,n'l'} \end{aligned}$$

where $\mathfrak{R}_{nl,n'l'} = \langle \mathcal{R}_{n,l} | r | \mathcal{R}_{n',l'} \rangle$ are the radial transition dipole matrix elements, which may be estimated analytically using [67].

Appendix F

Lippmann-Schwinger Scattering Beyond the Born Approximation

This appendix gives the result of the Lippmann-Schwinger equation for the single trapped atom system for the first order beyond the Born approximation. This result is gained by using the result of the Born approximation case (3.24) (where an electron travelling to the right and transmitted is subsequently assumed) and inserting it as the state $|\phi\rangle$ in the Lippmann-Schwinger equation for this system (3.20). The result is

$$\begin{aligned} \langle x | \psi^{(2)} \rangle = & \frac{1}{\sqrt{2\pi}} \left[e^{ik_i x} |n_i s\rangle + \sum_{n_1, \beta_1} \left\{ \frac{e^{ik_f^{(1)} x}}{k_f^{(1)}} \mu_{n_i, n_1} \right. \right. \\ & \times \left(\delta_{\beta_1, p_+} \mathcal{G}(k_i - k_f^{(1)}) - \delta_{\beta_1, p_+} \mathcal{F}(k_i - k_f^{(1)}) \right) |n_1, \beta_1\rangle \\ & + \sum_{n_2, \beta_2} \left[\frac{\mu_{n_i, n_1}}{k_f^{(1)}} \frac{e^{ik_f^{(2)} x}}{k_f^{(2)}} \left(\delta_{\beta_1, p_-} \mathcal{G}(k_i - k_f^{(1)}) \left\{ \delta_{\beta_2, s} \mu_{n_2, n_1} \mathcal{F}(k_f^{(1)} - k_f^{(2)}) \right. \right. \right. \\ & + \mu_{n_2 \beta_2, n_1, \beta_1} \left[\delta_{\beta_2, d_0} \mathcal{F}(k_f^{(1)} - k_f^{(2)}) + \delta_{\beta_2, d_{-2}} \mathcal{G}(k_f^{(1)} - k_f^{(2)}) \right] \left. \right\} \\ & - \delta_{\beta_1, p_+} \mathcal{F}(k_i - k_f^{(1)}) \left\{ -\delta_{\beta_2, s} \mu_{n_2, n_1} \mathcal{G}(k_f^{(1)} - k_f^{(2)}) + \mu_{n_2 \beta_2, n_1, \beta_1} \right. \\ & \left. \left. \times \left[\delta_{\beta_2, d_0} \mathcal{G}(k_f^{(1)} - k_f^{(2)}) + \delta_{\beta_2, d_{+2}} \mathcal{F}(k_f^{(1)} - k_f^{(2)}) \right] \right\} \right] |n_2, \beta_2\rangle \left. \right] \end{aligned}$$

where $k_f^{(1)} = \sqrt{k_i^2 - 2\Delta\mathcal{E}_{n_1,\beta_1}}$ is the electron momentum after the first scattering event, $k_f^{(2)} = \sqrt{k_i^2 - 2\Delta\mathcal{E}_{n_2,\beta_2}}$ is the electron momentum after the second scattering event, n_i is the initial principal quantum number of the atom, n_1 and n_2 are the principal quantum numbers of the atom after one and two scattering events respectively, β_1 can represent the states $|p_\pm\rangle$, whereas β_2 may represent the states $|s\rangle$ and $|d_{0,\pm 2}\rangle$. The transition dipole moments μ_{n_a,n_b} are of the form given in section 3.3, whereas those written as $\mu_{n_1\beta_1,n_2\beta_2}$ need to be calculated from

$$\mu_{n_1\beta_1,n_2\beta_2} = \langle n_1\beta_1 | x_a + iy_a | n_2\beta_2 \rangle + \langle n_1\beta_1 | x_a - iy_a | n_2\beta_2 \rangle$$

using the forms of the matrix elements given in appendix E.

Despite the complicated form of this expression, the interpretation is straightforward. The first term (that preceding the state $|n_i s\rangle$) describes the state where no scattering event has occurred, thus the atomic state and electron momentum remain the same. The two terms preceding the state $|n_1\beta_1\rangle$ describes the state of the system when only a single order scattering event has taken place, in which case the atomic state will be $|n_1 p_\pm\rangle$, with the electron changing momentum to $k_f^{(1)}$ to conserve energy. The terms which follow those describing first order and precede the state $|n_2\beta_2\rangle$, describe the state after the various possibilities for second order scattering have occurred. These terms therefore describe the final state of the system when the atom undergoes a first order transition to $|n_1, \beta_1\rangle$ and then undergoes a second order scattering event leaving it in the state $|n_2, \beta_2\rangle$. The electron is thus left with the energy conserving momentum $k_f^{(2)}$. Although not shown here, it is possible to rewrite the beyond Born approximation expression in terms of the unitless momentum κ as was done in section 3.4. Doing this shows that the terms describing second order scattering events are of the order η^2 , which can be seen in this form as roughly $\mu^2/(k_f^{(1)}k_f^{(2)})$, and thus makes them less likely to occur than the first order scattering, as is expected.

In principle it is possible to gain an expression describing the third order scattering events using this method, though it is expected that the result will be extremely complex and perhaps not so informative.

Bibliography

- [1] Bloch I, Dalibard J and Zwerger W 2008 *Rev. Mod. Phys.* **80** 885
- [2] Jaksch D and Zoller P 2005 *Ann. of Phys.* **315** 52
- [3] Ghosh P N 2001 *Physics with cold atoms* (Allied Publ. Ltd.)
- [4] Metcalf H J and Straten P V 1999 *Laser cooling and trapping* (Springer-Verlag GmbH)
- [5] Balykin V I, Minogin V G and Letokhov V S 2000 *Rep. Prog. Phys.* **63** 1429
- [6] Anderson M H, Ensher J R, Matthews M R, Wieman C E and Cornell E A 1995 *Science* **269** 198
- [7] Davis K B, Mewes M O, Andrews M R, van Druten N J, Durfee D S, Kurn D M and Ketterle W 1995 *Phys. Rev. Lett.* **75** 3969
- [8] Bose S N 1924 *Z. Phys.* **26** 178
- [9] Einstein A 1925 *Sitzungsber. Kgl. Preuss. Akad. Wiss.* **1** 3
- [10] Andrews M R, Townsend C G, Miesner H J, Durfee D S, Kurn D M and Ketterle W 1997 *Science* **275** 637
- [11] Cirac J I, Gardiner C W, Naraschewski M and Zoller P 1996 *Phys. Rev. A* **54** R3714

- [12] Stamper-Kurn D M, Andrews M R, Chikkatur A P, Inouye S, Miesner H J, Stenger J and Ketterle W 1998 *Phys. Rev. Lett.* **80** 2027
- [13] Barrett M D, Sauer J A and Chapman M S 2001 *Phys. Rev. Lett.* **87** 010404
- [14] Bloch I, Hänsch T W and Esslinger T 2000 *Nature* **403** 166
- [15] Madison K W, Chevy F, Wohlleben W and Dalibard J 2000 *Phys. Rev. Lett.* **84** 806
- [16] Matthews M R, Anderson B P, Haljan P C, Hall D S, Wieman C E and Cornell E A 1999 *Phys. Rev. Lett.* **83** 2498
- [17] Feenstra L, Andersson L M and Schmiedmayer J 2004 *Gen. Relat. Gravit.* **36** 2317
- [18] Hänsel W, Hommelhoff P, Hänsch T W and Reichel J 2001 *Nature* **413** 498
- [19] Folman R, Krüger P, Schmiedmayer J, Denschlag J and Henkel C 2002 *Adv. At., Mol., Opt. Phys.* **48** 263
- [20] Adams C S 1994 *Contemp. Phys.* **35** 1
- [21] Berman P R 1997 *Atom Interferometry* (Academic press)
- [22] Bloch I 2005 *Nature Phys.* **1** 23
- [23] Grimm R, Weidemüller M and Ovchinnikov Y B 2000 *Adv. At., Mol., Opt. Phys.* **42** 95
- [24] Grynberg G and Courtois J Y 1994 *Europhys. Lett.* **27** 41
- [25] Hemmerich A, Weidmüller M, Esslinger T, Zimmerman C and Hänsch T 1995 *Phys. Rev. Lett.* **75** 37
- [26] Feynman R P 1982 *Int. J. Theor. Phys.* **21** 467

-
- [27] Feynman R P 1985 *Opt. News* **11** 1
- [28] Feynman R P 1986 *Found. Phys.* **16** 507
- [29] Lloyd S 1996 *Science* 1073
- [30] Lewenstein M, Sanpera A, Ahufinger V, Damski B, Sen A and Sen U 2007 *Adv. Phys.* **56** 243
- [31] Greiner M and Fölling S 2008 *Nature* **453** 736
- [32] Hubbard J 1964 *Proc. R. Soc. London, Ser. A.* **281** 401
- [33] Greiner M, Mandel O, Esslinger T, Hänsch T W and Bloch I 2002 *Nature* **415** 39
- [34] Jördens R, Strohmaier N, Günter K, Moritz H and Esslinger T 2008 *Nature* **455** 204
- [35] Lee P A, Nagaosa N and Wen X G 2006 *Rev. Mod. Phys.* **78** 17
- [36] DiVincenzo D P 1995 *Science* **270** 255
- [37] Garcia-Ripoll J J, Zoller P and Cirac J I 2005 *J. Phys. B: At., Mol., Opt. Phys.* **38** S567
- [38] Penrose R 1998 *Phil. Trans. R. Soc. A* **356** 1927
- [39] Jozsa R and Linden N 2003 *Proc. R. Soc. Lond. A* **459** 2011
- [40] Shor P W 1997 *SIAM J. Comput.* **26** 1484
- [41] Deutsch I H and Brennen G K 2000 *Fortschr. Phys.* **48** 925
- [42] Negretti A, Treutlein P and Calarco T 2011 *Quantum Inf. Process.* **10** 721
- [43] Jaksch D 2004 *Contemp. Phys.* **45** 367

-
- [44] Brennen G K, Caves C M, Jessen P S and Deutsch I H 1999 *Phys. Rev. Lett.* **82** 1060
- [45] Jaksch D, Briegel H J, Cirac J I, Gardiner C W and Zoller P 1999 *Phys. Rev. Lett.* **82** 1975
- [46] Weitenberg C, Endres M, Sherson J F, Cheneau M, Schauß P, Fukuhara T, Bloch I and Kuhr S 2011 *Nature* **471** 319
- [47] Gerry C C and Knight P L 2005 *Introductory Quantum Optics* (Cambridge University Press)
- [48] Hammerer K, Sørensen A S and Polzik E S 2010 *Rev. Mod. Phys.* **82** 1041
- [49] Kuzmich A, Mølmer K and Polzik E S 1997 *Phys. Rev. Lett.* **79** 4782
- [50] Hald J, Sørensen J L, Schori C and Polzik E S 1999 *Phys. Rev. Lett.* **83** 1319
- [51] Boller K J, Imamoglu A and Harris S E 1991 *Phys. Rev. Lett.* **66** 2593
- [52] Hau L V, Harris S E, Dutton Z and Behroozi C H 1999 *Nature* **397** 594
- [53] Fleischhauer M and Lukin M D 2000 *Phys. Rev. Lett.* **84** 5094
- [54] Yimsiriwattana A and Lomonaco Jr S J 2004 *arXiv preprint quant-ph/0402148*
- [55] Deutsch D 1989 *Proc. R. Soc. A.* **425** 73
- [56] Kuhn A, Hennrich M and Rempe G 2002 *Phys. Rev. Lett.* **89** 067901
- [57] Cirac J I, Zoller P, Kimble H J and Mabuchi H 1997 *Phys. Rev. Lett.* **78** 3221
- [58] Briegel H J, Dür W, Cirac J I and Zoller P 1998 *Phys. Rev. Lett.* **81** 5932

- [59] Duan L M, Lukin M D, Cirac J I and Zoller P 2001 *Nature* **414** 413
- [60] Kuzmich A, Bowen W P, Boozer A D, Boca A, Chou C W, Duan L M and Kimble H J 2003 *Nature* **423** 731
- [61] van der Wal C H, Eisaman M D, André A, Walsworth R L, Phillips D F, Zibrov A S and Lukin M D 2003 *Science* **301** 196
- [62] Chou C W, Polyakov S V, Kuzmich A and Kimble H J 2004 *Phys. Rev. Lett.* **92** 213601
- [63] Matsukevich D N and Kuzmich A 2004 *Science* **306** 663
- [64] Chen S, Chen Y A, Strassel T, Yuan Z S, Zhao B, Schmiedmayer J and Pan J W 2006 *Phys. Rev. Lett.* **97** 173004
- [65] Bethe H A and Salpeter E A 1957 *Quantum Mechanics of One and Two Electron Atoms* (Academic Press, New York)
- [66] Gallagher T F 1994 *Rydberg Atoms* (Cambridge University Press)
- [67] Guseinov I I and Mamedov B A 2011 *Astropart. Phys.* **34** 649
- [68] Bates D R and Damgaard A 1949 *Phil. Trans. R. Soc. Lond. A* **242** 101
- [69] Saffman M, Walker T and Mølmer K 2010 *Rev. Mod. Phys.* **82** 23132363
- [70] Walker T G and Saffman M 2008 *Phys. Rev. A* **77** 032723
- [71] Olmos B 2010 *Information measures of quantum systems *** Collective Rydberg excitations of an atomic gas confined in a ring lattice* Ph.D. thesis Universidad de Granada
- [72] Boisseau C, Simbotin I and Côté R 2002 *Phys. Rev. Lett.* **88** 133004

- [73] Singer K, Stanojevic J, Weidemüller M and Côté R 2005 *J. Phy. B: At. Mol. Opt. Phys.* **38** S295
- [74] Urban E, Johnson T A, Henage T, Isenhower L, Yavuz D D, Walker T G and Saffman M 2009 *Nature Phys.* **5** 110
- [75] Olmos B and Lesanovsky I 2011 *Phys. Chem. Chem. Phys.* **13** 4208
- [76] Carter J D, Cherry O and Martin J D D 2012 *Phys. Rev. A* **86** 053401
- [77] Sørensen A S, Van Der Wal C H, Childress L I and Lukin M D 2004 *Phys. Rev. Lett.* **92** 63601
- [78] Tauschinsky A, Thijssen R M T, Whitlock S, van Linden van den Heuvell H and Spreuw R J C 2010 *Phys. Rev. A* **81** 063411
- [79] Cetina M *et al.* 2011 *Hybrid approaches to quantum information using ions, atoms and photons* Ph.D. thesis Massachusetts Institute of Technology
- [80] Wimberger S 2011 *Eur. Phys. J. D* **63**
- [81] Daniilidis N, Häffner H, Stillinger F, Debenedetti P, Nozières P, Sachdev S, Castelnovo C, Moessner R and Sondhi S 2013 *Annu. Rev. Cond. Matt. Phys.* **4**
- [82] Wallquist M, Hammerer K, Rabl P, Lukin M and Zoller P 2009 *Phys. Scr.* **T137** 014001
- [83] Petrosyan D, Bensky G, Kurizki G, Mazets I, Majer J and Schmiedmayer J 2009 *Phys. Rev. A* **79** 040304
- [84] Gao M, Liu Y X and Wang X B 2011 *Phys. Rev. A* **83** 022309
- [85] Jaksch D, Cirac J I, Zoller P, Rolston S L, Côté R and Lukin M D 2000 *Phys. Rev. Lett.* **85** 2208

-
- [86] Lukin M D, Fleischhauer M, Cote R, Duan L, Jaksch D, Cirac J I and Zoller P 2001 *Phys. Rev. Lett.* **87** 037901
- [87] Gaëtan A, Miroshnychenko Y, Wilk T, Chotia A, Viteau M, Comparat D, Pillet P, Browaeys A and Grangier P 2009 *Nature Phys.* **5** 115
- [88] Weimer H, Müller M, Lesanovsky I, Zoller P and Büchler H P 2010 *Nature Phys.* **6** 382
- [89] Olmos B, González-Férez R and Lesanovsky I 2009 *Phys. Rev. Lett.* **103** 185302
- [90] Olmos B, González-Férez R and Lesanovsky I 2010 *Phys. Rev. A* **81** 023604
- [91] Porras D and Cirac J I 2008 *Phys. Rev. A* **78** 053816
- [92] Lehmberg R H 1970 *Phys. Rev. A* **2** 883
- [93] Olmos B and Lesanovsky I 2010 *Phys. Rev. A* **82** 063404
- [94] Dudin Y O and Kuzmich A 2012 *Science* **336** 887
- [95] Peyronel T, Firstenberg O, Liang Q Y, Hofferberth S, Gorshkov A V, Pohl T, Lukin M D and Vuletić V 2012 *Nature* **488** 57
- [96] Pohl T, Demler E and Lukin M D 2010 *Phys. Rev. Lett.* **104** 43002
- [97] Schachenmayer J, Lesanovsky I, Micheli A and Daley A J 2010 *New J. Phys.* **12** 103044
- [98] Mourachko I, Comparat D, Tomasi F D, Fioretti A, Nosbaum P, Akulin V M and Pillet P 1998 *Phys. Rev. Lett.* **80** 253
- [99] Beigman I L and Lebedev V S 1995 *Phys. Rep.* **250** 95
- [100] Hickman A P 1979 *Phys. Rev. A* **19** 994

- [101] Lukin M 2003 *Rev. Mod. Phys.* **75** 457
- [102] Pedersen L H and Mølmer K 2009 *Phys. Rev. A* **79** 012320
- [103] Chaneliere T, Matsukevich D N, Jenkins S D, Lan S Y, Kennedy T A B and Kuzmich A 2005 *Nature* **438** 833
- [104] Julsgaard B, Sherson J, Cirac J I, Fiurášek J and Polzik E S 2004 *Nature* **432** 482
- [105] Choi K S, Deng H, Laurat J and Kimble H J 2008 *Nature* **452** 67
- [106] Nielsen A E B and Mølmer K 2010 *Phys. Rev. A* **81** 043822
- [107] Saffman M and Walker T 2002 *arXiv preprint quant-ph/0203080*
- [108] Simon J, Tanji H, Thompson J K and Vuletić V 2007 *Phys. Rev. Lett.* **98** 183601
- [109] Scully M O, Fry E S, Ooi C H R and Wódkiewicz K 2006 *Phys. Rev. Lett.* **96** 010501
- [110] Mazets I I and Kurizki G 2007 *J. Phys. B: At. Mol. Opt. Phys.* **40** F105
- [111] Wilk T, Gaëtan A, Evellin C, Wolters J, Miroshnychenko Y, Grangier P and Browaeys A 2010 *Phys. Rev. Lett.* **104** 010502
- [112] Weatherill K J, Pritchard J D, Abel R P, Bason M G, Mohapatra A K and Adams C S 2008 *J. Phys. B: At. Mol. Opt. Phys.* **41** 201002
- [113] Fleischhauer M, Imamoglu A and Marangos J P 2005 *Rev. Mod. Phys.* **77** 633
- [114] Ates C, Sevinçli S and Pohl T 2011 *Phys. Rev. A* **83** 041802

-
- [115] Müller M, Lesanovsky I, Weimer H, Büchler H P and Zoller P 2009 *Phys. Rev. Lett.* **102** 170502
- [116] Kruse J, Gierl C, Schlosser M and Birkel G 2010 *Physical Review A* **81** 060308
- [117] Göppert-Mayer M 1931 *Ann. Phys.* **401** 273
- [118] Suzuki S, Inoue J I and Chakrabarti B K 1996 *Quantum Ising Phases and Transitions in Transverse Ising Models* (Springer)
- [119] Holstein T and Primakoff H 1940 *Phys. Rev.* **58** 1098
- [120] Jordan P and Wigner E 1928 *Z. Physik* **47** 631
- [121] Derzhko O 2001 *arXiv preprint cond-mat/0101188*
- [122] Hauke P 2009 *Classical and Quantum Simulations of Frustrated Spin Models* Master's thesis Technische Universität München
- [123] Blasiak P, Horzela A, Penson K A, Solomon A I and Duchamp D H E 2007 *Am. J. Phys.* **75** 639
- [124] Castilla G E and Chakravarty S 1991 *Phys. Rev. B* **43** 13687
- [125] Dirac P A M 1927 *Proc. R. Soc. Lond. A* **114** 243
- [126] Laycock T, Olmos B and Lesanovsky I 2011 *J. Phys. B: At. Mol. Opt. Phys.* **44** 184017
- [127] Fewell M P 2005 *Opt. Commun.* **253** 125
- [128] Walls D F and Milburn G J 2008 *Quantum Optics* 2nd ed (Springer-Verlag)

- [129] Lukin M D 2009 Modern atomic and optical physics ii: Course notes harvard university Lecture Notes URL <http://lukin.physics.harvard.edu/teaching.htm>
- [130] Dummit D S and Foote R M 2003 *Abstract Algebra* 3rd ed (John Wiley & Sons)
- [131] Colpa J H P 1978 *Physica* **93A** 327
- [132] Bhatia R 2007 *Positive Definite Matrices* (Princeton University Press)
- [133] Horn R A and Johnson C R 1985 *Matrix Analysis* 1st ed (Cambridge University Press)
- [134] Golub G H and Loan C F V 1996 *Matrix Computations* 3rd ed (Johns Hopkins University Press)
- [135] Hazewinkel M 1995 *Encyclopaedia of Mathematics* vol 1 (Kluwer Academic Publishers)
- [136] Colpa J H P 1979 *J. Phys. A: Math. Gen.* **12** 469
- [137] Steck D A 2001 Rubidium 87 d line data URL <http://www.steck.us/alkalidata/rubidium87numbers.pdf>
- [138] Argawal G S 1970 *Phys. Rev. A* **2** 2038
- [139] Gardiner C W and Zoller P 2004 *Quantum Noise* (Springer-Verlag)
- [140] Breuer H P and Petruccione F 2006 *The Theory of Open Quantum Systems* (Clarendon Press)
- [141] DiVincenzo D P 2000 *Fortschr. Phys* **48** 771
- [142] Nielsen M A and Chuang I L 2010 *Quantum computation and quantum information* (Cambridge university press)

- [143] Reetz-Lamour M, Amthor T, Deiglmayr J, Westermann S, Singer K, de Oliveira A L, Marcassa L G and Weidemüller M 2006 *Fortschr. Phys.* **54** 776
- [144] Younge K C 2010 *Rydberg atoms for quantum information* Ph.D. thesis The University of Michigan
- [145] Weimer H, Müller M, Lesanovsky I, Zoller P and Büchler H P 2010 *Nature Phys.* **6** 382
- [146] Hogan S D, Agner J A and Merkt F 2012 *Phys. Rev. Lett.* **108** 063004
- [147] Bohlouli-Zanjani P, Petrus J A and Martin J D D 2007 *Phys. Rev. Lett.* **98** 203005
- [148] Mansbach P and Keck J 1969 *Phys. Rev.* **181** 275
- [149] Percival I C 1973 *Comput. Phys. Commun* **6** 347
- [150] Abd D Vrinceanu T P and Sadeghpour H R 2008 *Phys. Rev. Lett.* **100** 223201
- [151] Vriens L and Smeets A H M 1980 *Phys. Rev. A* **22** 940
- [152] Hu S X 2006 *Phys. Rev. A* **74** 062716
- [153] Dutta S K, Feldbaum D, Walz-Flannigan A, Guest J R and Raithel G 2001 *Phys. Rev. Lett.* **86** 3993
- [154] Walz-Flannigan A, Guest J R, Choi J H and Raithel G 2004 *Phys. Rev. A* **69** 063405
- [155] Millen J, Lothead G and Jones M P A 2010 *Phys. Rev. Lett.* **105** 213004
- [156] Hoffrogge J, Frölich R, Kasevich M A and Hommelhoff P 2011 *Phys. Rev. Lett.* **106** 193001

- [157] Ewart P Atomic physics. university of Oxford Atomic Physics Lecture Notes
- [158] Landau L D and Lifshitz E M 1977 *Quantum Mechanics (Non-Relativistic Theory)* 3rd ed vol Three (Butterworth-Heinemann)
- [159] Vvedensky I Chapter 3: The renormalization group in momentum space. lorentz Center Presentation from 2010 URL http://www.lorentzcenter.nl/1c/web/2010/404/presentations/VvedenskyI_4.pdf
- [160] Born M and Oppenheimer J R 1927 *Ann. Physik* **84** 457
- [161] Zettili N 2009 *Quantum Mechanics: Concepts and Applications* 2nd ed (John Wiley & Sons, Ltd)
- [162] Seaton M J 1983 *Rep. Prog. Phys.* **46** 167
- [163] Beterov I I, Ryabtsev I I, Tretyakov D B and Entin V M 2009 *Phys. Rev. A* **79** 052504
- [164] Li W, Mourachko I, Noel M W and Gallagher T F 2003 *Phys. Rev. A* **67** 052502
- [165] Liberman S and Pinard J 1979 *Phys. Rev. A* **20** 507
- [166] Karr W A, Jamell C R and Joglekar Y N 2010 *Am. J. Phys.* **78** 407
- [167] Butcher P N and Cotter D 1991 *The elements of nonlinear optics* (Cambridge University Press)
- [168] Hausdorff F 1906 *Ber. Ver. Sächs. Akad. Wiss. Leipzig* **58** 19
- [169] Lippmann B A and Schwinger J 1950 *Phys. Rev.* **79** 469
- [170] Hubač I, Masarik J and Wilson S 2011 *J. Phys. B* **44** 205201

-
- [171] Economou E N 2006 *Green's Functions in Quantum Physics* 3rd ed (Springer)
- [172] Moore M G 2008 Introduction to scattering theory Tech. rep. Michigan State University URL <http://www.pa.msu.edu/~mmoore/852scattering.pdf>
- [173] Cauchy A L 1831 On the celestial mechanics and on a new calculus that can be applied to a great number of diverse questions Presented to the Academy of Sciences, Turin
- [174] Cauchy A L 1831 Memorandum on the connections that exist between the residue calculus and the limit calculus, and on the advantages that these two calculi offer in solving algebraic and transcendental equations Presented to the Academy of Sciences, Turin
- [175] Jaffe C and Reinhardt W P 1977 *J. Chem. Phys.* **66** 1285
- [176] Stark J 1914 *Ann. Phys. (Berlin)* **43** 965
- [177] Zimmerman M L, Littman M G, Kash M M and Kleppner D 1979 *Phys. Rev. A* **20** 2251
- [178] Inglis D R and Teller E 1939 *Astrophys. J.* **90** 439
- [179] van Ditzhuijzen C S E 2009 *Dipole-dipole interaction between cold Rydberg atoms* Ph.D. thesis Universiteit van Amsterdam
- [180] DeMille D 2002 *Phys. Rev. Lett.* **88** 067901
- [181] Micheli A, Brennen G K and Zoller P 2006 *Nature Phys.* **2** 341
- [182] Scully M O and Zubairy M S 1997 *Quantum Optics* (Cambridge University Press)